INVESTIGATION OF MAGNETIC ANOMALIES OF UBIAJA AND ILLUSHI AREAS IN NORTHERN ANAMBRA BASIN USING AEROMAGNETIC DATA

BY

OKORIE, ALEXIUS CHUKWUDI
(PG/M.Sc./14/68244)

DEPARTMENT OF PHYSICS AND ASTRONOMY

FACULTY OF PHYSICAL SCIENCES

UNIVERSITY OF NIGERIA, NSUKKA

JUNE, 2016

INVESTIGATION OF MAGNETIC ANOMALIES OF UBIAJA AND ILLUSHI AREAS IN NORTHERN ANAMBRA BASIN USING AEROMAGNETIC DATA

A Research work submitted in partial fulfilment of the Requirements for the Award of the Degree of Master of Science (M.Sc.) in

Solid Earth Geophysics

BY

OKORIE, ALEXIUS CHUKWUDI
(PG/M.Sc./14/68244)

DEPARTMENT OF PHYSICS AND ASTRONOMY
FACULTY OF PHYSICAL SCIENCES
UNIVERSITY OF NIGERIA, NSUKKA

SUPERVISOR: DR D.N. OBIORA

JUNE, 2016

DEDICATION

This thesis is dedicated to my parents (Mr and Mrs Okorie) for their unrelenting support in the course of this programme.

CERTIFICATION

Okorie, Alexius Chukwudi, a postgraduate student of the Department of Physics and Astronomy with registration number **PG/M.Sc./14/68244** has satisfactorily fulfilled the requirements for the course and research work for the award of the degree of Master of Science (**M.Sc.**) in Solid Earth Geophysics.

... **..**
DR D.N. OBIORA **DATE**
SUPERVISOR

.. **..**
PROF. J.O. URAMA **DATE**
HEAD OF DEPARTMENT

.. **…………………………**
EXTERNAL EXAMINER **DATE**

ACKNOWLEDGEMENTS

My inexplicable gratitude goes to God Almighty who has made this thesis a reality. This work was feasible because of the support of many individuals who in one way or other contributed to this work.

First and foremost, my gratitude goes to my project supervisor, Dr. D.N. Obiora for taking his time to supervise and thoroughly go through this work, I say thanks a million. I want to thank in a special way my lecturer in University of Agriculture Makurdi, Dr. (Mrs) Isikwue for introducing me to geophysics in my final year.

I cannot forget to thank my parents, Mr and Mrs Okorie for their continuous care and support during my stay in school and also for my sibling; Eusebius, George, Jovita, Jennifer, Judith and Catherine.

I also want to thank Mrs Isa Catherine for her financial and moral support towards the completion of my master's programme. Finally I cannot forget to thank my friends; Dr. Johnson Ibuot, Emeka Njoku-Achu, Anthony Umeogamba, Ijeoma Chinedu, Bala Gabriel, Ossai Okwudili, Akor Yakubu, Aroh Bernard and Ernest (my room mate).

TABLE OF CONTENTS

LIST OF TABLES

LIST OF FIGURES

ABSTRACT

The aeromagnetic data of Ubiaja and illushi area that fall within latitude $6°30'N$ to $7°00'N$ and longitude $6°00'E$ to $7°00'E$ were interpreted qualitatively and quantitatively. The qualitative interpretation revealed that the area is intensely faulted with major anomalies (faults) trending in the northeast and southwest directions. Standard Euler deconvolution, source parameter imaging (SPI), spectral analysis and modelling (forward and inverse) methods were employed in the quantitative interpretation aimed at determining the depth or thickness of the sedimentary basin, magnetic susceptibilities and type of mineralization prevalent in the area. The results obtained by employing SPI have shown the minimum to maximum depths of 258.2 m to 3497.7 m of anomalous source bodies. Applying standard Euler deconvolution method for the structural index (SI), the depth obtained for SI = 0.5 ranges from 1377.3 m (outcropping and shallow magnetic bodies) to 2510.9 m (deep lying magnetic bodies); for SI = 1, the depth to magnetic source ranges from 1482.0 (outcropping and shallow magnetic bodies) to 3003.3 m (deep lying magnetic bodies); for SI = 2, the depth to magnetic source ranges from 1627.8 m (outcropping and shallow magnetic bodies) to 2984. 3 m (deep lying magnetic bodies); and for SI = 3, the depth ranges from 1853.9 m (outcropping and shallow magnetic bodies) to 3089.9 m (for deep lying magnetic bodies). The spectral depth obtained revealed two source depths, shallow and deeper. The deeper depth ranges from 1114.085 m to 3978.874 m with an average value of 2105.014 m, while the shallow depth ranges from 163.836 m to 460.057 m with an average value of 295.708 m. The results from forward and inverse modelling for profiles 1, 2, 3 and 4 showed depths of 4118 m, 3611 m, 2964 m and 5489 m respectively. From the results of susceptibility values obtained, profiles 1 and 2 with susceptibility value of 0.0100 is underlain by a body associated with group of minerals like hematite, gneiss, granite or gabbro. Profile 3 with susceptibility value of 0.0613 is typical of igneous rock porphyry. Profile 4 with susceptibility value of 0.0288 is typical with minerals like slate and hematite. The depth obtained from the four methods show thick sediment but on an average, the sedimentary thickness of the area is fairly sufficient for hydrocarbon accumulation.

CHAPTER ONE

INTRODUCTION

1.1 Background of the Study

Minerals and hydrocarbon play vital roles in the socio-economic development of a country. Before the colonial era to the era of the 1960's, the search for mineral deposits and hydrocarbon has been a major business challenge in Nigeria. It is no doubt that the foundation or basis of the Nigerian economy has been the solid minerals and now the booming oil sector since over 80% of the nation economy depends greatly on it (Obiora *et al.,* 2015). Since all the exploitation of hydrocarbon in Nigeria is mostly done in the Niger delta, it will benefit the country if other sedimentary basin such as the Anambra basin is explored. Anambra basin where Ubiaja and Illushi fall is one of those basins being suspected to have hydrocarbon and solid minerals prospect.

Magnetic method is a geophysical survey technique that exploits considerable differences in the magnetic properties of minerals with respect to the ultimate objective of characterizing the earth's subsurface. The technique requires the acquisition of measurements of the amplitude of the magnetic field at discrete points along survey lines distributed regularly throughout the area of interest (Horsfall, 1997). The magnetic field, whose amplitude is measured, is the vector sum of:

(i) earth's main field which originates from dynamo action of conductive fluids in the earth's deep interior (Merill *et al.*, 1996);

(ii) an induced fluid caused by magnetic induction in magnetically susceptible earth material polarized by the main field (Doell and Cox, 1967);

(iii) a field caused by remanent magnetism of the earth materials (Doell and Cox, 1967) and

(iv) others, usually less significant fields caused by solar, atmospheric and other cultural influences (Telford *et al.*, 1990).

Magnetic prospecting, the oldest method of geophysical exploration, is used to explore for oil, minerals and even archaeological artifacts. In prospecting for oil, it gives information from which one can determine the depth to basement rocks and thus locate and define the extent of sedimentary basins. Another application is the delineation of intra-sedimentary magnetic sources, such as shallow volcanics or intrusives that disrupt the normal sedimentary sequence (Peterson and Reeves, 1985).

Magnetic surveys can be carried out on land, at sea and in the air. Consequently, the technique is widely employed and the method is very attractive in the search for the types of ore deposits that contain magnetic minerals (Kearey *et al.*, 2002). An aeromagnetic survey is a common type of survey carried out using a magnetometer aboard or towed behind an aircraft. The principle is similar to a magnetic survey carried out with hand-held magnetometer, but allows much larger areas of the earth's surface to be covered quickly for regional reconnaissance. The aircraft typically flies in a grid-like pattern with height and line spacing determining the resolution of the data.

1.2 Operation of Magnetic Survey

As the aircraft flies, the magnetometer measures and records the total intensity variation of the field at the sensor, which is a combination of the desired magnetic field generated in the earth as well as tiny variations due to temporal effects of the constantly varying solar wind and the magnetic field of the survey aircraft. By subtracting the solar, regional and aircraft effects, the resulting aeromagnetic map shows the spatial distribution and relative abundance of magnetic minerals (most commonly the iron oxide mineral magnetite) in the upper levels of the earth's crust. Since different rock types differ in their content of magnetic minerals, the magnetic map allows a visualization of the geological structure of the upper crust in the subsurface, particularly the spatial geometry of bodies or rock and the presence of faults and folds. This is particularly useful where bedrock is obscured by surface sand, soil or water. Aeromagnetic data was once presented as contour plots, but now is commonly expressed in gridded maps and pseudo-topography images. The apparent hills, ridges and valleys are referred to as the anomalies. A geophysicist can use mathematical model to infer shape, depth and properties of the rock bodies responsible for the anomalies. Airplanes are commonly used for high-level reconnaissance surveys in gentle terrain, and helicopters are used in mountainous terrain or where more detail is required. Unmanned Aerial Vehicles (UAVs), commonly known as a ‘drone’ is an aircraft without a human pilot aboard and can also be used in aeromagnetic survey work (Burger *et al.,* 2006).

1.3 Applications of Aeromagnetic Surveys

Aeromagnetic surveys are widely used to aid in the production of geophysical maps and are commonly used during mineral and petroleum exploration. Some mineral deposits are associated with an increase in the abundance of magnetic minerals and occasionally the sought after commodity may itself be magnetic (example iron ore deposits), but often the elucidation of the subsurface structure of the upper crust is the most valuable contribution of the aeromagnetic data.

Aeromagnetic surveys were performed in World War II to detect submarines using magnetic anomaly detector attached to an aircraft. Aeromagnetic surveys also used to perform reconnaissance mapping of Unexploded Ordnance (UXO). Unexploded Ordnance (sometimes acronymized as UO, Unexploded Bomb (UXB), or explosive remnants of war (ERW)) are explosive weapons (bombs, shells, grenades, land mines, cluster munitions, etc.) that did not explode when they were employed and still pose a risk of detonation, potentially many decades after they were used or discarded.

1.4 Location and Geology of the Study Area

The regional map of Nigeria showing the Anambra basin (Figure 1.1) shows the location of some basins with the various formations associated with the basins. The northern Anambra basin within which Ubiaja and Illushi areas fall is located between latitude $N6°30' - N7°00'$ and longitude $E6°00' - E7°00'$. The study area covers a total area of about 6050 square - kilometer which is situated in the southwestern Nigeria. Ubiaja is located in the Ishan district of Edo state, and is bothered to the south by Benin City, to the southeast by Agbor, to the northeast by Etsako, to the west by river Niger. Illushi is located in sub-locality, Illushi locality district, Edo state of Nigeria. Two aeromagnetic maps (sheets 285 and 286) covered the area. The study area consists of two formations and alluvium deposit. These formations include Ameki or Bende-Ameki and Imo shale or Ebenebe sandstone as shown in the detailed geology map of the study area (Figure 1.2).

Stratigraphically, the Ameki formation overlies the impervious Imo shale group characterized by lateral and vertical variations in lithology. The Imo shale of Paleocene age is underlain in succession by Nsukka formation, Ajali sandstones and Nkporo shales (Reyment, 1965).

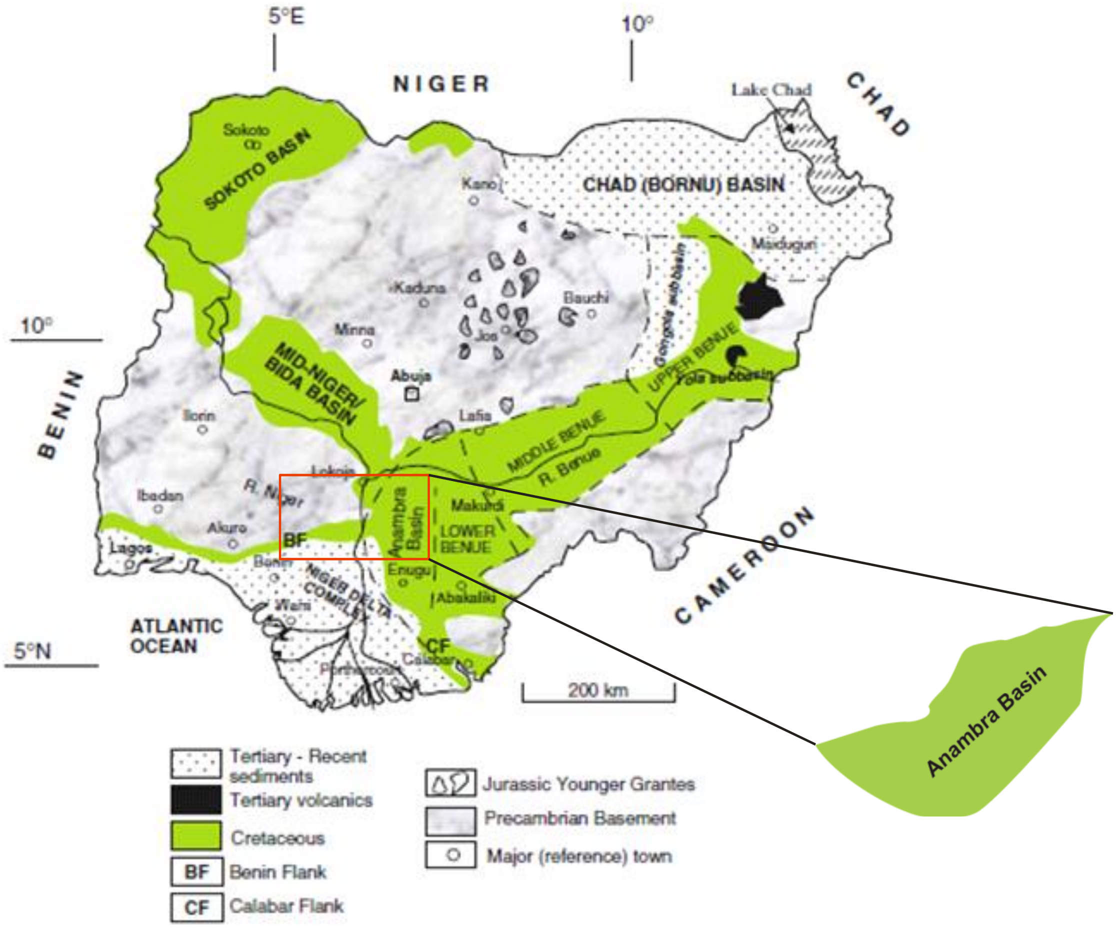

Figure 1.1: A regional map of Nigeria showing the Anambra basin (Obaje, 2009)

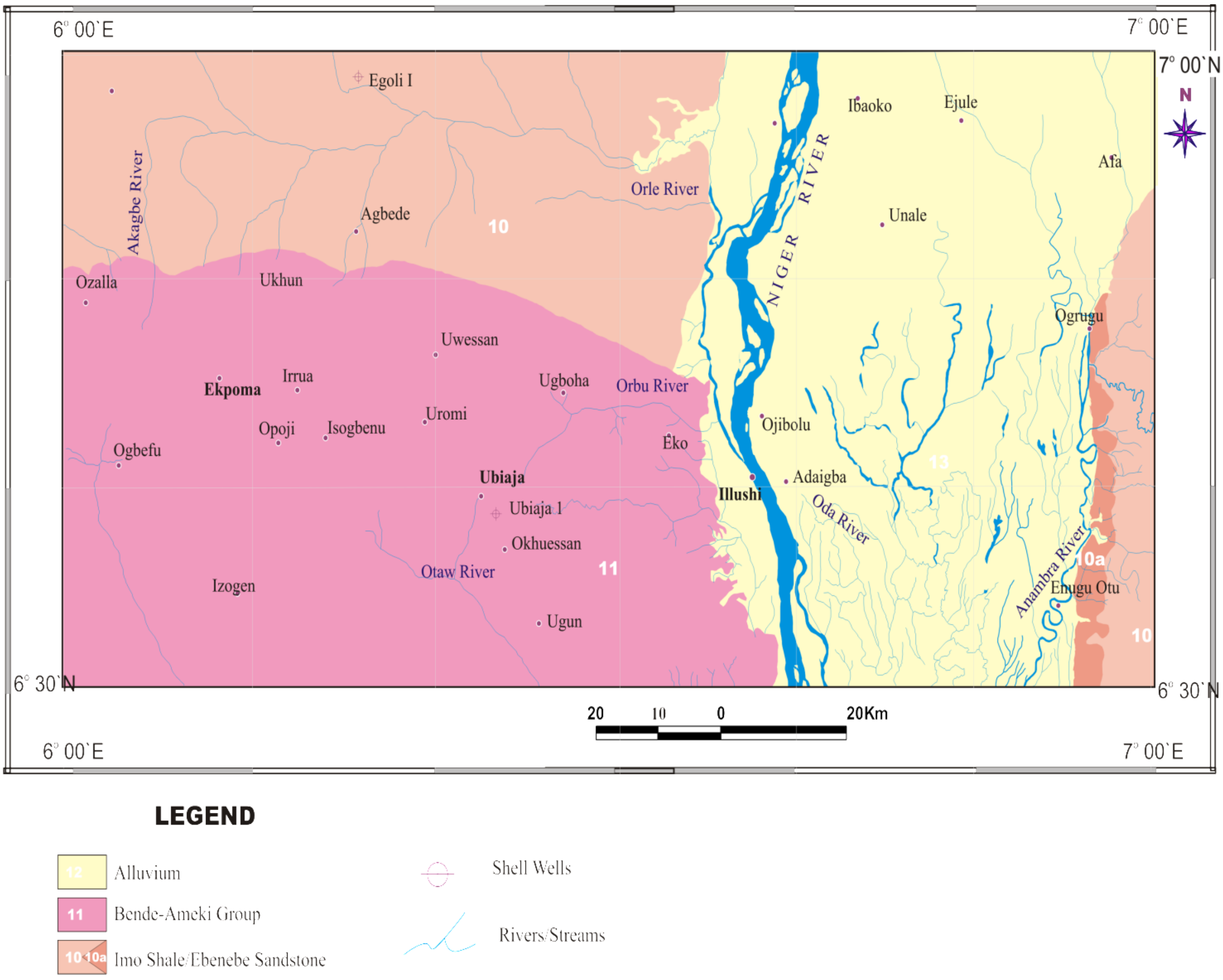

Figure 1.2: A geology map of the study area (Ubiaja and Illushi sheets)

1.5 Geologic Setting

The Anambra basin is one of the sub-basins in the Benue trough (Reijers *et al.,* 1997). It is a multicycle basin whose initiation begin in the late Jurassic to the early cretaceous associated with the opening of the Gulf of Guinea and south Atlantic ocean consequent upon the separation of the African and South American plates (Benkhelil, 1989). The Anambra basin is about 40,000 square kilometer in size (Ogala, 2011) and is bounded to the west by Okitipupa ridge, in the east by Abakaliki basin, and in the south by the Niger Delta basin. The present day Anambra basin evolved after the santonian tectonism that affected the Benue trough characterized by uplift of the Abakaliki structure and subsequent down warping of the

Anambra platform and Afikpo syncline which are respectively SW and SE of the Abakaliki structure (Reijers *et al.*, 1997). Its basin fill is estimated to be about 5000 to 7000 metres (Agagu and Adhijie, 1983) and contains merely cretaceous to tertiary continental-marine sediments. The sediments display a wedge outlines and exhibits soft sediments definition structures (Obi and Okogbue, 2004) which suggests that the sedimentation was tectonically controlled.

1.6 Stratigraphy

The stratigraphy successions in the Anambra basin have been described by many authors (Simpson, 1954; Reyment, 1965; Agagu *et al.*, 1985; Armajor, 1989; Nwajide and Reijers, 1996; Nwajide, 2005). The Nkporo Group constitutes the basalt lithostratigraphic unit in the Anambra basin and was deposited during late companion – early maastritchtian period. The Nkporo formation consists of dark shales and mudstones with subordinate sandstones, oolitic iron stone and shelly limestone with commonly burrows of skolithos isp., ophiomorpha isp., and thalassinoides isp. The Enugu formation, a lateral equivalent of the Nkporo formation consists of grey, blue or dark shale, occasional white sandstones and striped sandy shale beds. The Owelli sandstone comprises the fining upward successions of hard ferruginous sandstones, cross-bedded sand stone, shale, siltstone, coal, kaolinitic clay, vitrinite and wood fragments. The Mamu formation, the Ajali sandstone and the lower Nsukka formation were deposited conformably during the maastrichtian stage over the Nkporo group and consists of shale heteroliths, sandstones and coal (Kogbe, 1989). The Ajali sandstone is dominated by sandstones in which kaolinitic clay interbeds are common and overlies the Mamu formation. The Nsukka formation (Reyment, 1965) overlies the Ajali sandstone. It consists of an alternating succession of sandstones and shales with thin coal seams. The Anambra basin and gross depositional environment is shown in Figure 1.3.

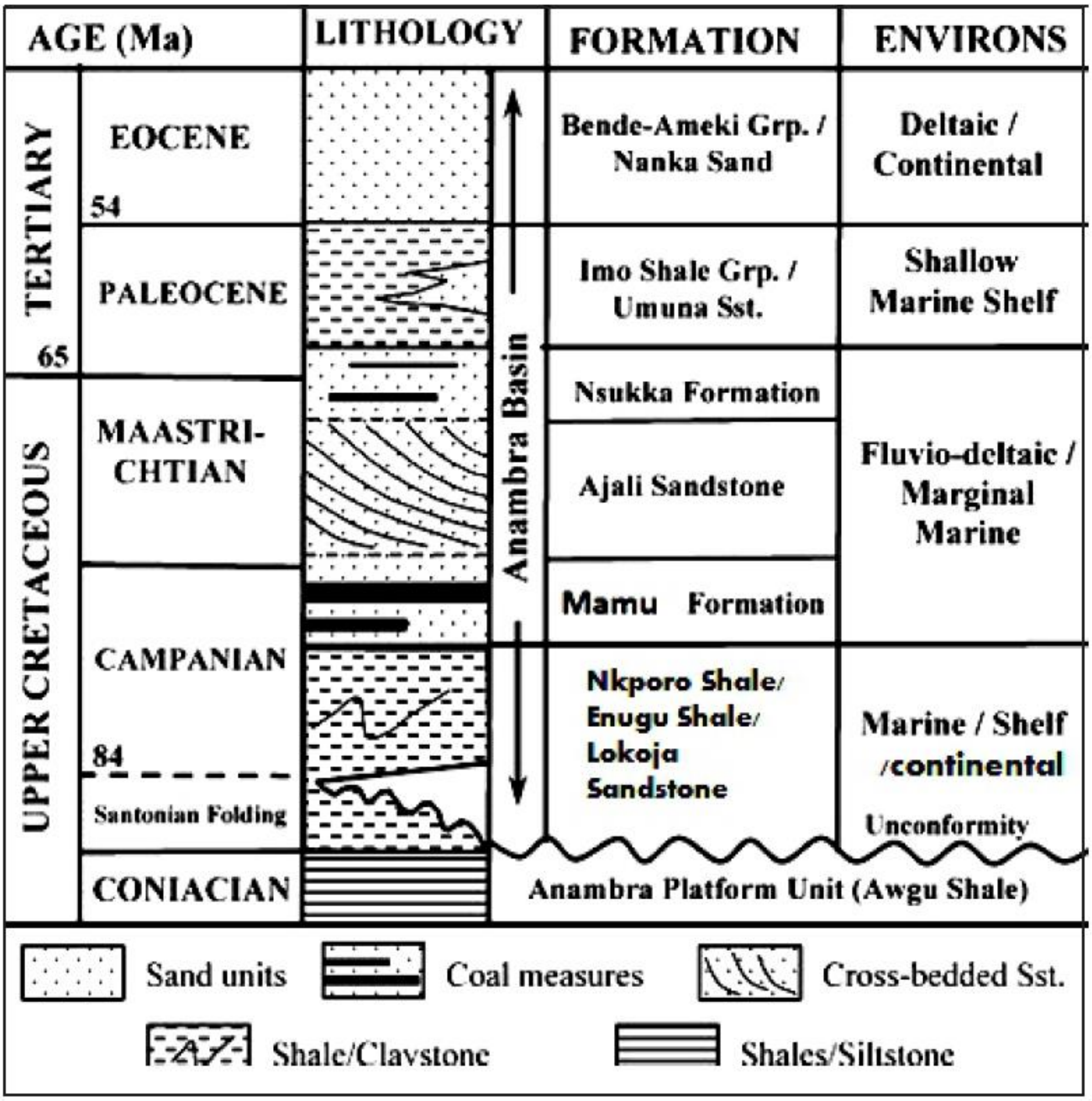

Figure 1.3: Anambra basin stratigraphy and gross depositional environment (Tijani *et al.*, 2010)

1.7 The Earth's Magnetic Field and its Anomalies

From the point of view of geomagnetism, the earth may be considered as made up of three parts: core, mantle and crust (Figure 1.4). Convection process in the liquid part of the iron core give rise to a dipolar geomagnetic field that resembles that of a long bar-magnet aligned approximately along the earth's axis rotation (Figure 1.5). The mantle plays little part in the earth's magnetism, while interaction of the (past and present) geomagnetic field with the rocks of the earth's crust producing the magnetic anomalies recorded in detailed aeromagnetic surveys carried out close to the earth's surface (Reeves, 2005).

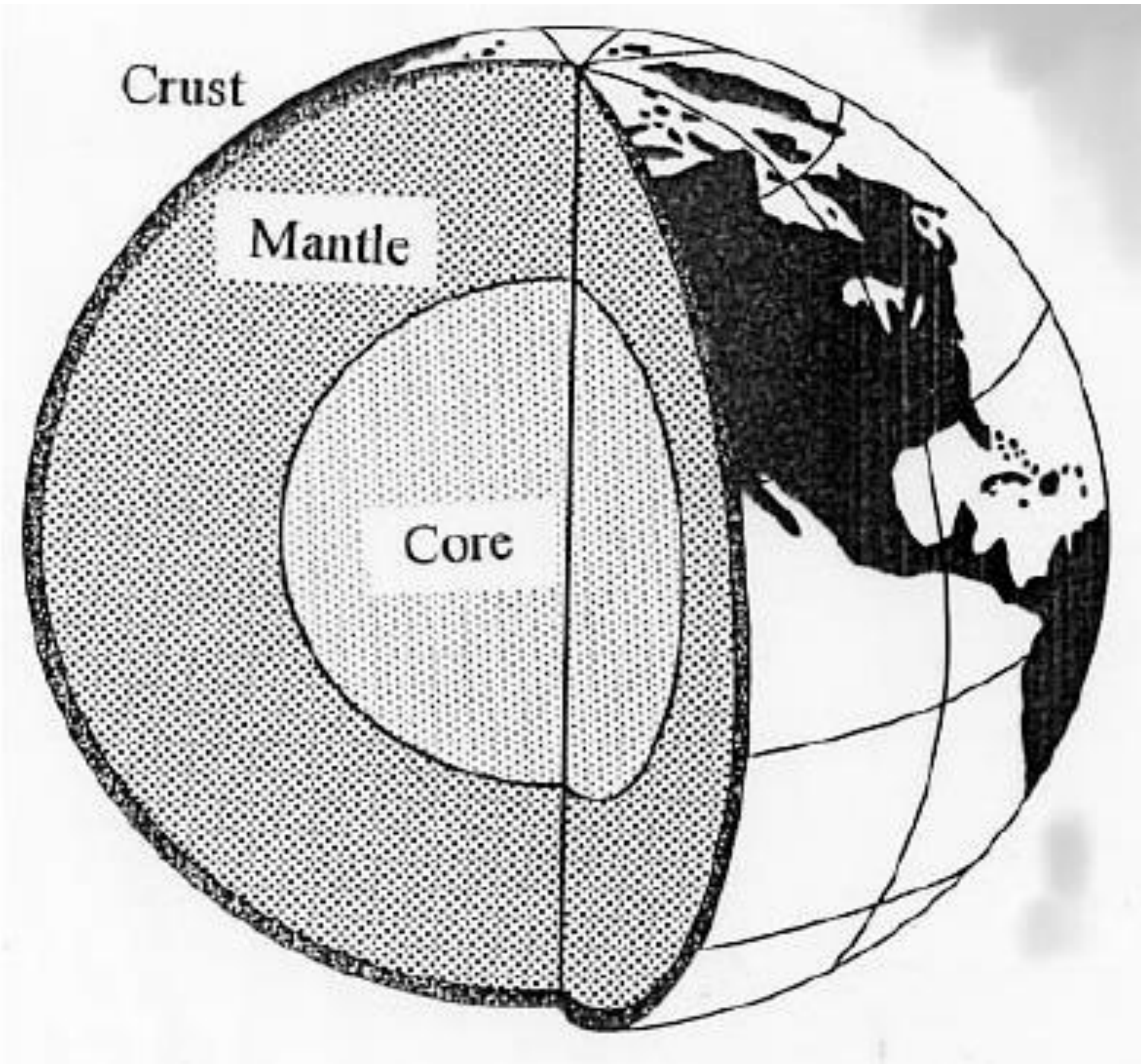

Figure 1.4: The main divisions of the earth's volume (Reeves, 2005)

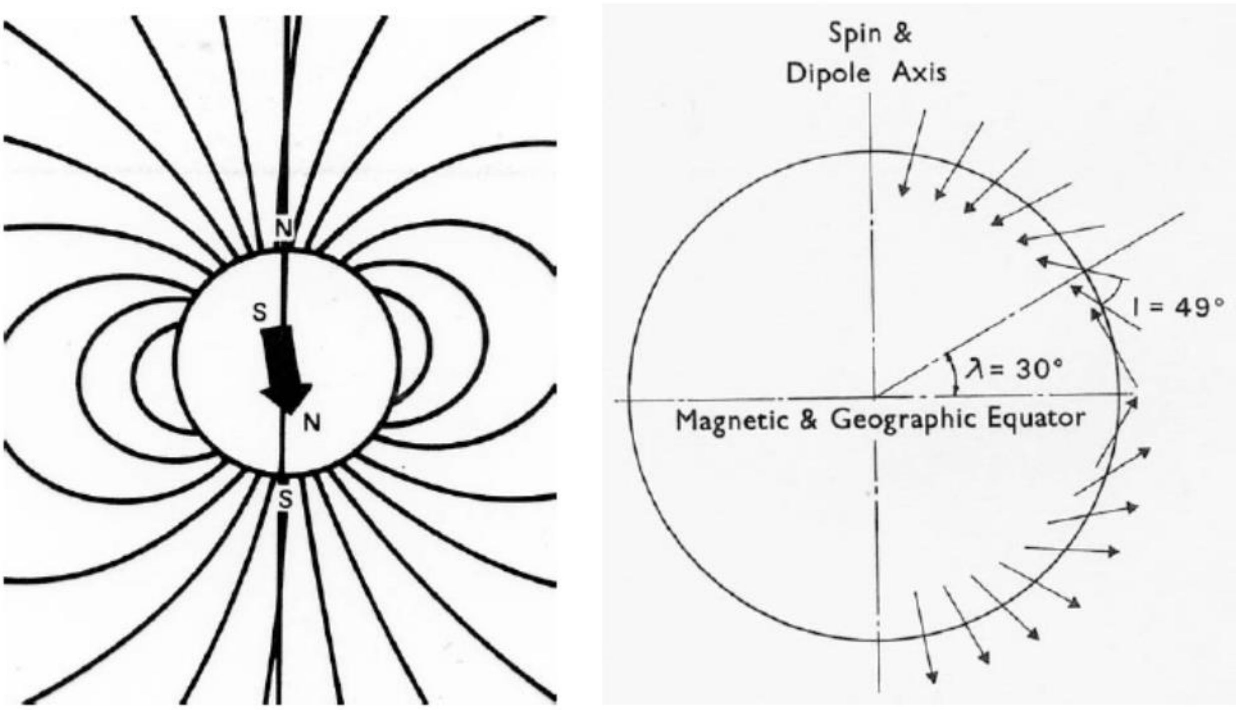

Figure 1.5: The earth's dipolar magnetic field (Reeves, 2005)

1.8 Magnetic Field of the Earth

The earth's magnetic field can be divided into three main components from the point of magnetic exploration:

(i) The main field originating within the earth's interior and changing relatively slowly.

(ii) A small field (compared to the main field) which varies rapidly and originates outside of the earth.

(iii) Spatial variations of the main field usually smaller than the main field and usually invariant in the time and place, caused by the inhomogeneities of the earth's crust. These are the target of the magnetic exploration.

1.8.1 The Earth's main Field

According to the electromagnetic theory, the magnetic field is a consequence of a flow of electrically charged particles (electric current). A current flowing in a circular loop acts as a magnetic dipole located in the centre of the loop (Figure 1.6).

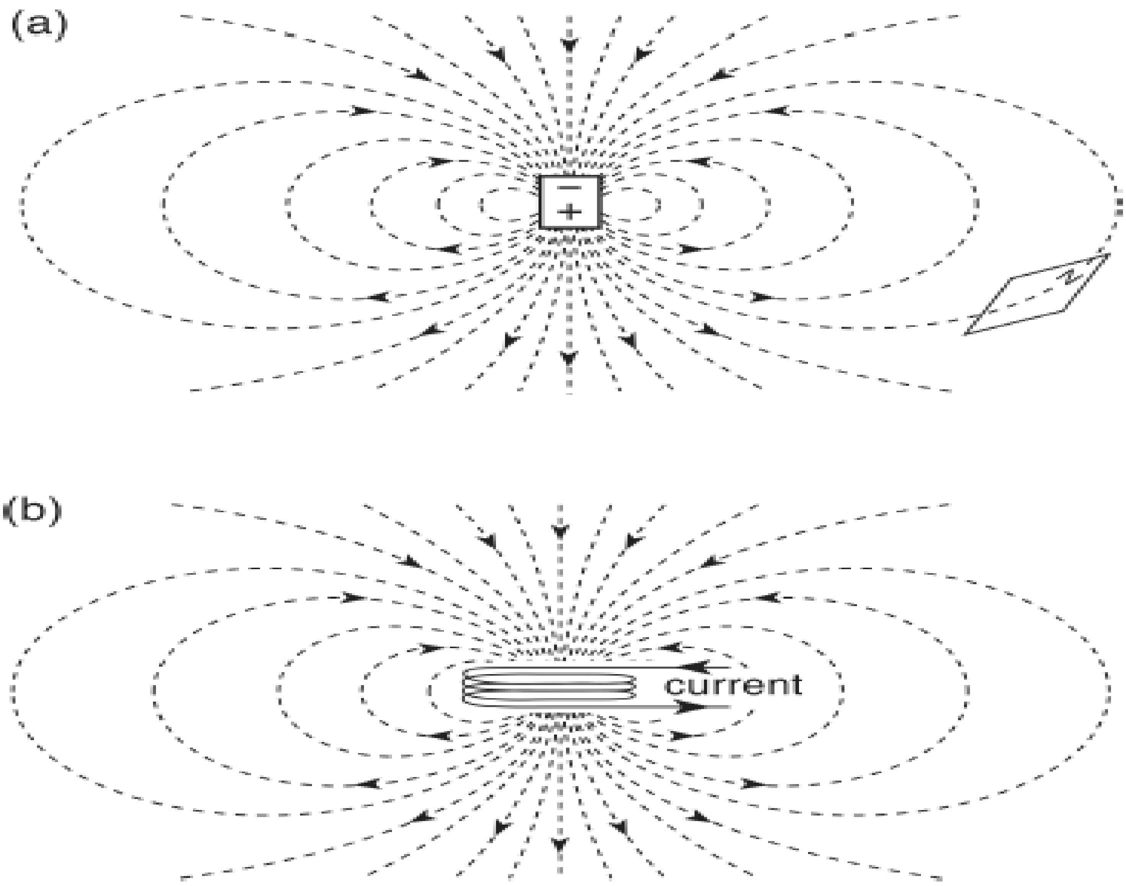

Figure 1.6: Magnetic field of a bar magnet and a coil (Musset and Khan, 2000)

The magnetic field of the earth (the geomagnetic) is supposed to be formed like this – by the electric currents flowing in the outer core, the geodynamo. The currents are generated by the convection currents in the conductive liquid outer core; however, the process is complex and not fully understood so far. The principal component of the earth magnetic field is the dipole, but also higher orders are present. These are predominately during the poles reversals, where the main (dipole) field is ceasing.

Hence the geomagnetic field could be approximated by a dipole situated in the earth's centre (Figure 1.7). The dipole is not aligned with the rotation axis and hence the magnetic pole is deviated from the geographic pole (Valenta, 2015).

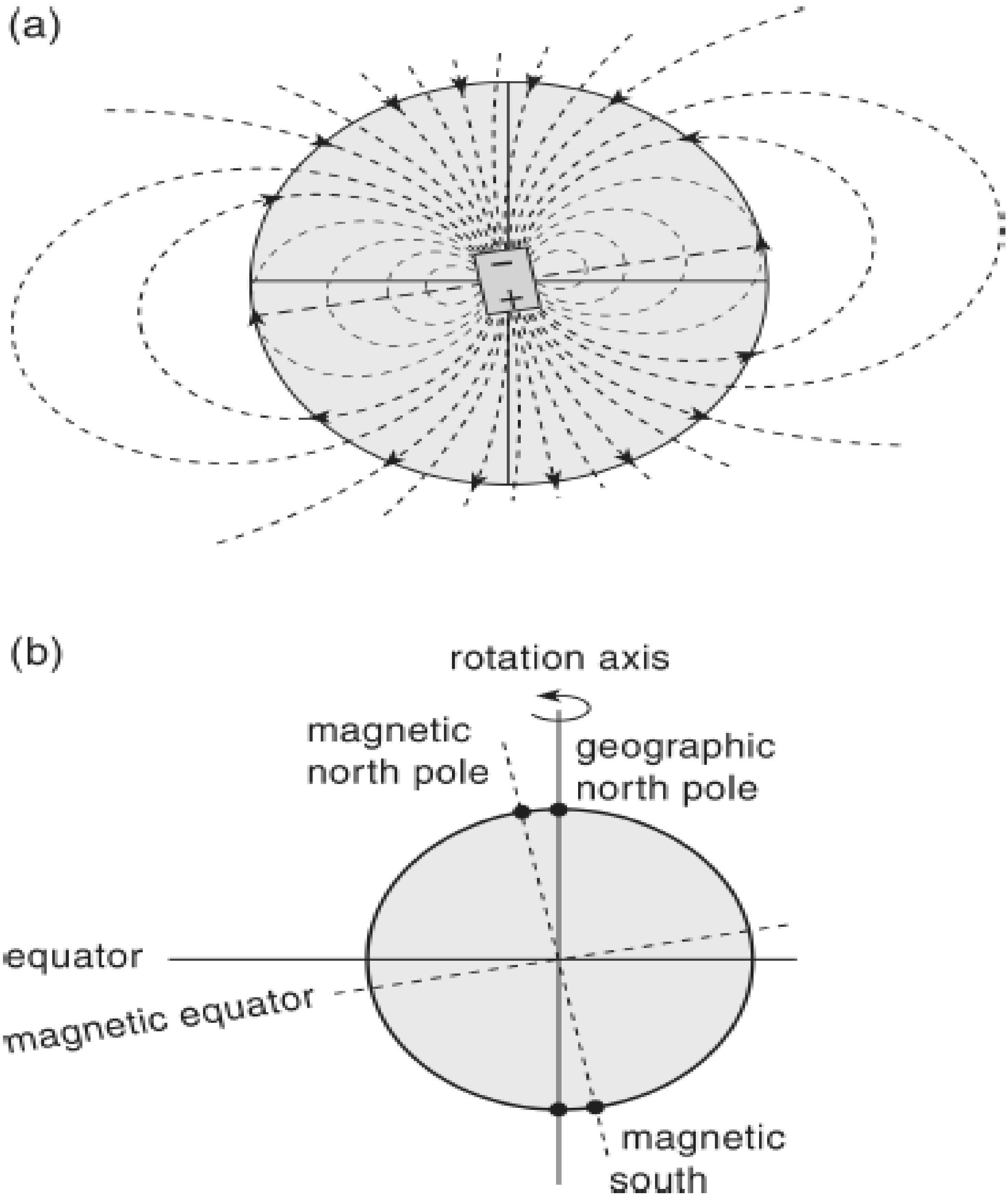

Figure 1.7: Magnetic field of the earth (Musset and Khan, 2000)

1.8.2 Temporal Variation of the Earth's Magnetic Field

The magnetic field varies with time. When describing temporal variations of the magnetic field, it is useful to classify these variations into one of three types depending on their rate of occurrence and source. There are three basic temporal variations of the earth's magnetic field; secular variations, diurnal variations and magnetic storms.

(i) **Secular Variations** – These are long-term (changes in the field that occur over years) variations in the main magnetic field that are presumably caused by fluid motion in the Earth's outer core. Because these variations occur slowly with respect to the time of completion of a typical exploration magnetic survey, these variations will not complicate data reduction efforts (Dobrin and Savitt, 1988).

(ii) **Diurnal Variations** – These are variations in the magnetic field that occur over the course of a day and are related to variations in the Earth's external magnetic field. This variation can be on the order of 20 nT to 30 nT per day and should be accounted for when conducting exploration magnetic surveys (Dobrin and Savitt, 1988).

(iii) **Magnetic Storms** – Occasional, magnetic activity in the ionosphere will abruptly increase. The occurrence of such storms correlates with enhanced sunspot activity. The magnetic field observed during such times is highly irregular and unpredictable, having amplitudes as large as 1000 nT. Exploration magnetic survey should not be conducted during magnetic storms. This is because the variations in the field that they can produce are large, rapid, and spatially varying. Therefore, it is difficult to correct for them in acquired data (Dobrin and Savitt, 1988).

1.9 Magnetism of rocks and minerals

The overall magnetization of the rocks is a vector sum of induced magnetization (the magnetization present only if an external field applied, ceases, when the external field is removed) and natural remanent magnetization (present even without the external field). For example, effusive rocks have the remanent magnetization often much stronger than induced one. According to their behaviour when placed into an external field, the material could be divided into two main groups – diamagnetic and paramagnetic. Diagrams showing the orientation of magnetic moments in the crystal lattice of different materials are shown in Figure 1.8.

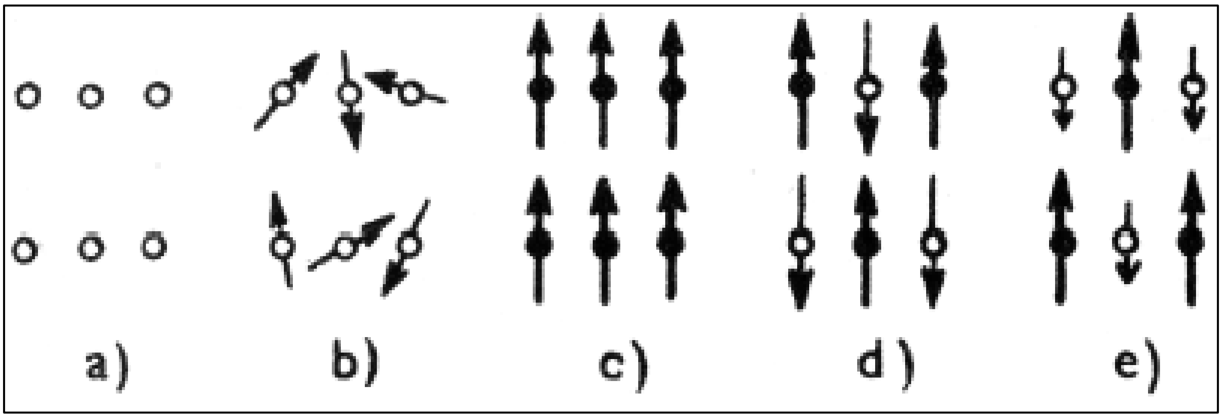

Figure 1.8: Schematic diagram showing orientation of magnetic moments in the crystal lattice of different materials: (a) diamagnetic, (b) paramagnetic, (c) ferromagnetic, (d) antiferromagnetic and (e) ferromagnetic (Mares and Turdy, 1984).

Diamagnetic material is dominated by atoms with orbital orientation to oppose the external field ─ the susceptibility is negative.

Examples of diamagnetic materials are graphite, quartz, feldspar, marble, salt, etc. Atoms of paramagnetic materials have non-zero moments without the presence of external field and magnetic susceptibility of such materials is positive. The direction of magnetization of individual atoms is randomly oriented and their vector sum is non-zero, but weak. In presence of extreme field, the magnetic atom slightly aligns forming a weak magnetization─ an induced magnetization. When the external field is removed, the magnetization ceases. The magnetic effect of diamagnetic and most paramagnetic substances is weak. Certain paramagnetic materials (iron, nickel, cobalt) could have such strong magnetic interactions that the magnetic moments in larger regions─ domains align. This effect is called ferromagnetism and it decreases with increasing temperature and ceases when the temperature exceeds the Curie point. The ferromagnetism decreased with increasing temperature and ceases when the temperature exceeds the Curie point.

Some materials have domains further divided into subdomains with opposite orientation and the overall magnetic moment nearly cancels. These materials are called antiferromagnetic and their susceptibility is low. The common example is hematite. The last group has subdomains also aligned in opposition; however their net magnetic moment is non-zero. This could be either due to the fact that one orientation of subdomains have weaker moment or that there is less domains with one of the orientations. Such substances are called ferromagnetic. Examples of the first type are magnetite, titanomagnetite, oxides of iron and titanium. The second group is represented by pyrrhotite.

The induced magnetization is directly proportional to the susceptibility and orientation of magnetic mineral present in the rocks. The orientation is, naturally, the same as that of the external field (geomagnetic field in our case). However, the measured magnetization is not always of this direction. That which is responsible for this phenomenon is the remanent magnetization. The remanent magnetization is present even if we remove the external magnetic field (Valenta, 2015). The mean values and ranges in susceptibility of common rock types are shown in Figure 1.9.

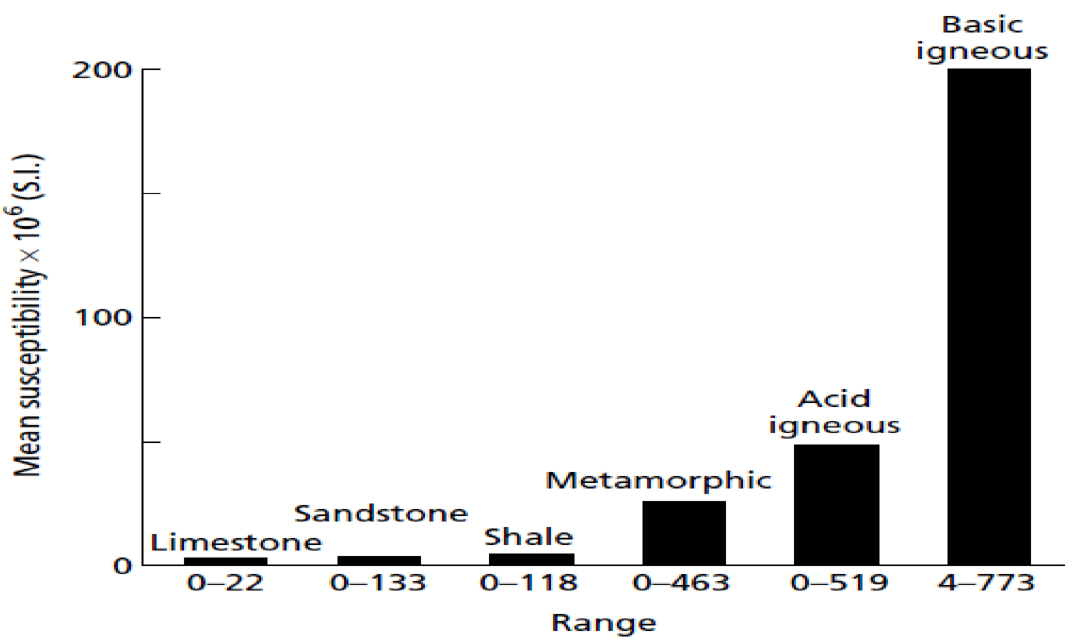

Figure 1.9: Histogram showing the mean values and ranges in susceptibility of common rock types (Dobrin and Savit, 1988)

1.9.1 Thermoremanent magnetization

This is created when magnetic material is cooled below the Curie temperature in the presence of external magnetic field (usually the earth's magnetic field). Its direction depends on the direction of the external field at the time and place where the rock is cooled (Telford *et al.,* 1990).

1.9.2 Detrital magnetization

This has fine-grained sediments. When magnetic particles slowly settle, they are oriented into a direction of an external field. Various clays exhibit this type of remanence (Telford *et al.,* 1990).

1.9.3 Chemical remanent magnetization

This is created during a grown of crystals or during an alteration of existing minerals. The temperature must be low (below the Curie temperature). This type might be significant in sedimentary or metamorphic rocks (Telford *et al.,* 1990).

1.9.4 Isothermal remanent magnetization: is the residual left following the removal of an external field. Its amplitude is low unless it was created within very large magnetic field like during the lightning strike (Telford *et al.,* 1990).

1.9.5 Viscous remanent magnetization

This` is produced by a long exposure to an external field. It grows with a logarithm of time. It is common for all rocks types, the direction is usually close to the direction of present magnetic field, is quite stable and an amplitude could be up to 80 % of the induced magnetization (Telford *et al.,* 1990).

1.9.6 Dynamic remanent magnetization

This is created when a rock is exposed to varying pressure within a magnetic field. The pressures could be of various types ranging from tectonic or seismic pressures up to hammer strikes (Telford *et al.*, 1990).

1.10 Geomagnetic Components

The earth's magnetic field at each point in space has strength and direction, that is, it is a direction quantity (Figure 1.10). To specify the field at any point three elements are needed;

- three orthogonal strength component (X, Y and Z)
- the total field strength and two angles (F,D,I) or
- two strength components and an angle (H,Z,D)

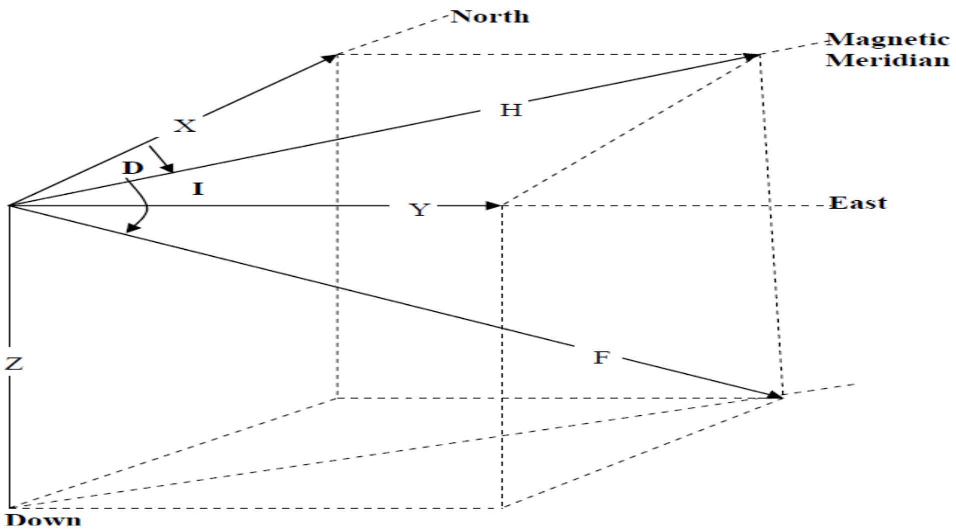

Figure 1.10: Geomagnetic field elements (Langel, 1987)

F is the total intensity of the magnetic vector, H is the horizontal component of the magnetic field vector, Z is the vertical component of the magnetic field vector (by convention Z is positive downward), X is the north component of the magnetic field, Y is the east component of the magnetic field, D is magnetic declination, defined as the angle between true north and the horizontal component of the field measured eastward from true north, I is magnetic inclination, defined as the angle measured from the horizontal plane to the magnetic field vector, downward is positive. D and I are measured in degrees. All other elements are measured in nano-Tesla (nT; 1 nT= 10^{-9} Tesla). The seven elements are related by the simple expressions.

Declination, D $= arctan\left(\frac{Y}{X}\right)$ (1.1)

Inclination, I$= arctan\left(\frac{Z}{H}\right) = \arctan \frac{Z}{(X^2+Y^2)^{1/2}}$ (1.2)

H= $(X^2 + Y^2)^{1/2} = FcosI$ (1.3)

If X= $HcosD, Y = HsinD$, the total intensity of the magnetic vector, F, is given as

$F^2 = X^2 + Y^2 + Z^2$ (1.4)

1.11 Objectives of the study

The objective of this study is to interpret qualitatively and quantitatively the aeromagnetic data of Ubiaja and Illushi areas located in the northern Anambra basin, south western Nigeria. This involves the use of source parameter imaging (SPI), spectral analysis, forward and inverse modelling and Euler deconvolution methods in determining:

(i) the depth to basement (sedimentary thickness) of the study area;

(ii) the possible minerals in the area;

(iii) the Rose diagram showing structural lineaments of the area.

CHAPTER TWO

LITERATURE REVIEW

2.1 Review of Previous Aeromagnetic Survey carried out in Anambra Basin and other basins

The making of the aeromagnetic data available by the Nigerian Geological Survey Agency (NGSA) has made the qualitative and quantitative interpretations of aeromagnetic data feasible. This enabled some researchers to carry out geophysical investigations on Anambra basin and some other basins in Nigeria.

Onwuemesi (1997) evaluated the depth to the basement (sedimentary thickness) using spectral analysis in the Anambra basin and found the sedimentary thickness to vary from 0.9 km to 5.6 km. Jacques *et al.* (2003) used gravity and magnetic data from Niger Delta in enhancing structural interpretation generally. They employed 2-D gravity and magnetic models to reveal major shale structures and transform faults in the study area.

Onuba *et al.* (2011) interpreted the aeromagnetic anomalies over Okigwe area and estimated the depth to basement using slope methods. They established two depth models. On the average the deeper magnetic sources range from 2.0 km to 4.99 km while the shallower magnetic sources range from 0.4 km to 1.99 km. They did not recommend hydrocarbon exploration in the area since their result shows low thickness of sediments on the average.

Ali *et al.* (2012) carried out geomagnetic modelling of potential hydrocarbon traps in the lower Niger Delta, offshore West Africa. In the study, eleven intrusives were mapped and the lateral extents range from 1.5 km to 6 km. Due to the presence of intrusives, part of the study area is less favourable for hydrocarbon especially the northern and northcentral parts. Also southwest, southeast and parts of the south are dominated by these features. In essence, the more the intrusives, the more the geothermal energy to be released to the source rocks and the more likelihood for them to become over matured as the geothermal temperature widens when their maturation is exceeded. They noticed that several oil producing fields were reportedly situated around the structurally low areas of the Niger Delta basin. Ugwu and Ezema (2012) carried out forward and inverse modelling of aeromagnetic data over Abakaliki and Nkalagu areas of the lower Benue trough, Nigeria. The anomalies over the study area were modeled by spherical, prismatic or dyke-like bodies. These bodies were emplaced at various depths between 2 km to 22 km, either within the cretaceous sediment or in the basement. The magnetic susceptibility of most of these bodies, as revealed by the model results, indicated that the bodies were igneous rocks.

Okiwelu *et al.* (2013) performed directional horizontal derivatives, analytical signal, filtering of magnetic data sets and 3-D magnetic modelling incorporating induced and remanent magnetization on low resolution aeromagnetic data to unravel the basement structure and its relationship with hydrocarbon target offshore Niger Delta basin. The 3-D magnetic modelling results of six bodies reveal a maximum depth of 12 km. Further results from the study, revealed structural highs (basement highs), structural lows (basement lows) and steep or faulted flanks which are attractive sites for oil and gas accumulation. Ugwu *et al.* (2013) interpreted aeromagnetic data over Okigwe and Afikpo areas of lower Benue trough of Nigeria using forward and inverse modeling technique. The anomalies over the study area were modeled using spherical or dyke-like bodies embedded at various depths ranging from 3.0 km to 12.7 km, either in the sediment or in the metamorphic basement. The magnetic susceptibilities of most of these bodies indicate that they are igneous intrusions. These intrusions with large lateral extents occurring more at Afikpo area than the Okigwe area account for more mineralization at Afikpo than at Okigwe. They employed only one method (forward and inverse technique) in their interpretation. Igwesi and Umego (2013) interpreted the aeromagnetic anomalies over some parts of the lower Benue trough, using only spectral analysis which indicated a two layer source model with depth for deeper magnetic source ranging from 1.16 km to 6.13 km with an average value of 3.03 km and depth to the shallower magnetic source ranging from 0.016 km to 0.37 km with an average value of 0.22 km. Adetona and Abu (2013) estimated the thickness of sedimentation within the lower Benue basin and upper Anambra basin. They employed only spectral depth analysis which used the radial average energy spectrum to obtain a depth of 7.3 km and source parameter imaging to obtain a depth of 9.847 km. Ikumbur *et al.* (2013) carried out spectral analysis of aeromagnetic data over part of the southern Bida basin, west-central Nigeria. They found out that the area revealed two depth sources in the area, the deeper sources range from 2.81 km to 3.24 km, while the shallower sources range from 0.45 km to 1.49 km. The result also shows a linear depression with sedimentary accumulation trending east to west. The average sedimentary thickness in the region is about 2.90 km.

Ezema *et al.* (2014) used forward and inverse modeling to interpret the aeromagnetic data of Abakaliki which gave or showed maximum depths of 4.96 km to 9.8 km with minimum depth ranging from 0.12 km to 0.17 km. Nwosu (2014) determined the depth to magnetic basement of parts of middle Benue trough by source parameter imaging (SPI) technique using high resolution aeromagnetic (HRAM) data. The SPI technique revealed two magnetic anomaly source bodies, the deeper lying magnetic source bodies and the shallow seated magnetic sources. The deeper lying magnetic bodies had thicker sedimentary cover ranging from 2.10 km to 6.29 km with an average depth of 3.25 km and could be viewed as the magnetic basement depth of the study area. The shallow seated magnetic source bodies of thinner sediment ranged from 1.59 km to 2.00 km with an average depth of 1.08 km. They may be regarded as magmatic intrusions into the sedimentary basins and these may be responsible for the lead-zinc mineralization found in the area.

Emujakporue and Ofoha (2015) carried out spectral depth estimation of subsurface structures over parts of offshore Niger Delta, Nigeria. They found out that the areas with deep lying magnetic bodies have sedimentary thickness ranging from 5600 m to 13636 m with an average depth of 9466 m, whereas the shallow source bodies have depths ranging from 1250 m to 3684 m with an average of 2467 m. From the average depth of the deep lying magnetic bodies, 9466 m, they suggested that the sediments are thick enough for the accumulation of hydrocarbon if other conditions are favourable. Onwe *et al.* (2015) carried out the estimation of sedimentary thickness in the eastern Anambra basin by qualitative and quantitative interpretation of aeromagnetic data using peter's half slope method and found a linear depression with thicker sediment accumulation trending northeast to southwest. Their result also reveal that the depth to sedimentary thickness is from 3.50 km to 7.00 km which could be associated to near surface magnetic sources that intruded into the magnetic bodies within the sedimentary cover. Akanbi and Fakoya (2015) carried out regional magnetic field trend and depth to magnetic source determination from aeromagnetic data of Maijuju area, north-central Nigeria. They found out that the regional magnetic field trend as observed from the upward continuation process is northeast to southwestern trend while the spectral depth analysis result revealed that the deeper sources range from 1.19 km to 2.01 km with an average depth of 1.47 km while the shallow depth range from 0.34 km to 0.39 km with an average of 0.36 km. Obiora *et al.* (2015) interpreted aeromagnetic data of Nsukka area, Enugu state, Nigeria, for hydrocarbon exploration using SPI, inverse and forward modeling and Euler deconvolution techniques. The result for SPI estimated depth ranges from 151.6 m (outcropping and shallow magnetic bodies) to -3082.7 m (deep lying magnetic bodies). 35 m to 150 m depths are good potential water reservoir for Nsukka and environs and depths of 1644 m to 3082.7 m show sufficient thick sediments suitable for hydrocarbon accumulation. They also found out that the possible mineral in the area are quartzite, hematite, pyrrhotite, limonite and pyrite. They however did not employ spectral analysis. Apart from the work of Obiora *et al.* (2015), the works of other researchers depend mostly on one or combination of two methods.

In this work, four methods will be employed in estimating the sedimentary thickness (depth to basement) of the study area.

CHAPTER THREE

MATERIALS AND METHOD

3.1 Theory of magnetic force

Magnetic force is similar to the force that exists between two point charges as stated by Coulomb (1736−1806). Coulomb showed that the force of attraction or repulsion between two electrically charged bodies and between magnetic poles (dipoles) obeys an inverse square law like denoted by Newton for gravity.

An inverse square law for the force F between magnetic poles with strengths p_1 and p_2 at distance r from each other is expressed as;

$$F(r) = k\frac{p_1 p_2}{r^2} \tag{3.1}$$

From equation (3.1), if $k = \frac{1}{\mu}$, the magnetic force becomes;

$$F(r) = \frac{1}{\mu}\frac{p_1 p_2}{r^2} \tag{3.2}$$

The constant μ is known as the magnetic permeability, p_1 and p_2 are the strengths of the two magnetic monopoles, and r is the distance between the two poles.

3.2 Magnetic Field Strength, H

The magnetic field strength at a point is defined as the force per unit of pole strength which would be exacted upon a small pole of strength $p_1$if placed at that point. That is;

$$H = \frac{F(r)}{p_1} \tag{3.3}$$

Substituting equation (3.2) into equation (3.3), we will have;

$$H = \frac{p_2}{\mu r^2} \quad (3.4)$$

The field strength, H, due to a pole of strength p at a distance r away can simply be written as;

$$H = \frac{F(r)}{p_1} = \frac{p}{\mu r^2} \quad (3.5)$$

The magnetic field strength is often expressed in terms of the density of the lines of force or flux representing the field. The SI unit of magnetic field strength H is the nanoTesla or nT.

3.3 The Magnetic Potential

The magnetic field has field just as the gravitational field. The potential of a magnetic field is simply the work necessary to bring a unit magnetic pole from infinity to a point of distance r from another source of magnetic polarity of strength, p. The magnetic potential U can be expressed as:

$$U = \frac{1}{\mu}\frac{p}{r} \quad (3.6)$$

where U is the magnetic potential, p is the strength of magnetic polarity, R is the distance and μ is the magnetic permeability.

3.4 Magnetic Susceptibility (k)

Magnetic susceptibility (k) is the extent to which a material may be magnetized in relation to a given applied magnetic field. Mathematically,

$$I = kH \quad (3.7)$$

And

$$k = \frac{I}{H} \quad (3.8)$$

where k is the proportionality constant called susceptibility, H is the magnetic field strength and I is the intensity of magnetization. The magnetic susceptibilities of some minerals and rocks are given in Table 3.1. This shows the type of intrusive rocks and their respective average magnetic susceptibility.

Table 3.1: Magnetic susceptibility of some minerals and rocks (Telford *et al.*, 1990)

	Susceptibility $\times$ $\mathbf{10^{-3}}$ ($\boldsymbol{SI}$)	
Type	***Range***	***Average***
Sedimentary		
Limestones	0—3	0.3
Sandstones	0—20	0.4
Shales	0.01—15	0.6
Metamorphic		
Schist	0.3—3	1.4
Gneiss	0.1—25	
Slate	0—35	6
Igneous		
Granite	0—50	2.5
Porphyry	0.3—200	60
Gabbro	1—90	70
Basalts	0.2—175	70
Mineral		
Quartz		−0.01
Coal		0.02
Hematite	0.5—35	6.5
Magnetite	1200—19200	6000

3.5 Magnetic instruments

Magnetic instruments are divided into two namely:

(i) mechanical instruments

(ii) magnetometers

Mechanical instruments are instruments that operate based on the movement of machines and usually measure the attitudes (its direction or a component of its direction) of the magnetic field. Examples are mariner's compass or the Swedish mining compass used for measuring the dip and declination, a simple compass used for free rotation in a horizontal plane, magnetic variometer or dip needle with high sensitivity used for measuring Z and H, dip needles for measuring the declination of magnetic field, Torsion magnetic instruments for measuring the strength of the vertical component of the magnetic field.

Magnetometers are instruments for measuring the strength and sometimes the direction of magnetic field including those on or near Earth and in space. Magnetometers are also used to calibrate electromagnets and permanent magnets and to determine the magnetization of materials. The development of magnetometer is effective in exploration in making large number of readings over a given area of interest in a reasonably short space of time.

3.6 Airborne Magnetometers

3.6.1 Proton precession magnetometer

For land-based magnetic surveys, the most commonly used magnetometer is the proton precession magnetometer (Figure 3.2). Unlike the fluxgate magnetometer, the proton precession magnetometer measures the total amplitudes (size) of the Earth's magnetic field. The most commonly used magnetometer for both survey work and observatory monitoring is currently the nuclear precession or proton magnetometer. The sensing device of the proton magnetometer is a container filled with a liquid rich in hydrogen atoms, such as kerosene or water, surrounded by a coil (Figure 3.1a). The hydrogen nuclei (protons) act as small dipoles and normally align parallel to the ambient geomagnetic field B_e (Figure 3.1b). A current is passed through the coil to generate a magnetic field, B_p, $50\ to\ 100$ times larger than the geomagnetic field, and in a different direction, causing the protons to realign in this new direction (Figure 3.1c). The current to the coil is then switched off so that the polarizing field is rapidly removed. The protons return to their original alignment with B_e by spiraling, or precessing, in phase around this direction (Figure 3.1d) with a period of about 0.5 ms, taking some 1 to 3 s to achieve their original orientation. The frequency f of this precession is given by

$$f = \frac{\gamma_p B_e}{2\pi} \tag{3.9}$$

where γ_p is the gyromagnetic ratio of the proton and B_e is the ambient geomagnetic field

Consequently, measurement of f, about 2 kHz, provide a very accurate measurement of strength of the total geomagnetic field f, is determined by measurement of the alternating voltage of the same frequency induced to flow in the coil by the precessing protons.

Field instruments provide absolute readings of the total magnetic field accurate to ± 0.1 nT although much greater precision can be accurately oriented, although it should ideally lie at an appreciable angle to the total field vector. Consequently, reading may be taken by sensors towed behind ships or aircraft without the necessity of orienting mechanism. Aeromagnetic surveying with proton magnetometers may suffer from the slight disadvantage that readings are not continuous due to the finite cycle period. Small anomalies may be missed since an aircraft travels a significant distance between the discrete measurements, which may be spaced at intervals of a few seconds. This problem has been largely obviated by modern instruments with recycling periods of the order of a second. The proton magnetometer is sensitive to acute magnetic gradients which may cause protons in different parts of the sensor to precess at different rates with a consequence adverse effect on precession signal strength.

Many modern proton magnetometers make use of the *overhauser effect*. The difference between the free-proton magnetometer and the overhauser-effect magnetometer is that the free-precession magnetometer makes use of a magnetic field to polarize the protons, while the overhauser-effect magnetometer uses a similar proton-rich fluid but adds a solution rich in paramagnetic ions. While magnetometers using the overhauser effect produce a continuous output signal, a finite amount of time is still required to count the proton-precession frequency. The overhauser effect does not change the proton gyromagnetic ratio; thus the overall frequency of this magnetometer is no different than that of the free-precession type. The major advantages are slightly increased precession signal strength and the ability to sample more rapidly. Maximum sampling rates that can realistically be achieved are 8 to 10 per second, but at these rates the sensitivity is limited (Kearey, 2002).

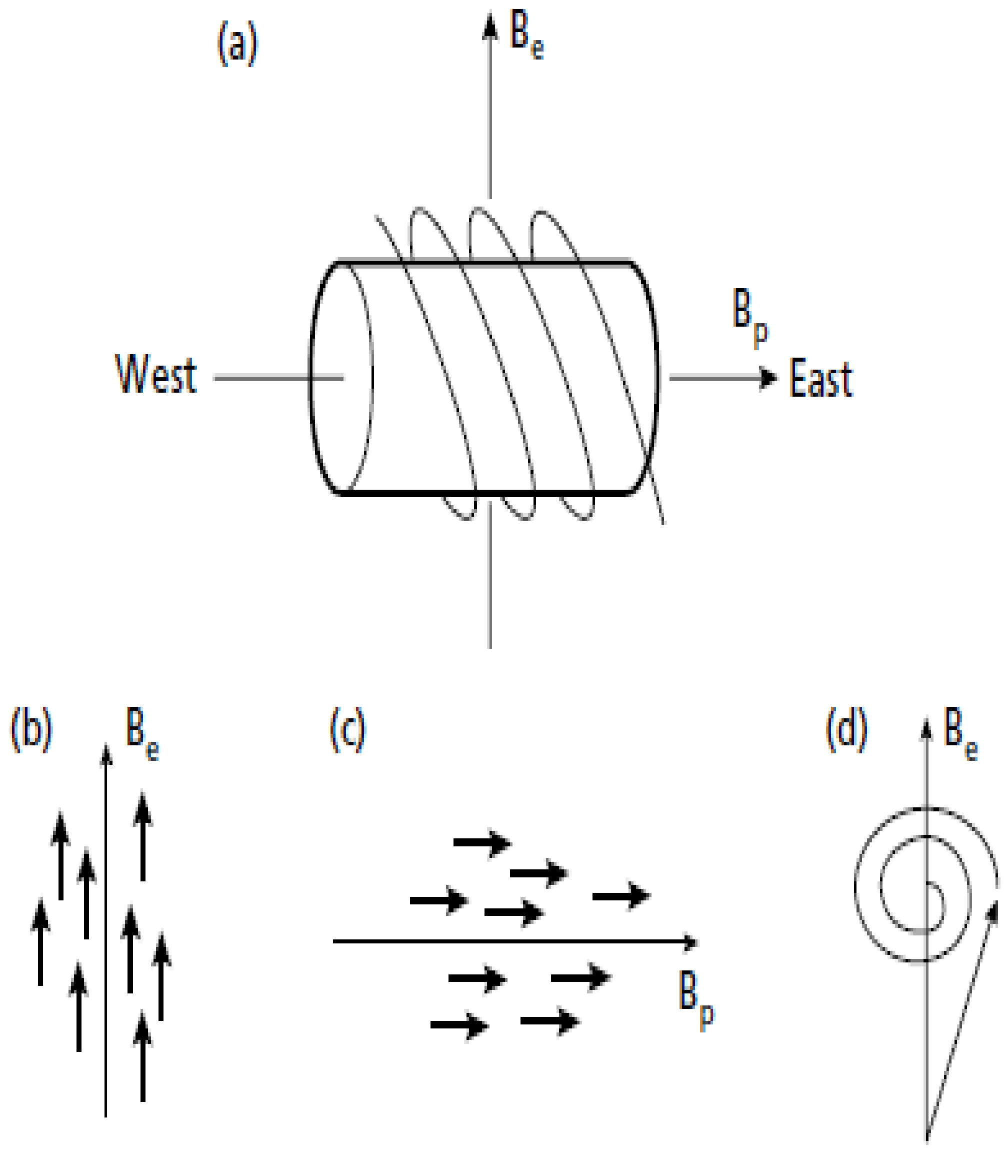

Figure 3.1: Principle of the proton magnetometer (Kearey *et al.*, 2002)

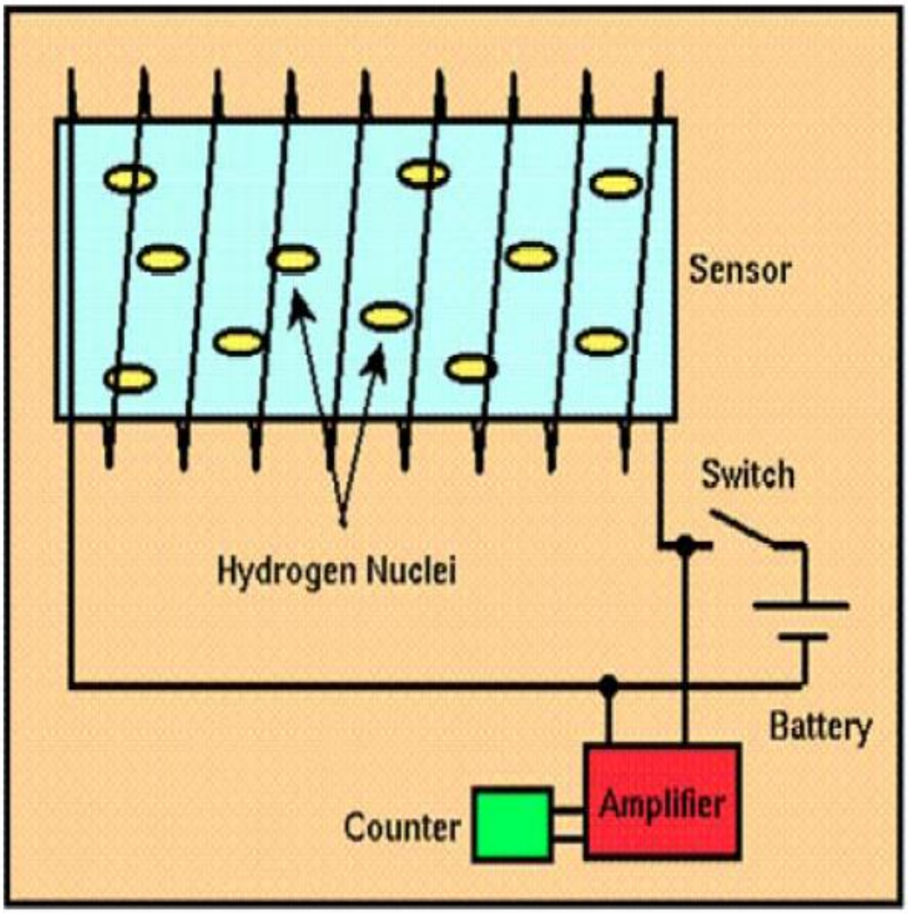

Figure 3.2: A schematic of the proton precession magnetometer (Ariffin, 2012).

3.6.2 Fluxgate magnetometer

The fluxgate magnetometer (Figure 3.3) was originally developed during World War II. It was built for use from low-flying aircrafts as a submarine detection device. Today it is used for making borehole measurements, and transducers are found in electronic compasses and in laboratory devices for measuring remanent magnetization. A schematic of the fluxgate magnetometer is shown in Figure 3.3.

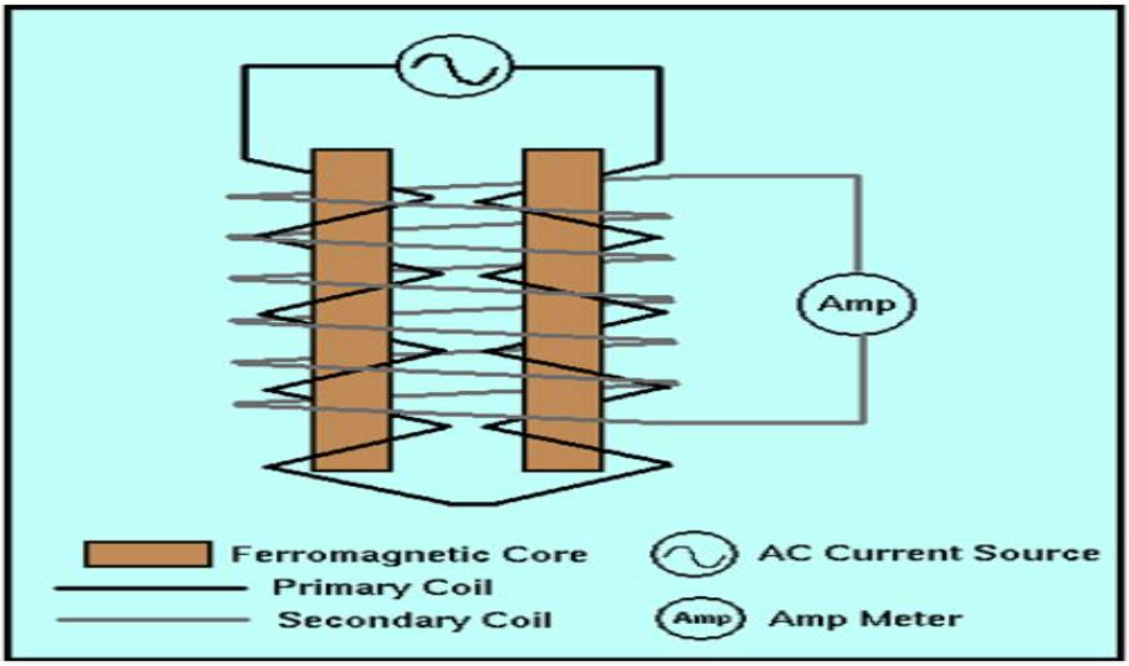

Figure 3.3: A schematic of a fluxgate magnetometer (Ariffin, 2012).

The fluxgate magnetometer is based on what is referred to as the 'magnetic saturation circuit'. Two parallel bars of a ferromagnetic material are placed closely together. The susceptibility of the two bars is large enough so that even the Earth's relatively weak magnetic field can produce near magnetic saturation in the bars.

Each bar is wound with a primary coil, but the direction in which the coil is wrapped around the bars is reversed. An alternating current (A.C.) is passed through the coils causing a large, artificial, and varying magnetic field in each coil. This produces induced magnetic fields in the two cores that have the same strengths but opposite orientations, at any given time during the current cycle. If the cores are in an external magnetic field, one component of the external field will be parallel to the core axes. As the current in the primary coil increases, the magnetic field in one core will be parallel to the external field and so reinforced by it. The other will be in opposition to the external field and so smaller. The field will reach saturation in one core at a time different from the core (and fall below saturation, as the current decreases, at a different time). This difference is sufficient to induce a measurable voltage in a secondary coil that is proportional to the strength of the magnetic field in the direction of the cores.

The secondary coil surrounds the two ferromagnetic cores and the primary coil. The magnetic fields induced in the cores by the primary coil produce a voltage potential in the secondary coil. In the absence of an external field (i.e., if the earth had no magnetic field), the voltage detected in the secondary coil would be zero because the magnetic fields generated in the two cores have the same strength but are in opposite directions (their effects on the secondary coil exactly cancel). In the presence of an external field component, the behaviour in the two cores differs, by an amount which depends on the external field.

Thus, the fluxgate magnetometer is capable of measuring the strength of any component of the Earth's magnetic field by simply reorienting the instrument so that the cores are parallel to the desired component. Fluxgate magnetometers are capable of measuring the strength of the magnetic field to about 0.5 nT to 1.0 nT (Kearey, 2002).

3.6.3 Optically pumping magnetometer

Optically pumped or alkali vapour magnetometer have a significantly higher precession than other types. They comprise of a glass cell containing an evaporated alkali metal such as caesium, rubidium, or potassium which is energized by light of a particular wavelength (Kearey, 2002).

The physical principle of an optically absorption magnetometer is known as larmor precession. In the presence of an external magnetic field, the orbital motion of a charged particle such as an electron in its orbit around an atomic nucleus precesses (that is, wobbles in the fashion of a spinning top) about the direction of the magnetic field. The angular frequency in this precession is directly proportional to the magnitude of the magnetic field; each of the elements will have a larmor frequency known as the constant of proportionality.

3.7 Gradiometer

This measures the magnetic field gradient rather than total field strength, which allows the removal of background noise. Magnetic gradient anomalies generally give a better definition of shallow buried features such as buried tanks and drums, but are less useful for investigating large geological features. Unlike EM surveys, the depth penetration of magnetic surveys is not impeded by high electrical ground conductivities associated with saline groundwater or high levels of contamination.

3.8 Aeromagnetic Data Filtration

Filtering is done to remove or eliminate noise (unwanted signal). Filtration is a way of separating signals of different wavelength in order to isolate and hence, enhance anomalous features with certain wavelength. WinGLink and Surfer-11 softwares were employed in the processing of data in this work. These data processing techniques include gridding, regional-residual separation, first vertical derivative, first horizontal derivative and reduction to pole. There are many aeromagnetic data filtering, some used in this work are discussed below:

3.8.1 Polynomial fitting

The regional and residual anomaly maps are achieved by carrying out polynomial fitting of any degree. Polynomial fitting of degree 1 and 2 were done in order to get the residual anomaly and regional anomaly maps and see how the degree of polynomial fitting affects the appearance of maps. The equation used to generate the algorithm for the removal of regional field according to Nwankwo (2006) is given as:

$$r = a_0 + a_1\left(X - X_{ref}\right) + a_2(Y - Y_{ref}) \quad (3.10)$$

where r is the regional field, X_{ref} and Y_{ref} are the X and Y coordinates of the geographic centre of the data set respectively. They are used as X and Y offsets in the polynomial calculation to prevent high order coefficients becoming very small and a_0, a_1 and a_2 are the regional polynomial coefficients. The residual field is the difference between the observed magnetic (which is the total magnetic intensity) field and the regional field value computed.

3.8.1.1 Regional-residual separation

The traditional filtering method can either be low pass (regional) or high pass (residual). Regional anomaly is referred to as the component of magnetic anomaly that has higher wavelength. This deep large feature shows up as regional trend and continues smoothly over a wider aerial extent. The residual anomaly has shorter wavelength and shows up as smaller, local trend which are secondary in size but primary in importance. These residual anomalies may provide structures for mineral ore emplacement. For effective interpretation to take place, the regional and the residual anomalies must be separated. Generally only the residual or local variations are of interest and hence, interpretation is based on it.

3.8.2 Derivatives

Derivative helps to sharpen the edges of anomaly and enhance shallow features (Telford *et al.*, 1990). This includes first and second vertical derivatives, first horizontal derivative, second horizontal derivative, etc.

3.8.2.1 Vertical derivative

Computation of the first vertical derivative in an aeromagnetic survey is equivalent to observing the vertical gradient with a magnetic gradiometer with advantages of enhancing shallow sources, suppressing deeper ones and giving a better resolution of closely-spaced sources. Hence the second, third and higher order vertical derivatives can be computed but usually noise in the data becomes more prominent than the signal in the first vertical derivative because of the Fast Fourier Transform (FFT) used. The FFT is given by:

$$F(\omega) = \omega^n \qquad (3.11)$$

3.8.2.2 Horizontal derivative

This is also calculated noting that a direction (azimuth) needs to be chosen, giving another element of choice for optimum presentation. Alternatively, the maximum horizontal gradient at each grid point can be displayed, regardless of direction. The horizontal gradient in this work will be filtered in x and y directions (Telford *et al.,* 1990).

3.8.3 Reduction to pole

This method entails removing the dependence of magnetic data on the magnetic inclination, which is converting data which were recorded in the inclined Earth's magnetic field to what they would have been if the magnetic field had been vertical. This method simplified the interpretation because for sub-vertical prisms or sub-vertical contacts (including faults), it transforms their asymmetric responses to simpler symmetric and anti-symmetric forms. The symmetric "highs" are directly centred on the body, while the maximum gradient of the anti-symmetric dipolar anomalies coincides exactly with the body edges. Reduction to pole was performed on the digitized aeromagnetic data of the study area (Figure 4.2) via Fast Fourier filtering programs in order to remove the dipolar nature of the magnetic field (Baranov and Naudy, 1964; Blakely and Simpson, 1986).

3.9 Method of Data Analysis

The first step was to reassemble the two maps covering the survey area. The data was digitized and provided in excel format which was converted from the excel format to text format. The data in text format was imported to the WinGLink software and the Total magnetic Intensity map (TMI) was produced. Various filtering processes were done and maps generated which were exported to the contouring software (surfer 11). The rose diagram or the circular histogram was gotten from Rozeta software which shows the structural lineament of the study area. The depths were gotten from the grids of Source Parameter Imaging (SPI), standard Euler deconvolution and spectral analysis and modelling.

3.10 Sorting and Arrangement of Data

The aeromagnetic data was carefully selected to include the data points that fall within latitude 6°30′N – 7°00′N and longitude 6°00′E - 7°00′E (study area). The longitude and latitude was originally given in degrees but was converted to metres by the WinGLink and the Oasis Montaj softwares.

3.11 Interpretation

This is the process of applying general principles (which may be qualitative or quantitative) to the explanation of the results obtained from a geophysical survey. The objective of interpretation in a survey is to:

(i) improve the description of the configuration of rocks in the ground that give rise to anomalies (e.g. geological mapping of poorly exposed or unexposed areas);

(ii) set limits to the depth, size, areal extent and so on, of each body causing an anomaly (Reeves, 2005)

3.11.1 Qualitative interpretation

Qualitative interpretation involves the description of the survey results and the explanation of the major features revealed by a survey in terms of the types of likely geological formations and structures that give rise to the evident anomalies. Typically, some geological information is available from outcrop evidence within the study area (or nearby) and very often the role of the geological data is to extend this geological knowledge into areas where there is no outcrop information (that is, extrapolation from the known to the unknown) or to extend mapped units into the depth dimension (Reeves, 2005).

3.11.2 Quantitative interpretation

This involves making numerical estimates of the depths and dimension of the sources of anomalies and this often takes the form of modelling of sources which could in theory replicate the anomalies recorded in the survey. In other words, conceptual models of the subsurface are created and their anomalies calculated in order to see whether the earth-model is consistent with what has been observed, that is, given a model that is a suitable physical approximation to the known geology, the theoretical anomaly if the model is calculated (forward modelling) and compared with the observed anomaly. The model parameters are then adjusted in order to obtain a better agreement between the observed and the calculated anomalies (Reeves, 2005). Quantitative interpretation involves the following methods: spectral analysis, source parameter imaging, Euler 3D deconvolution and modelling (forward and inverse) methods.

3.12 Spectral Analysis

Spectral analysis involves the measurement of the amplitude of the component of the complex waveform all through the frequency range of waveform. Spectral analysis is one of the most widely used methods for data analysis in geophysics, oceanography, atmospheric science, astronomy, engineering and so on. The Fourier Transform expresses a magnetic field as an integral of sine / cosine wave, each defining a wave of amplitude A(k) and phase $\emptyset(k)$, where $k/_{2\pi} = 1/_{\lambda}$ is the wavenumber. Plotting $A(k)$ gives the amplitude spectrum and $A^2(k)$ gives the power spectrum (Telford *et al.*, 1990).

The spectral depth method is based on the principle that a magnetic field measured at surface can therefore be considered the integral of magnetic signatures from all depths. The power spectrum of the surface field can be used to identify average depths of source ensembles (Spector and Grant, 1970). This same technique can be used to attempt identification of the characteristic depth of the magnetic basement, on a moving data window basis, merely by selecting the steepest and therefore deepest straight-line segment of the power spectrum, assuming that this part of the spectrum is sourced consistently by basement surface magnetic contrast. A depth solution is calculated for the power spectrum derived from each grid sub-set, and is located at the centre of the window. Overlapping the windows creates a regular, comprehensive set of depth estimates. This approach can be automated, with the limitation however that the least squares best-fit straight line segment is always calculated over the same points of the power spectrum, which is performed manually, would not necessarily be the case.

The step-by-step analysis of aeromagnetic data using spectral analysis starts by digitizing the data in text format, after which the other processes follow. The summary of the processes is given by the flow chart in Figure 3.4.

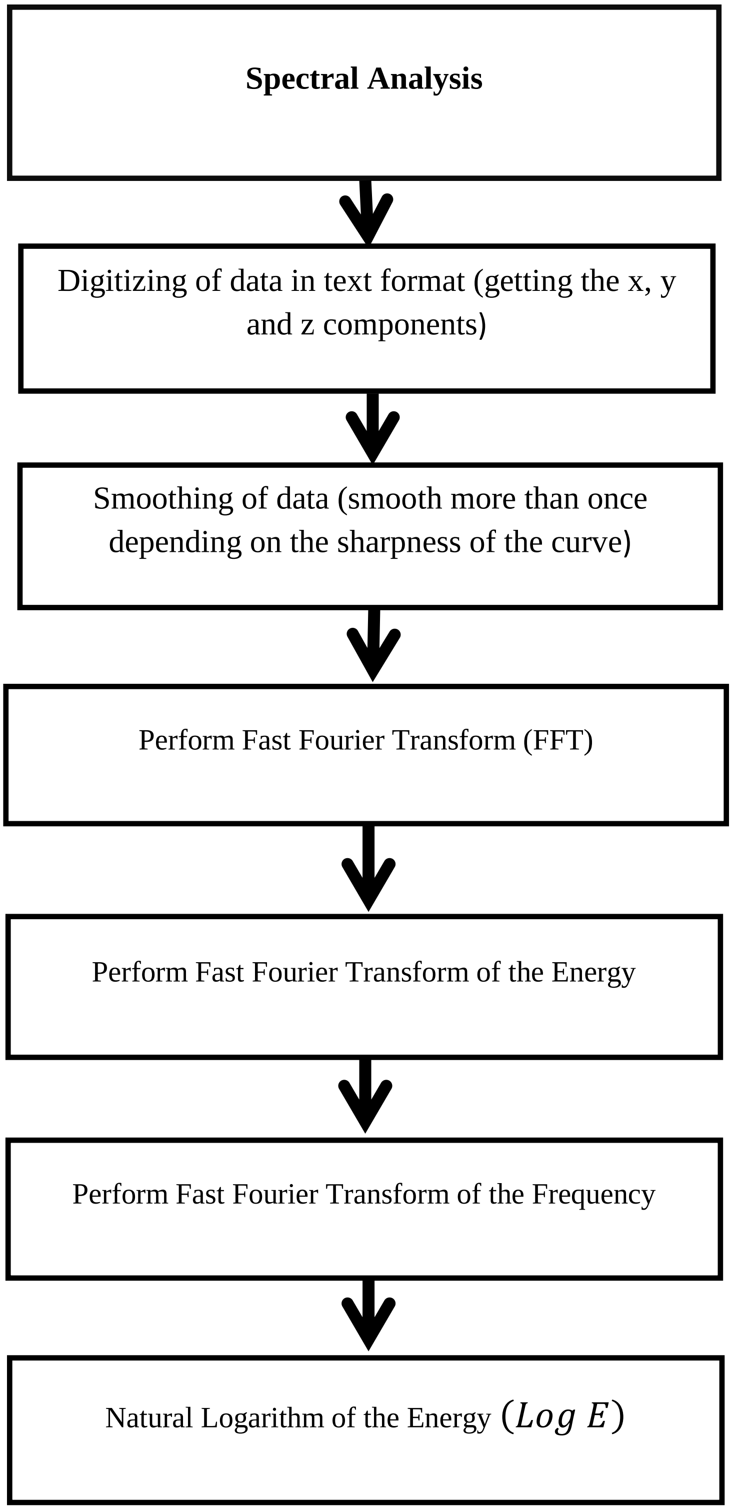

Figure 3.4: Spectral analysis procedure using Microsoft excel

3.12.1 Derivation of depth to basement from power spectrum

For an anomaly with n data points the solution of Laplace equation in 2D is written as;

$$M(x_j, z) = \sum_{j=0}^{n-1} A_k\, e^{i2\pi kx} e^{\pm 2\pi kz} \tag{3.12}$$

where wavenumber k is defined as $k = \frac{2\pi}{\lambda}$ and A_k are the amplitude coefficients of the spectrum given as;

$$A_k = \sum_{j=0}^{n-1} M(x_j, z)\, e^{-i2\pi kx_j} e^{\pm 2\pi kz} \tag{3.13}$$

For $z = 0$, equation (3.13) becomes,

$$(A_k)_0 = \sum_{j=0}^{n-1} M(x_j, 0)\, e^{-i2\pi kx_j} \tag{3.14}$$

Equation (3.13) can be written in terms of equation (3.14) as;

$$A_k = (A_k)_0\, e^{\pm 2\pi kz} \tag{3.15}$$

The power spectrum P_k is defined as;

$$P_k = (A_k)^2 = (P_k)_0\, e^{\pm 4\pi kz} \tag{3.16}$$

Taking the natural logarithm of both sides, we have;

$$log_e P_k = log_e (P_k)_0 \pm 4\pi kz \tag{3.17}$$

The estimated depth of anomalous body from power spectrum (Spector and Grant, 1970) is given as;

$$h = -\frac{\log \Delta E}{4\pi \Delta f} = -\frac{1}{4\pi} \times slope = -\frac{m}{4\pi} \tag{3.18}$$

$$h = -\frac{m}{4\pi} \tag{3.19a}$$

where the slope (m) is $\frac{\log \Delta E}{\Delta f}$. According to Telford et al. (1990), the sedimentary thickness (Z) and depth (h) are related by the relation; $h = \frac{Z}{2}$.

Equation (3.19a) becomes;

$$\frac{Z}{2} = -\frac{m}{4\pi} \tag{3.19b}$$

Therefore; $Z = -\frac{m}{2\pi}$ (3.20)

where z is the sedimentary thickness, m is the slope of the graph, E is the spectral energy, f is the spectral frequency and the negative sign ($-$) indicates that the logarithm of energy against frequency has an inverse relationship.

3.13 Source Parameter Imaging (SPI)

SPI is a profile or grid-based method for estimating magnetic source depths for some source geometries, the dip and susceptibility contrast. The method utilizes the relationship between source depth and the local wave number (k) of the observed field, which can be calculated for any point within a grid of data via horizontal and vertical gradients (Thurston and Smith, 1997; Fairhead *et al.*, 2004). The fundamentals for SPI are that for vertical contacts, the peaks of the local wave number define the increase of depth. Mathematically,

$$Depth = \frac{1}{K_{max}} = \frac{1}{\left(\sqrt{(\partial Tilt/\partial x)^2 + (\partial Tilt/\partial y)^2}\right)_{max}} \tag{3.21}$$

where;

$$Tilt = \arctan\left(\frac{\partial T/\partial Z}{\sqrt{(\partial T/\partial X)^2 + (\partial T/\partial Y)^2}}\right) = \arctan\left(\frac{\partial T/\partial Z}{HGRAD}\right) \tag{3.22}$$

where HGRAD is the horizontal gradient, T is the total magnetic intensity (TMI), $\partial T/\partial X$, $\partial T/\partial Y$ and $\partial T/\partial Z$ are derivatives of T with respect to x, y and z (Thurston and Smith, 1997). The SPI method requires first and second order derivative and this reduces both noise in the data and interference effects. Oasis Montaj software will be employed in computing the SPI image and depth.

3.14 Euler-3D deconvolution method

Euler deconvolution is an interpretation tool in potential field for locating anomalous source and the determination of their depths using Euler's homogeneity relation (Reid *et al.,* 1990). The homogeneity relation is given as:

$$(x - x_0)\frac{\partial T}{\partial x} + (y - y_0)\frac{\partial T}{\partial y} + (z - z_0)\frac{\partial T}{\partial z} = N(B - T) \tag{3.23}$$

where, $\frac{\partial T}{\partial x}$, $\frac{\partial T}{\partial y}$ and $\frac{\partial T}{\partial z}$ represent first-order derivative of magnetic field along the x-, y- and z-directions respectively, and $(x_{0,}y_0, z_0)$ is the source position of a magnetic source whose total magnetic intensity field, T, is measured at (x, y, z). B is the regional value of the total field and N is the structural index. The Euler deconvolution image and depth will be computed using Oasis Montaj.

3.15 Forward and inverse modelling

Forward modelling involves the comparison of the calculated field (red curve) of a hypothetical source with that of the observed data (indicated by the blue curve); the model is adjusted in order to improve the fit for a subsequent comparison. Inverse modelling involves direct determination of some parameters of the source from the measured data. Potent is the software that will be used in the modeling of the aeromagnetic data. Potent is software for modelling the magnetic and gravitational effects of subsurface. The main concepts in potent include: Observation, Inversion, Model, Visualization and calculation.

3.16 Softwares used in this work

The softwares employed in this work include:

(i) Golden software – surfer-11 software

In this work the Surfer-11 software was used to get the 3D plot of the deep depth and the shallow depth and also to get their grids and contour maps. It is preferred because it is user friendly and one can also see major features such as the points of depression and elevation of the 3D plots.

(ii) WinGLink: in this work WinGLink was applied to the aeromagnetic data in the following areas:

(a) To get the Total Magnetic Intensity (TMI) map

(b) To conduct magnetic filtering such as first vertical derivative, first horizontal derivative, residual anomaly map, regional map and reduction to pole. The following filtering methods were further exported to Surfer-11 software to get the legend bar, bar scale and the coordinates of the maps.

(iii) Rozeta: This is a ma

(iv) pping software that projects a sphere onto a plane. In this work, Rozeta software was used to get the 'Rose diagram' or 'circular histogram'. The Rose diagram shows the lineation in an area which could be anomalies or faults. In this work the Rose diagram shows the major and minor anomaly trends.

(v) Oasis Montaj: This is used to produce an intelligent entity called a map. Oasis Montaj mapping and processing system (MAPS) is a Geosoft software that contains a variety of built-in data import, processing, analysis, visualization, mapping and integration capability platform for working with large volume spatial data. The system enables users to perform processing, editing, mapping and interpretation tasks.

In this thesis the Oasis montaj was used to achieve the following:

(a) Total Magnetic Intensity (TMI) Grid mapping

(b) Source Parameter Imaging (SPI) depth determination

(c) Standard Euler Deconvolution depth determination

(vi) Microsoft Excel: This is software that is used for doing various packages such as: analysis of data, perform various statistical analysis such as ANOVA etc., validating data, creating of spreadsheets, performing spectral analysis in geophysics etc. In this thesis Microsoft Excel is used to perform spectral analysis and the format of this is illustrated in Figure 3.4.

(vii) Potent: Potent is a software that is mostly used in performing modelling in geophysics. In this work the Potent software will be employed in modelling the TMI grid map in other to determine the susceptibility of the area which will in turn expose the type of mineralization in the area.

3.17 Source of Data

The study area (Ubiaja and Illushi) is covered by an aeromagnetic survey conducted by Nigerian Geological Survey Agency (NGSA) of Nigeria in 2009. The magnetometer used for the aeromagnetic data survey is '3 × scintrex CS2 Cesium vapour'. The aeromagnetic surveys were flown at 500 metres flight line spacing and 5000 metres tie line spacing with 75 m sensor mean terrain clearance. The average magnetic inclination for the area is $-12.7°$ while the declination for the area is $-1.6°$. The geomagnetic gradient was removed from the data collected in digitized form (X Y Z data). The data collected in digitized format has X and Y representing the longitude and the latitude respectively while the Z represents the magnetic intensity measured in nano-Tesla (nT). The flight path processing used is the 'Real Time Differential Global Positioning System (GPS)'.

CHAPTER FOUR

RESULTS AND DISCUSSION

4.1 Data Analysis and Results

Interpretation or analysis of aeromagnetic data was carried out qualitatively and quantitatively, which aims to improve the description of the configuration of the rocks in the ground that give rise to anomalies, also the lineament trends of major and minor anomalies and to set limits to the depth of each body causing an anomaly.

4.2 Qualitative Interpretation

4.2.1 Total magnetic intensity (TMI)

The TMI map is a combination of total signals both the anomalous and the common signal in an area. The TMI map was produced using Oasis Montaj software. The TMI map (Figure 4.1) shows magnetic intensity values ranging from -48.7 nT to 100.7 nT. The area is marked by both high and low magnetic signatures which could be attributed to several factors such as: difference in susceptibility, variation in depth, degree of strike and difference in lithology. The circular alignment of blue circular bodies in the northwest and central directions (Figure 4.1) in the TMI map suggests that the area could contain intrusive.

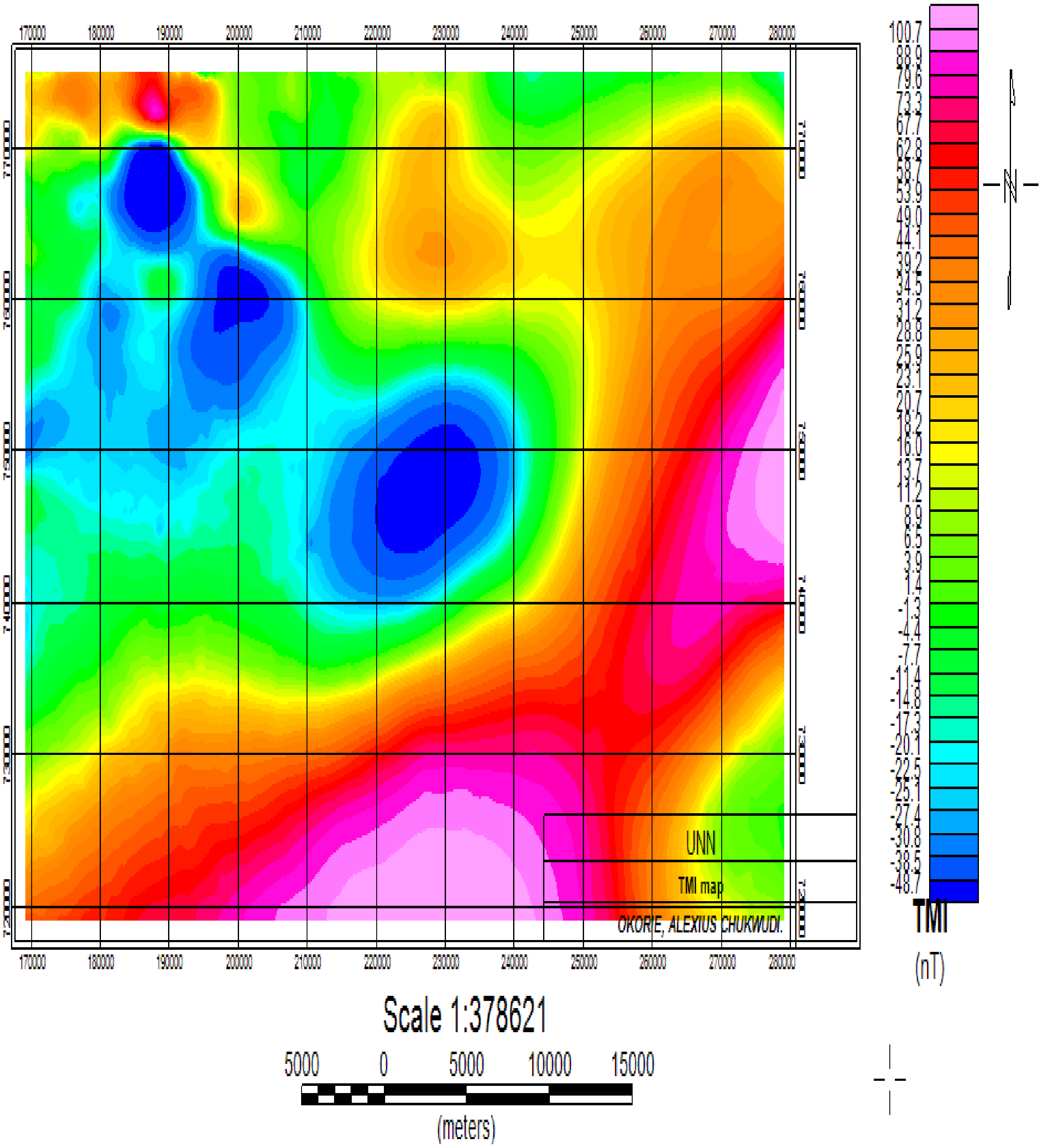

Figure 4.1: The TMI grid map from Oasis Montaj (contour intervals 10.2 nT)

4.2.2 Reduction to pole

The reduction to pole map (Figure 4.2) shows the magnetic intensity ranging from $-400\ nT$ to $450\ nT$. The magnetic intensity is concentrated at points A, B and C which is indicated by colour red from the colour legend bar at the right hand side of Figure 4.2. The areas of the lowest magnetic intensity are found in the northwestern and the southwestern parts of the study area as indicated by the blue colour from the colour legend bar. The northeastern part of the study area is characterized by neither high nor low (mid) magnetic intensity. WinGLink and surfer 11 were employed in producing the reduction to pole map (Figure 4.2)

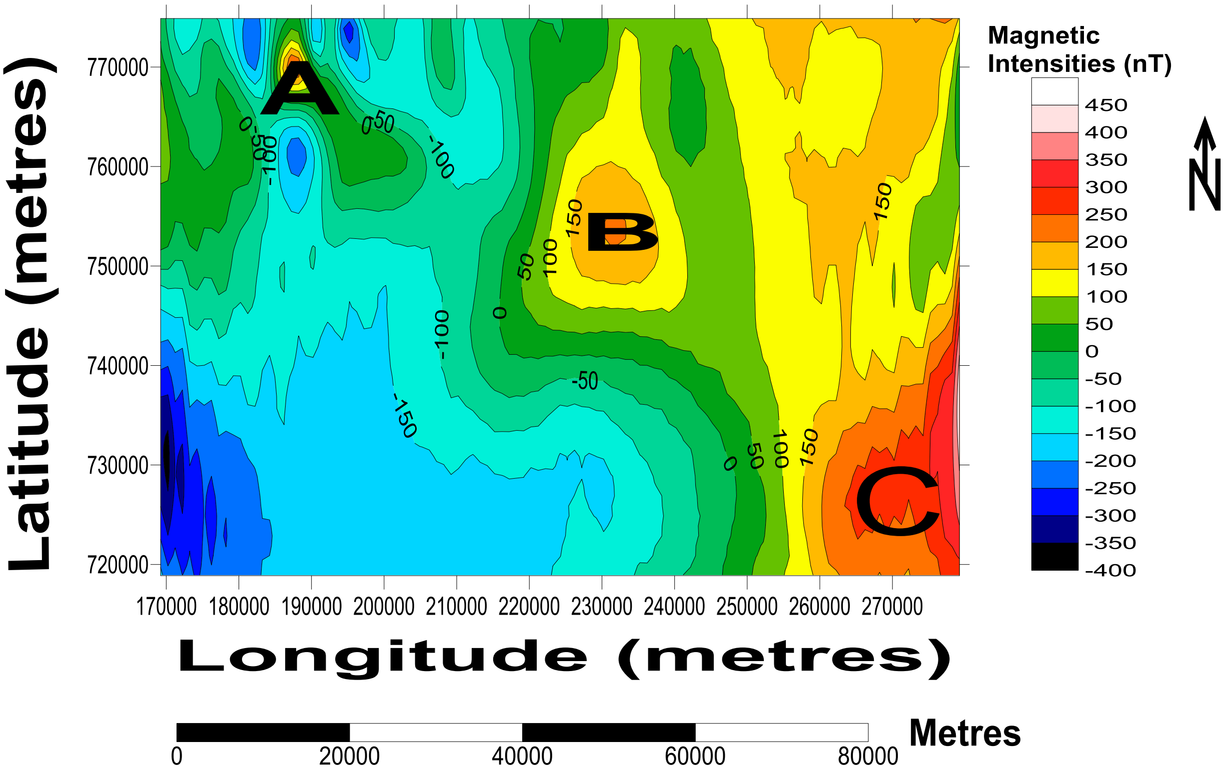

Figure 4.2: Reduction to pole map (contour interval $-50\ nT$)

4.2.3 Upward continuation

The upward continuation map (Figure 4.3) shows magnetic intensity ranging from $-40\ nT$ to $95\ nT$. The areas $K1$ and $K2$ show areas of high magnetic intensity as indicated by the colour legend bar which are found in the southern and eastern parts of the study area respectively. The areas $L1$, $L2$ and $L3$ show areas of low magnetic intensity as indicated by the colour legend bar which are found in the central and northwestern parts of the study area. WinGLink and Surfer 11 were employed in producing the upward continuation map (Figure 4.3)

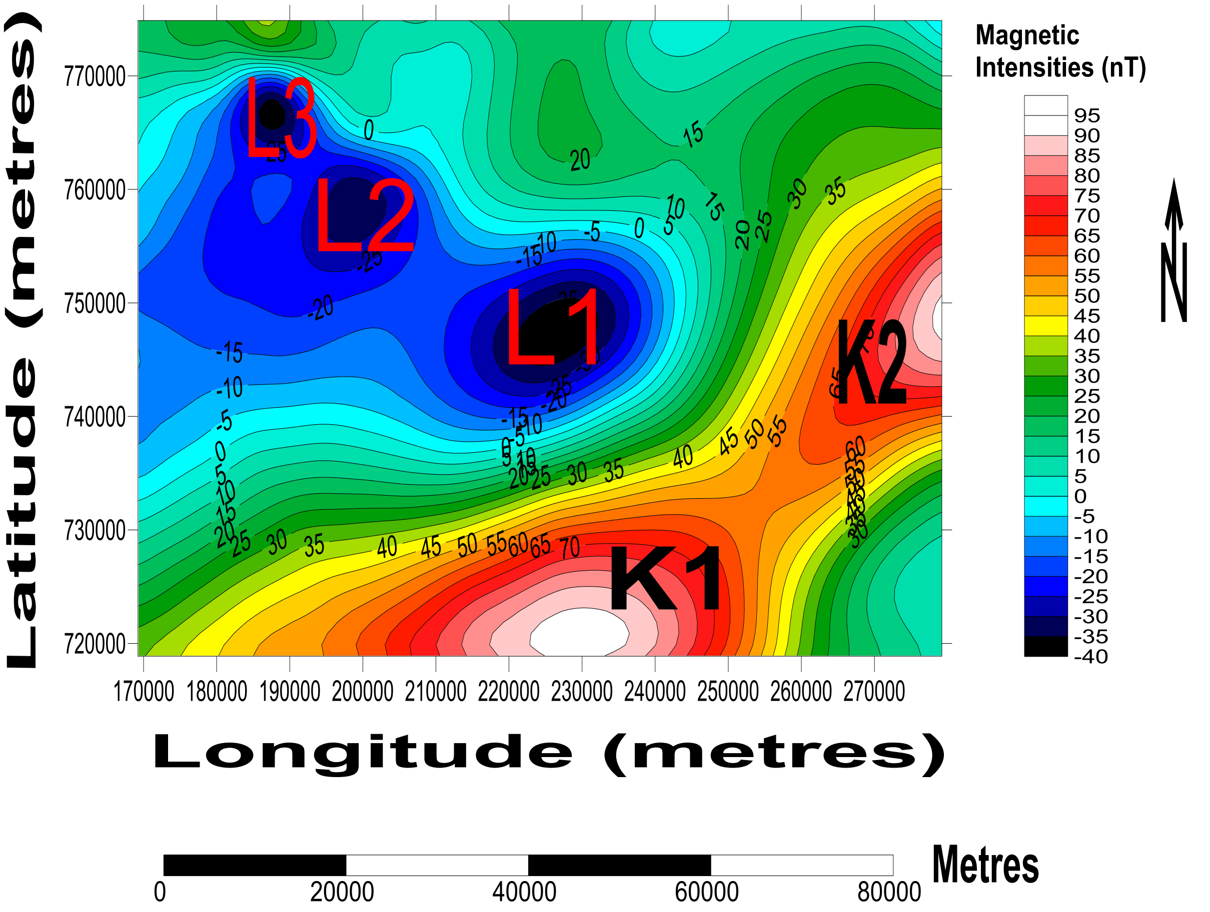

Figure 4.3: Upward continuation map (contour intervals $-5\ nT$)

4.2.4 Residual anomaly from polynomial fitting of degree 1 and 2

The residual anomaly map from polynomial fitting of degree 1 (Figure 4.4) shows the magnetic intensity ranging from $-90\ nT\ to\ 120\ nT$. From the map, the areas R1 and R2 which are found in the southern and eastern parts of the study area show areas of high magnetic intensity as indicated by the colour legend bar. The circular shaped contours found in the northwest and central parts of the study area show areas with low magnetic intensity as indicated by the colour legend bar. The residual anomaly map from polynomial fitting of degree 2 (Figure 4.5) shows the magnetic intensity ranging from $-100\ nT\ to\ 90\ nT$. From Figure 4.5, the areas D2 and D3 show areas of high magnetic intensity as indicated by the colour legend bar and the area D1 shows the boundary between the high magnetic intensity and low magnetic intensity.

WinGLink and Surfer 11 were employed in producing the residual anomaly maps (Figures 4.4 and 4.5)

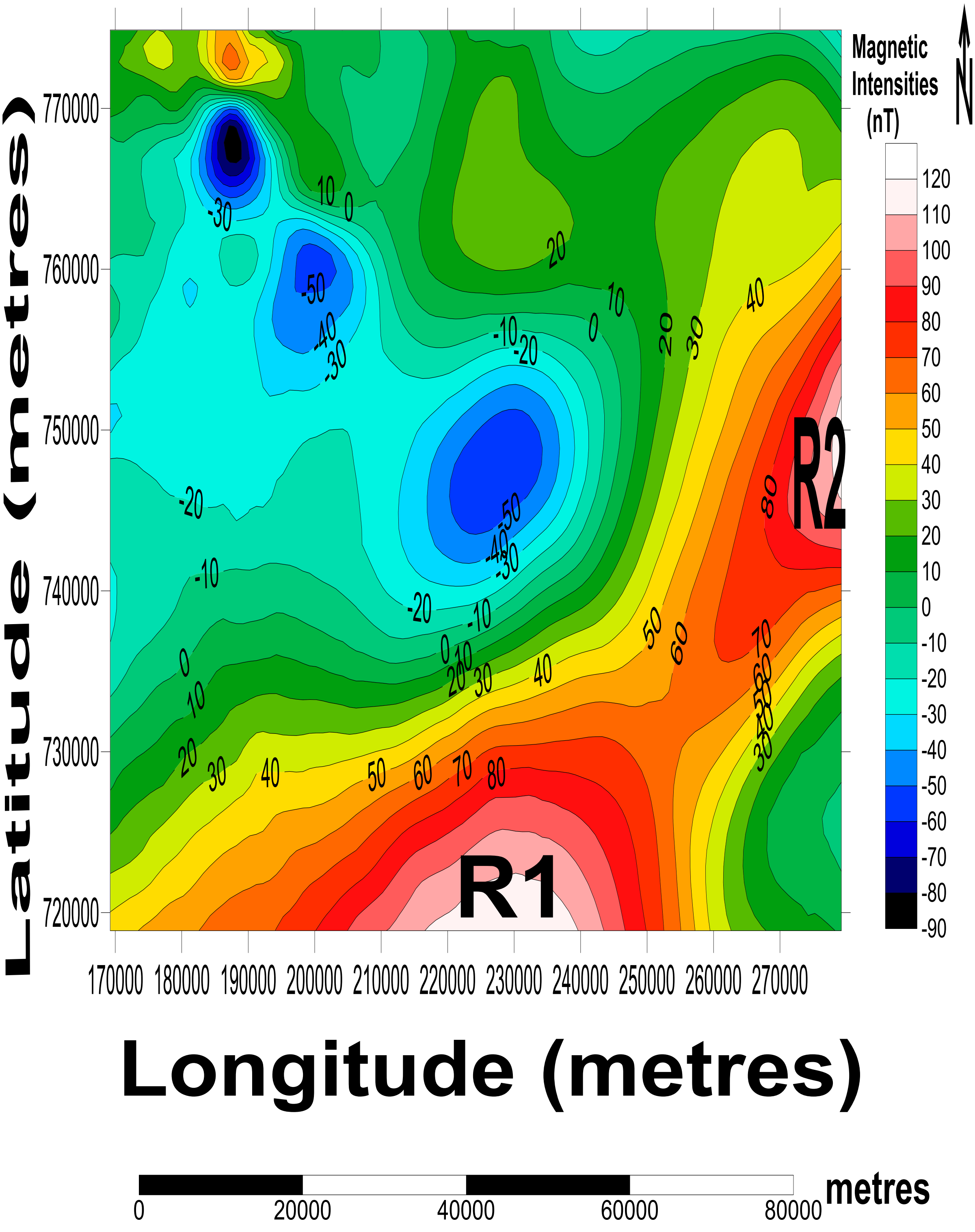

Figure 4.4: Residual anomaly map from polynomial fitting of degree 1 (contour intervals $-10\ nT$)

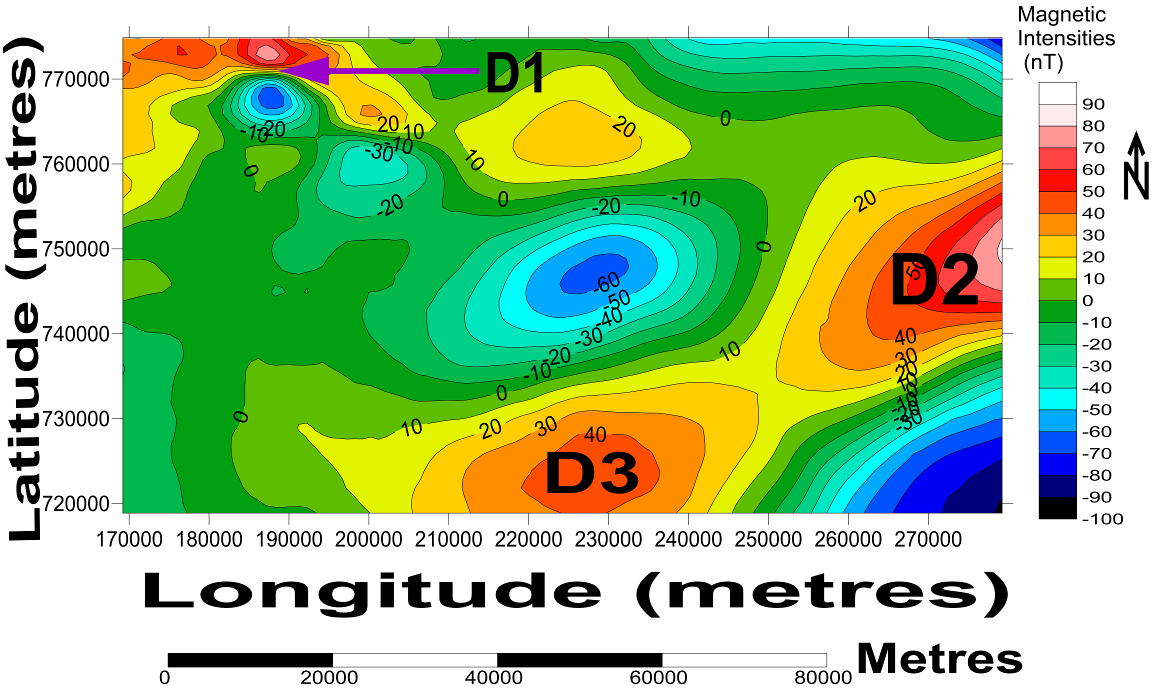

Figure 4.5: Residual anomaly map from polynomial fitting of degree 2 (contour intervals $-10\ nT$)

4.2.5 Regional anomaly from polynomial fitting of degree

The regional anomaly map from polynomial fitting of degree 1 (Figure 4.6) shows the magnetic intensity of the area ranging from $-45\ nT\ to\ 80\ nT$. The map shows an increase of magnetic intensity from northwest to southeast. Figure 4.6 shows high magnetic intensity in the southeastern parts and low intensity in the northwestern parts of the study area.

The regional anomaly map from polynomial fitting of degree 2 (Figure 4.7) shows magnetic intensity of the area ranging from $-35\ nT\ to\ 105\ nT$. The map shows an increase of magnetic intensity in conical form from northwest to southeast. Figure 4.7 shows very high magnetic intensity in the southeastern part and very low intensity in the northwestern part of the study area. The regional anomaly maps (Figures 4.6 and 4.7) were product of WinGLink and the Surfer 11 softwares.

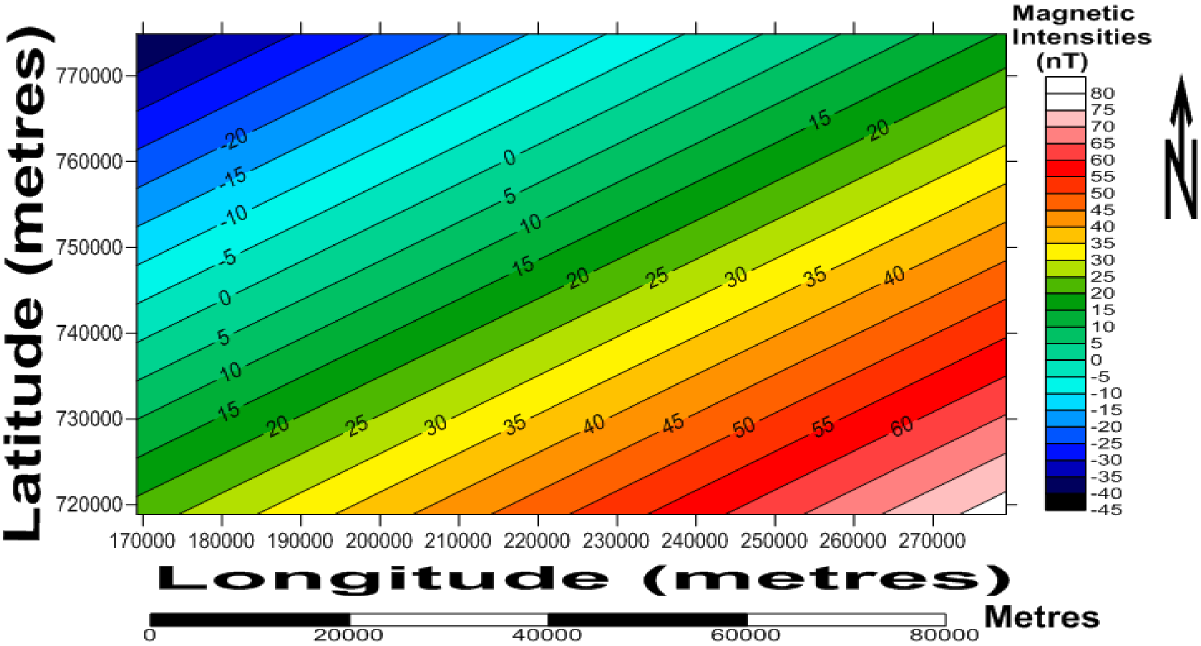

Figure 4.6: Regional anomaly map from polynomial fitting of degree 1 (contour intervals $-5\ nT$)

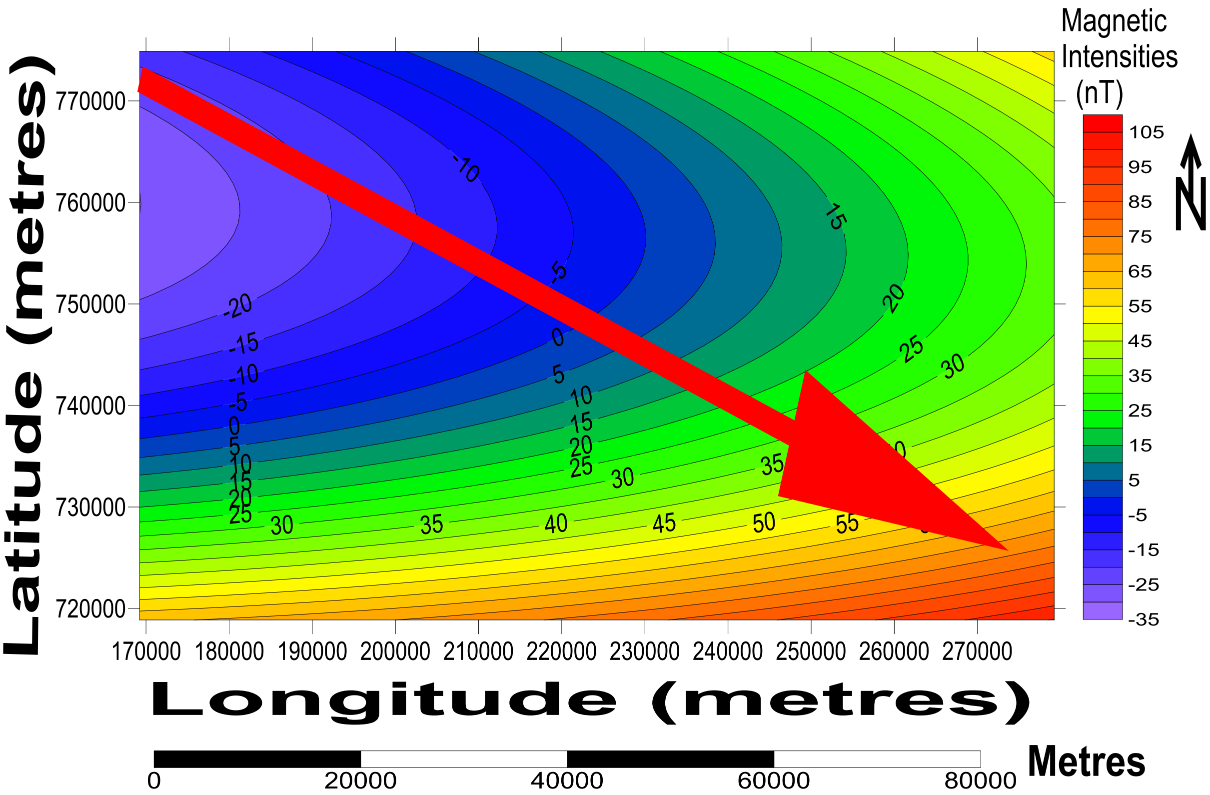

Figure 4.7: Regional anomaly map from polynomial fitting of degree 2 (contour intervals $-5\ nT$)

4.2.6 First horizontal derivative

The first horizontal derivative map (Figure 4.8) shows clearly that the area has low intensity in general as indicated by the colour legend bar. The areas G1 and G2 have high magnetic intensity compared to other areas. The magnetic intensity of the study area range from $0\ nT\ to\ 0.054\ nT$. The first horizontal derivative map was achieved by WinGLink and Surfer 11 softwares.

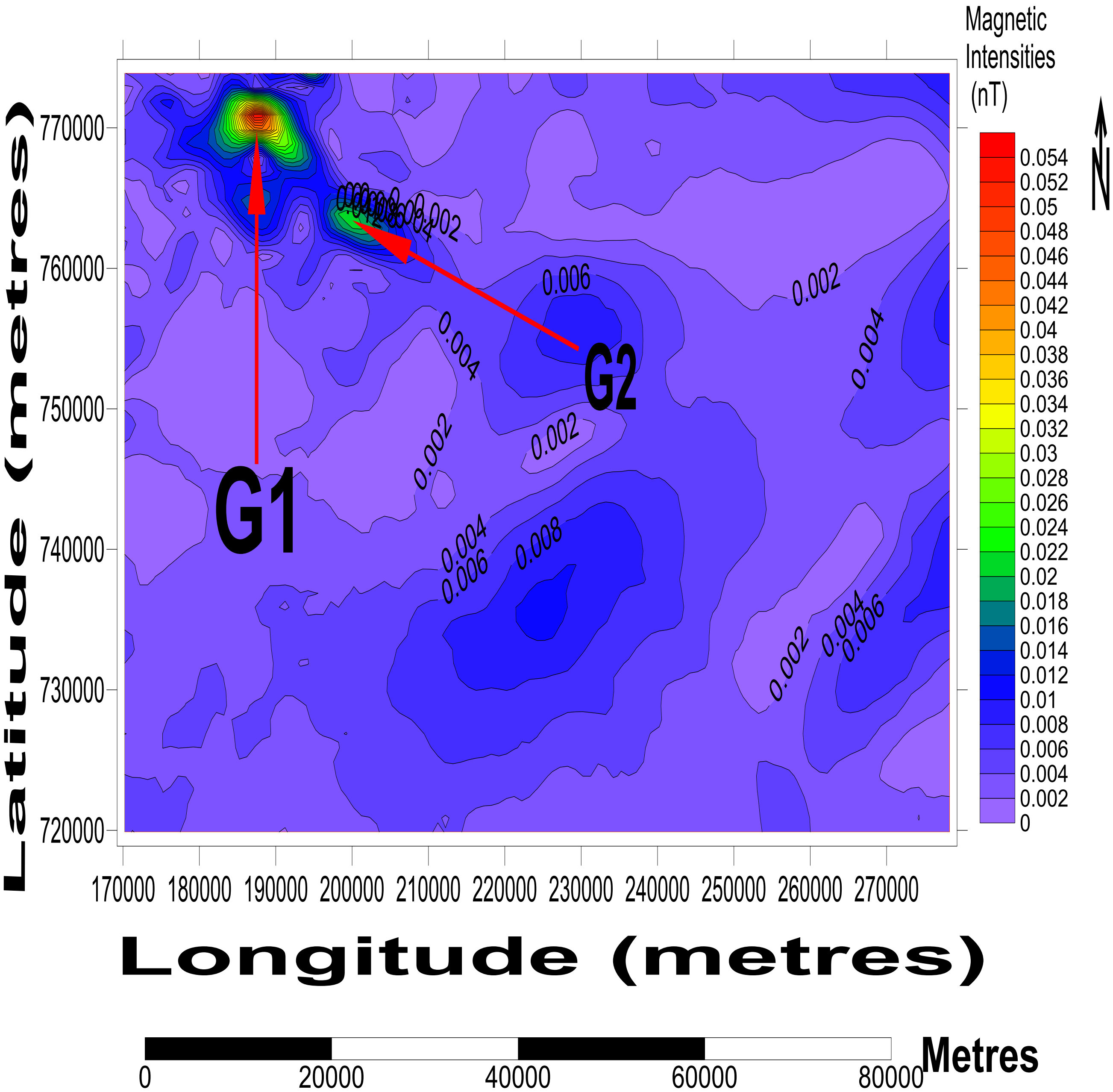

Figure 4.8: First horizontal derivative (contour intervals 0.00001 nT)

4.2.7 First vertical derivative

The first vertical derivative map (Figure 4.9) shows the magnetic intensity of the area ranging from 18.925 nT to 19.02 nT. The intensity is high at points T1 and T2 which occur in the northwestern parts of the study area. WinGLink and Surfer 11 were employed in producing the first vertical derivative map (Figures 4.9).

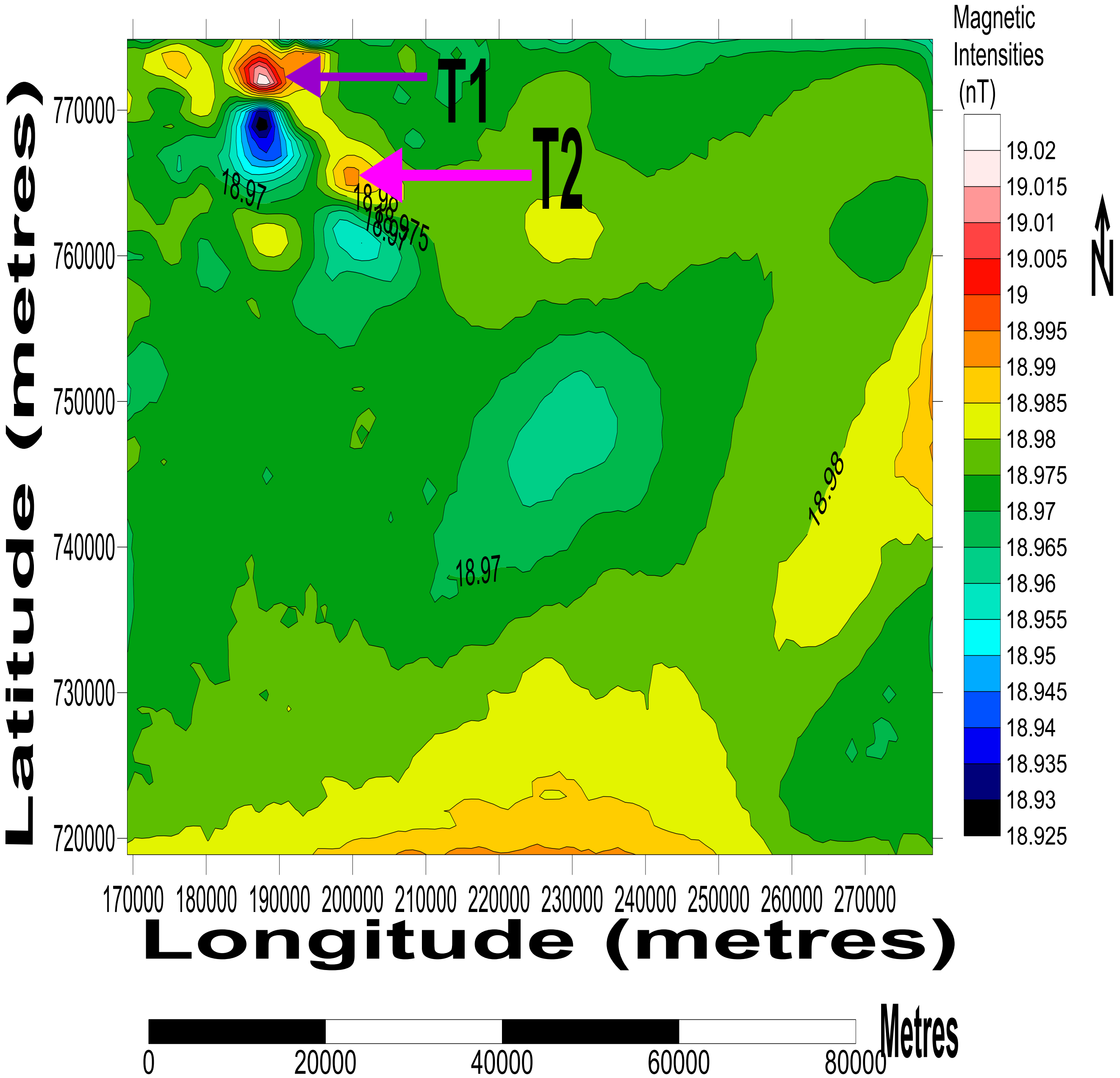

Figure 4.9: First vertical derivative (contour intervals 0.005 nT)

4.2.8 Rose diagram (circular histogram)

From Figure 4.10 the major anomaly trends are northeast (NE) and southwest (SW) directions while the minor anomaly trends are northeast of east (NE of E), southeast (SE), southeast of east (SE of E), south (S), west (W), northwest (NW) and northwest of west (NW of W) directions. The Rose diagram was achieved by the software $ROZETA^{TM}$.

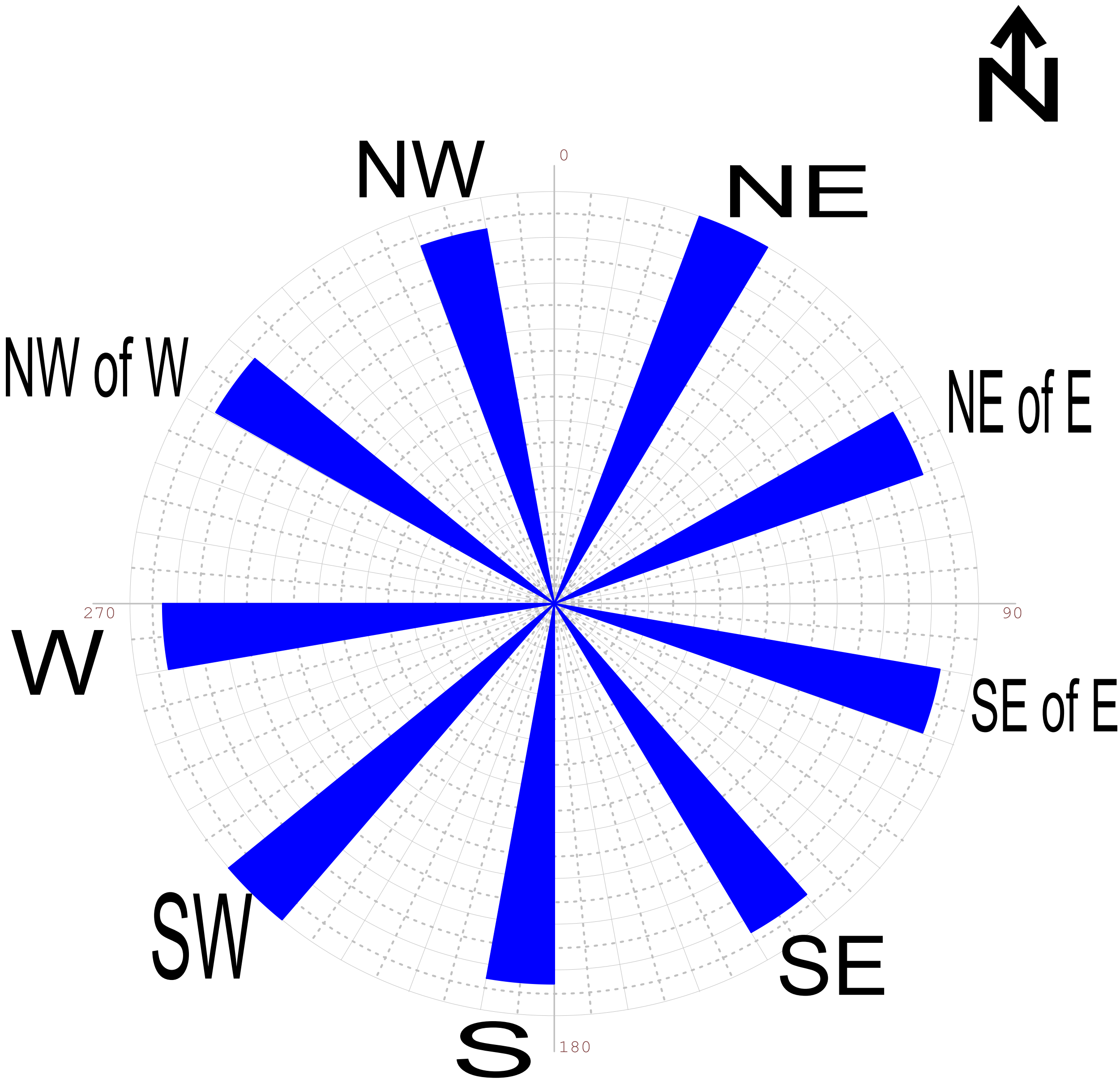

Figure 4.10: Rose diagram showing the structural lineament in Ubiaja/Illushi

4.3 Quantitative Interpretation

This involves the numerical interpretation of data in order to get the depth to basement. This involved the following methods:

(i) Source parameter imaging (SPI) method

(ii) Euler 3D deconvolution method

(iii) Spectral analysis from Microsoft Excel and

(iv) Inverse and forward modeling using potent software

4.3.1 Source parameter imaging (SPI) method

The Oasis Montaj software was used in computing the SPI image and depth. The generated SPI grid image and SPI legend (Figure 4.11) shows varied colours supposedly showing different magnetic susceptibility contrast within the study area and could portray the undulations in the basement surface. The negative values indicated in the legend signify depth. The blue colours from the legend shows areas of thicker sediments or deep lying magnetic bodies. The pink, purple, orange and yellow colours at the SPI legend shows areas of shallower sediment or near surface lying magnetic bodies. The depth of magnetic source ranges from -258.2 m to -3497.7 m.

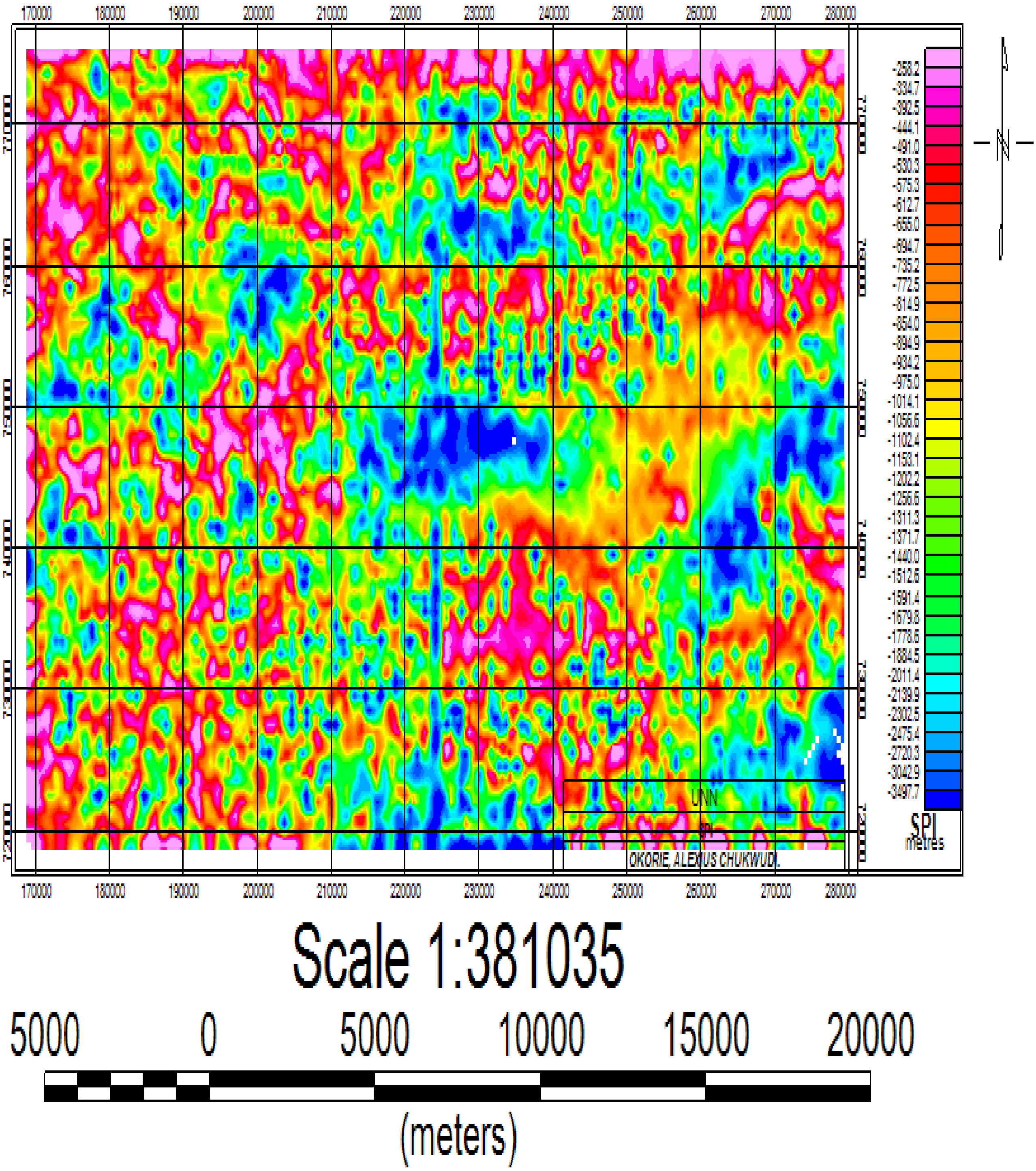

Figure 4.11: The SPI grid map showing depths to magnetic bodies

4.3.2 Standard Euler deconvolution method

In computing the Euler depth and to produce the Euler depth map and legend, standard Euler deconvolution (Euler 3-D) interpretation was carried out in three dimensions by employing

Oasis Montaj software. For four different structural indices (SI = 0.5, 1, 2 and 3), four Euler 3D maps were generated (Figures 4.12a , 4.12b, 4.12c and 4.12d). From the maps, the blue colour indicates deep lying magnetic bodies, while the pink colour indicates the shallow magnetic bodies. The outcrops as shown by the positive depth values in the colour legend bar signify that some parts of the study area are mountainous or rocky, while the negative depth values are depths of deep lying magnetic source bodies. There is no Euler solution (depth) for the particular structural index used as indicated by the areas in the maps without magnetic signatures or colour (depth).

The Euler 3D depth grid for structural indices (SI) 0.5, 1, 2 and 3 are shown in Figures 4.12a, 4.12b, 4.12c and 4.12d respectively. Depth range for SI = 0.5 is from $+1377.3$ m to -2510.9 m; for SI = 1, depths range from $+1482.0$ m to -3003.3 m; for SI = 2, depths range from $+1627.8$ m to -2984.3 m; and for SI = 3, depths range from $+1853.9$ m to -3089.9 m.

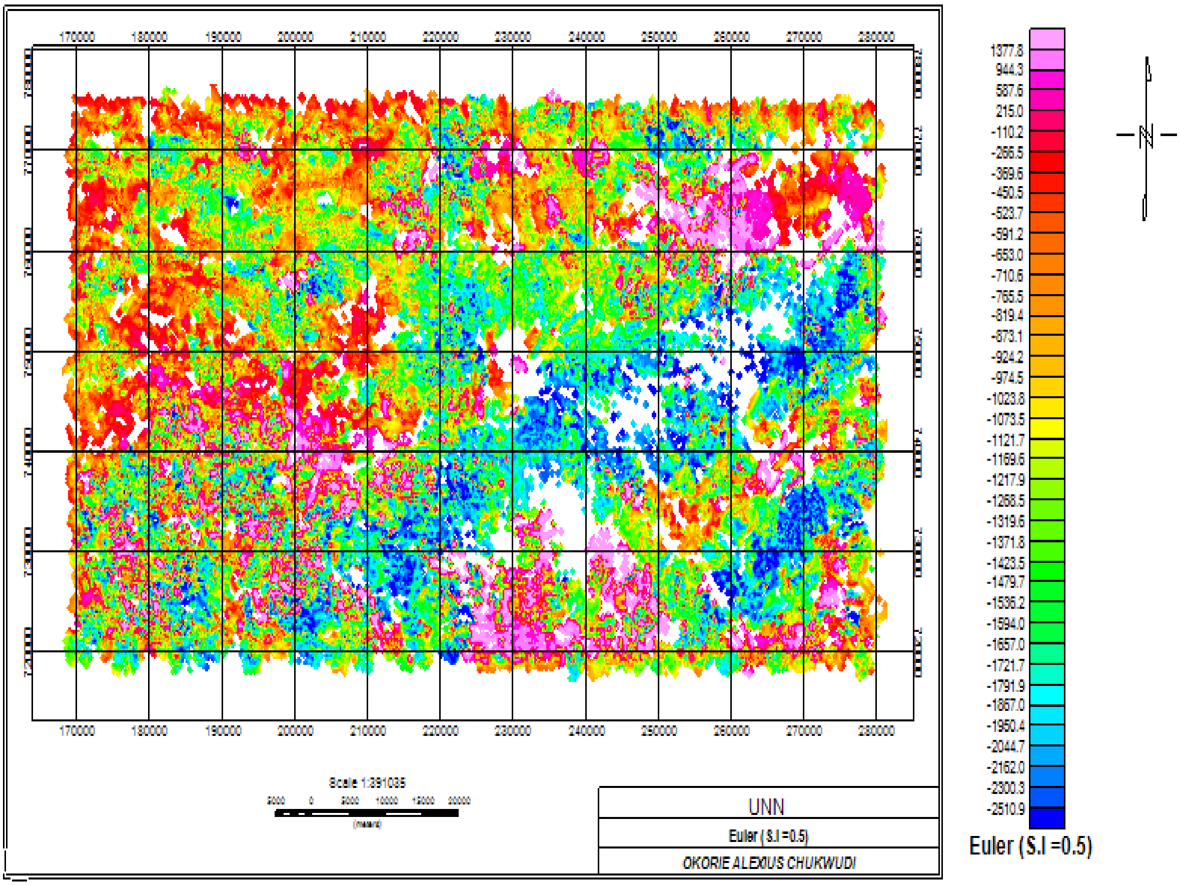

Figure 4.12a: Euler grid map (structural index equals 0.5)

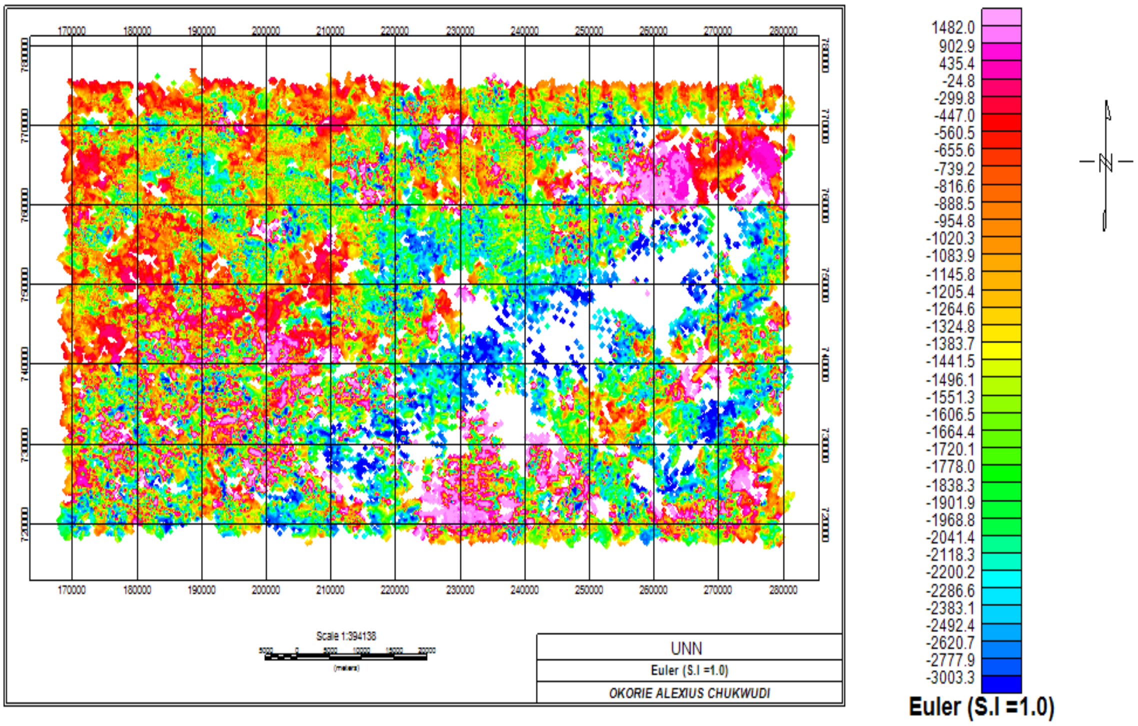

Figure 4.12*b*: Euler grid map (structural index equals 1)

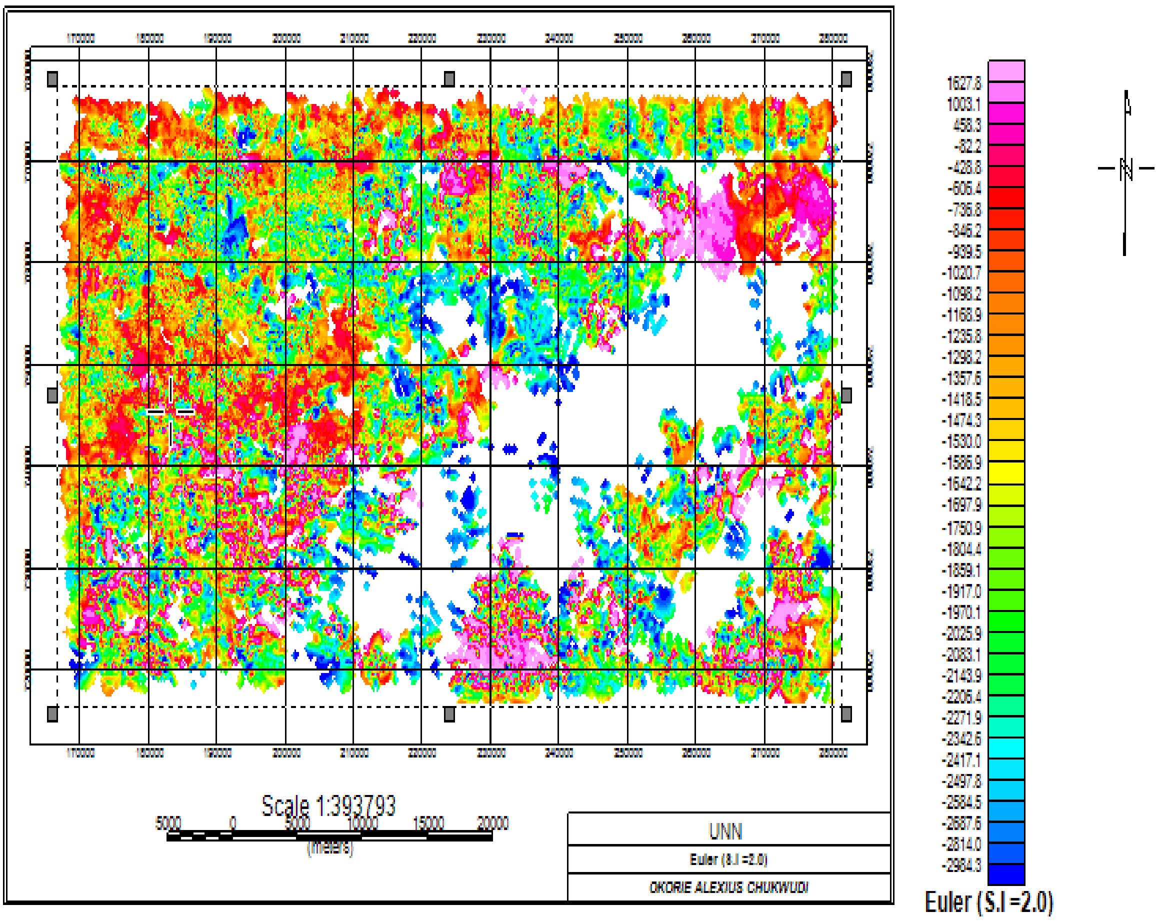

Figure 4.12*c*: Euler grid map (structural index equals 2)

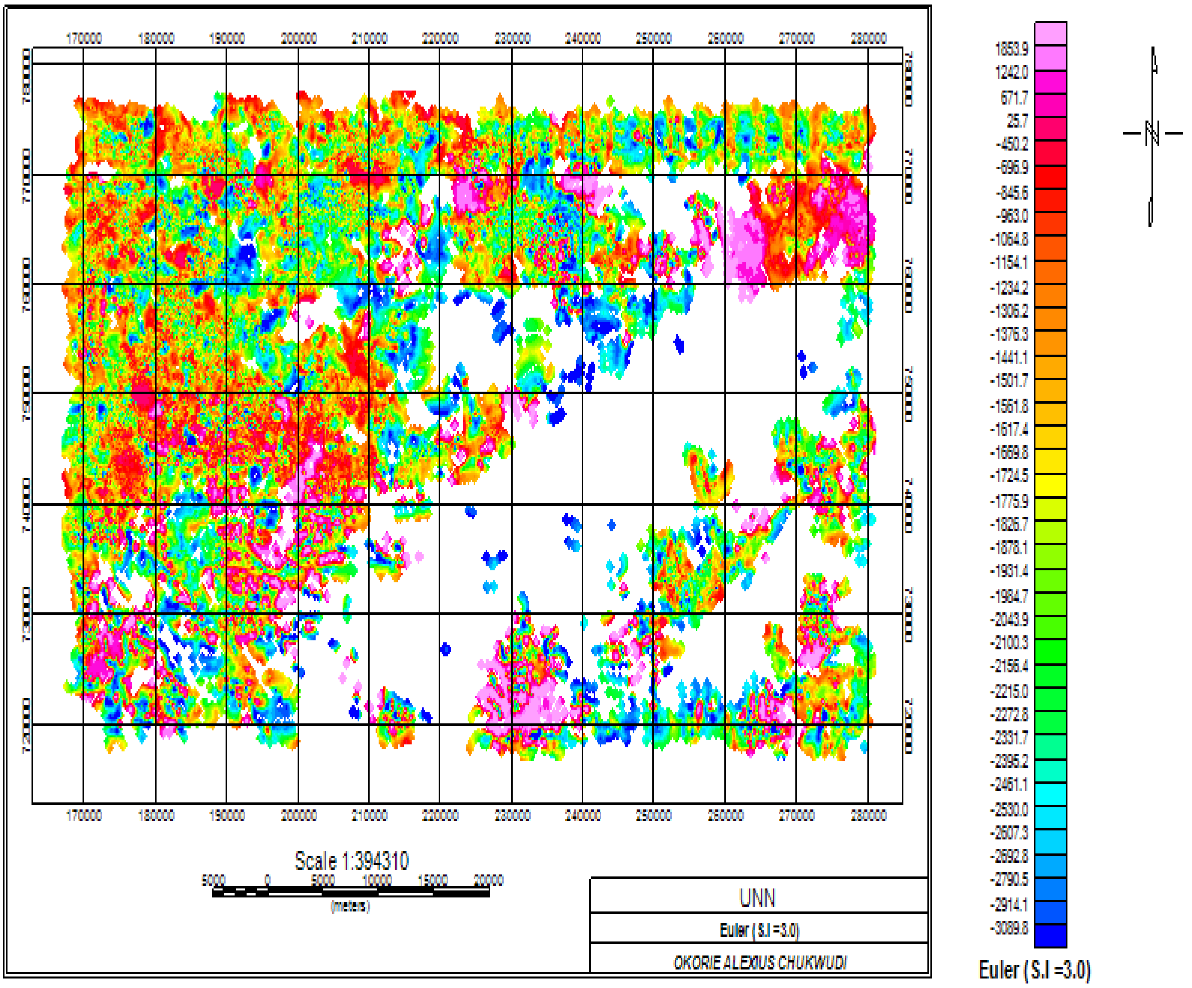

Figure 4.12d: Euler grid map (structural index equals 3)

4.3.3 Spectral analysis result

The study area was divided into 18 spectral cells to allow for an in-depth analysis of the area as shown in Figure 4.13. The area covered by one spectral cell measured 18.33 km by 18.33 km. In carrying out the cell division, special care was taken to avoid two spectral cells from having the same depth value (if spectral cell is very small) or not having an in-depth spectral depth analysis (if spectral cell is very large). Letters A, B, C, D, E, F, G, H, I, J, K, L, M, N, O, P, Q and R were used to denote the 18 spectral cell (Figure 4.13).

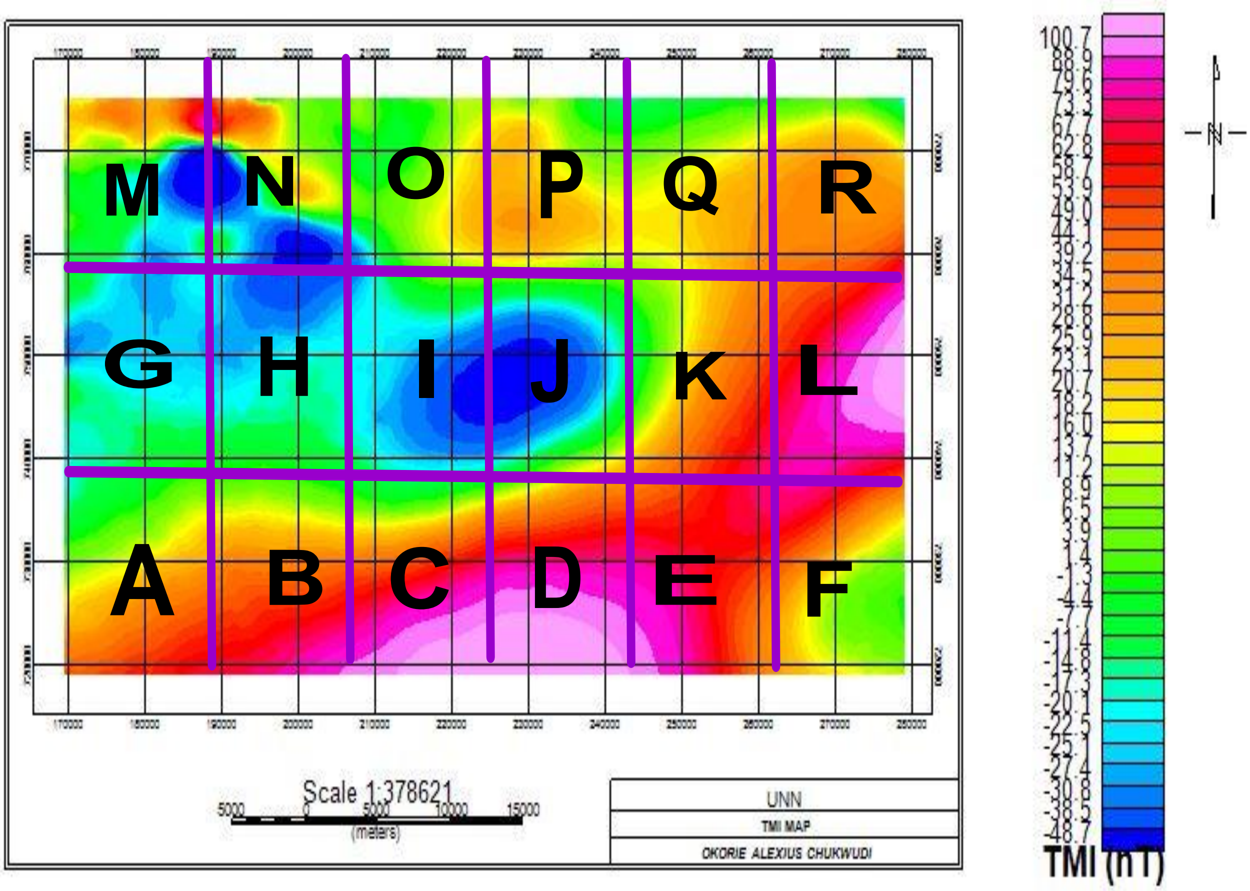

Figure 4.13: The TMI map of the study area showing the spectral cells

4.3.3.1 Plots of spectral depths (Logarithm of Energy against frequency)

The natural logarithm of the energy against the frequency was obtained following the steps in Figure 3.4. The slope of the spectral graph equals $\frac{\log \Delta E}{\Delta f}$ which when equated to equation 3.20 gives the sedimentary thickness (Z) for both the shallow source magnetic bodies and the deeper source magnetic bodies.

The red tangent was used in calculating the deeper depths, while the blue tangent was used in calculating the shallow depths as shown in Figures 4.14a to 4.14r. From the Figures (4.14a to 4.14r) and values obtained, Figure 4.14p has the highest depth of 3978.874 m, while Figure 4.14h has the shallowest depth of 163.836 m. The summary of the spectral depths for the eighteen (18) spectral blocks is given in Table 4.1.

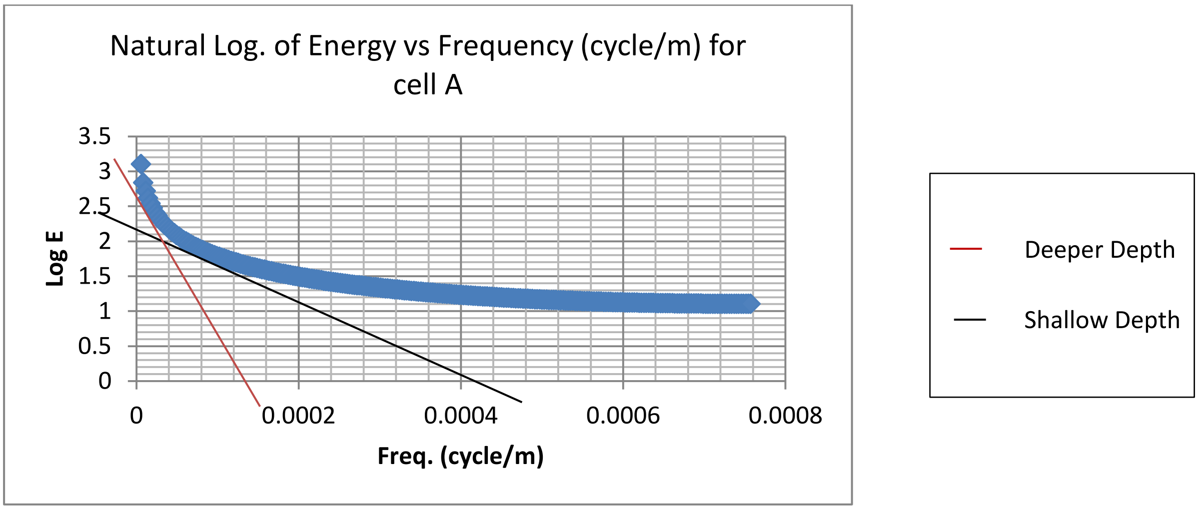

Figure 4.14*a*: A graph showing the deeper depth and the shallow depth for cell A

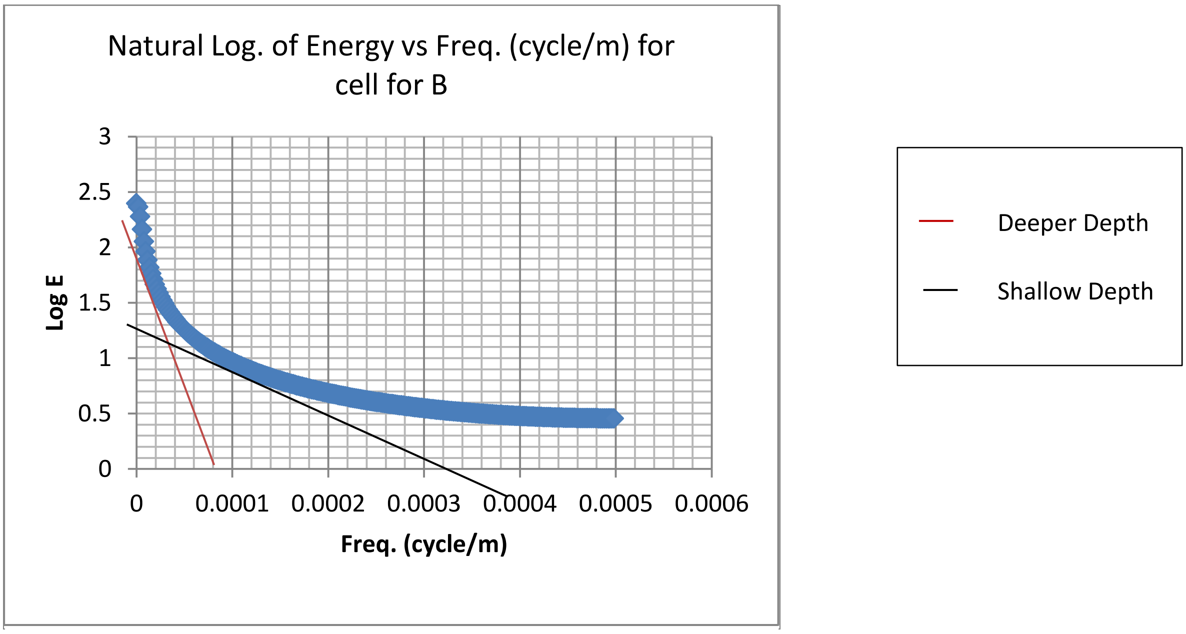

Figure 4.14*b*: A graph showing the deeper depth and the shallow depth for cell B

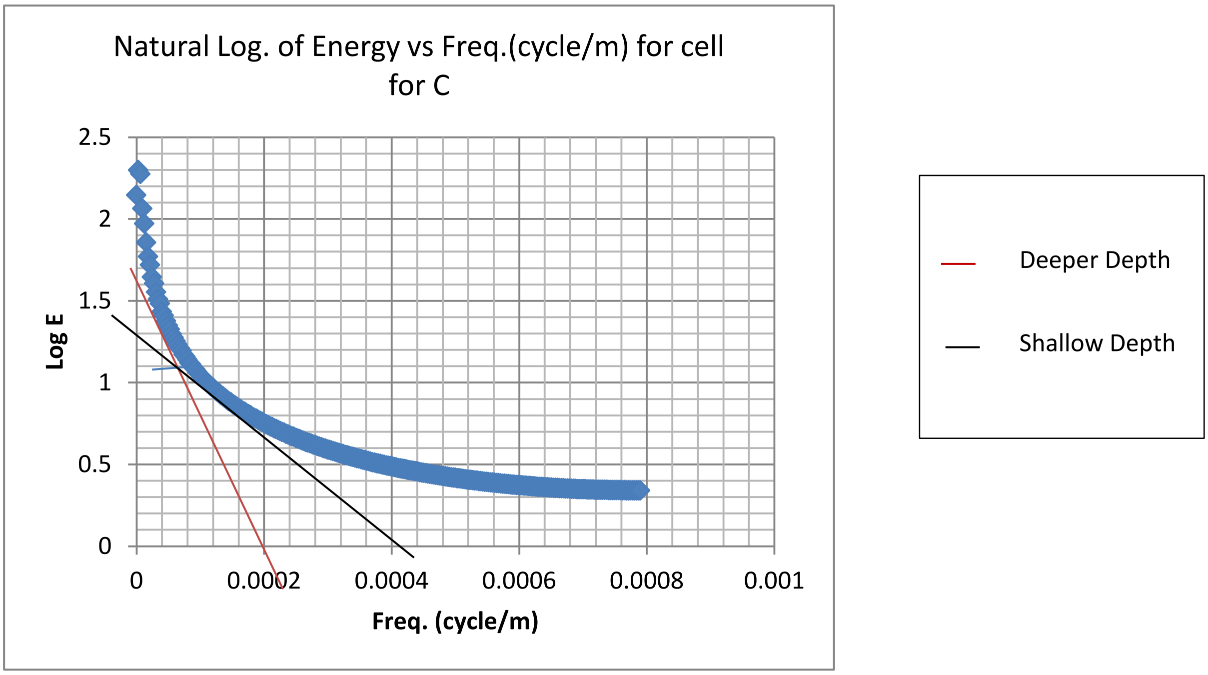

Figure 4.14*c*: A graph showing the deeper depth and the shallow depth for cell C

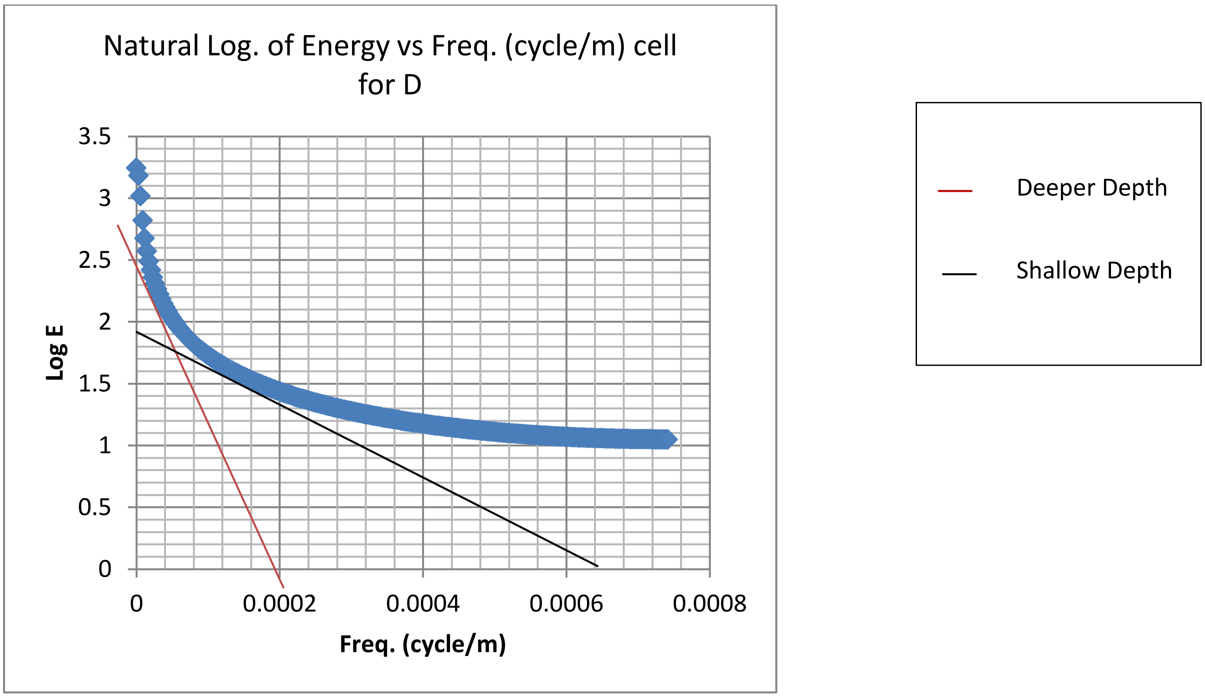

Figure 4.14*d*: A graph showing the deeper depth and the shallow depth for cell D

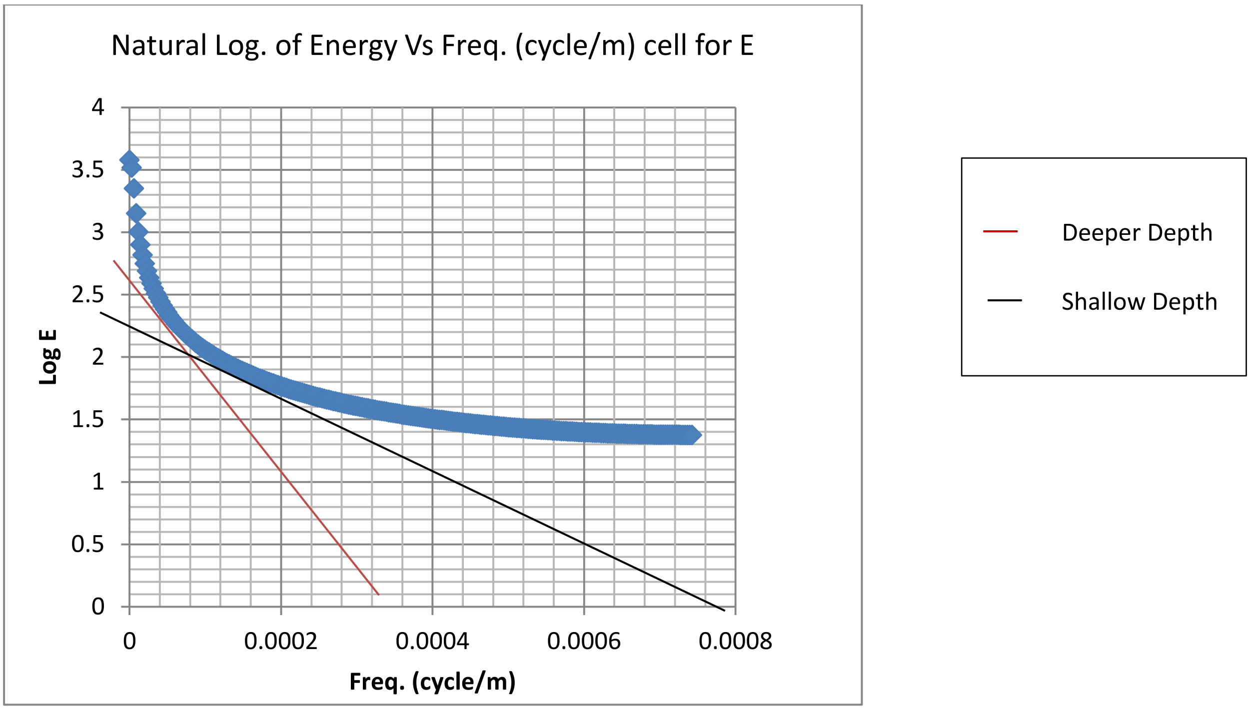

Figure 4.14*e*: A graph showing the deeper depth and the shallow depth for cell E

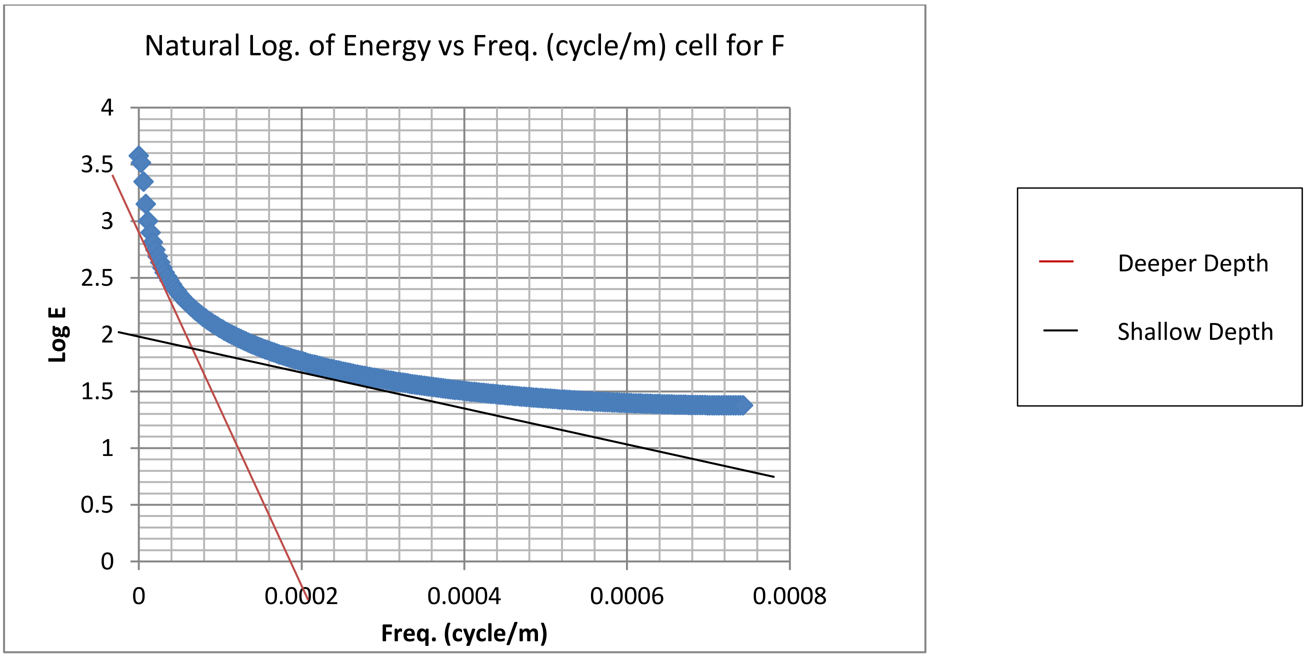

Figure 4.14*f*: A graph showing the deeper and the shallow depth for cell F

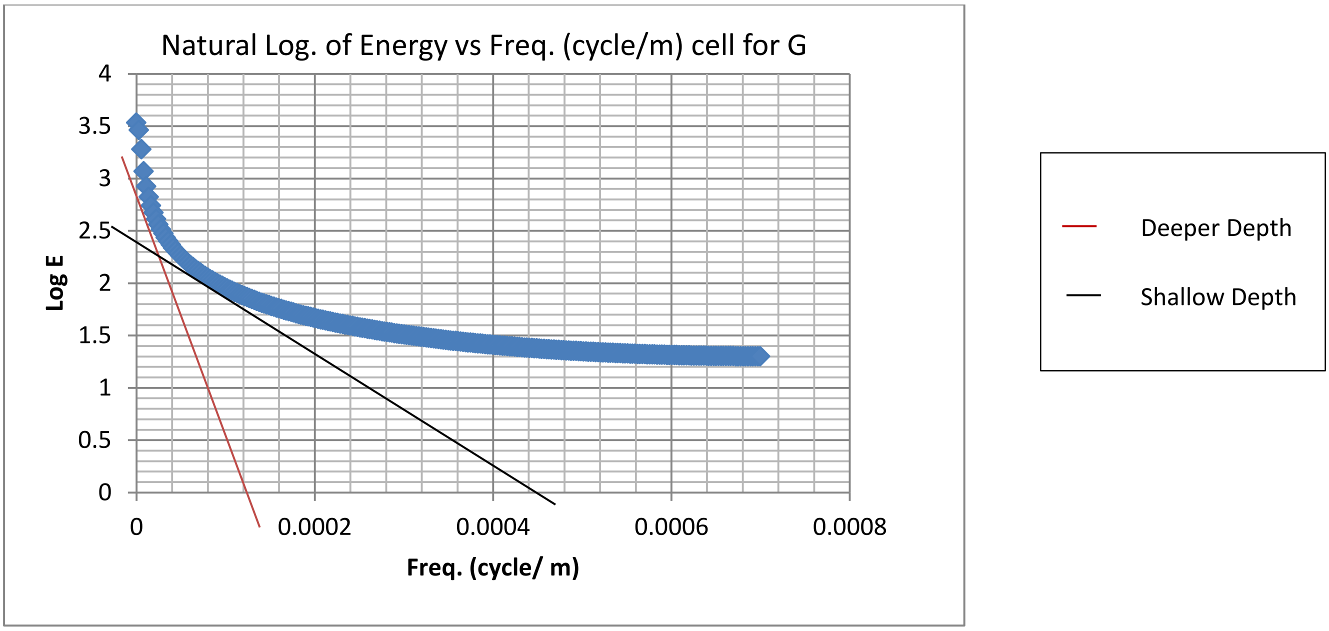

Figure 4.14*g*: A graph showing the deeper and the shallow depths for cell G

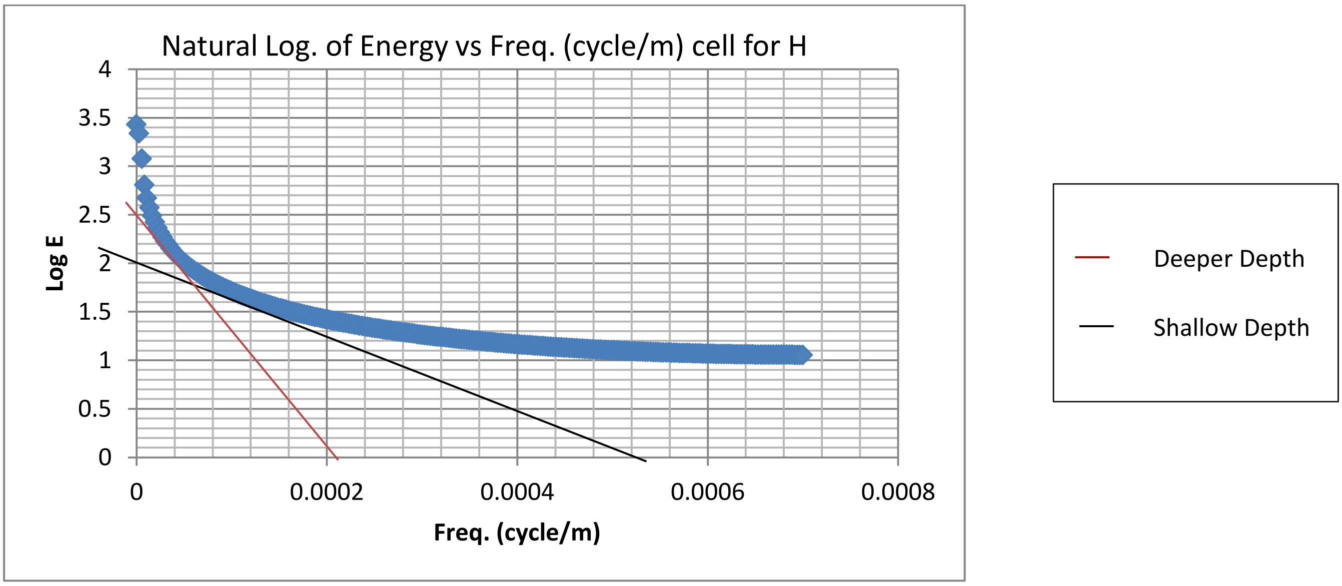

Figure 4.14*h*: A graph showing the deeper and the shallow depths for cell H

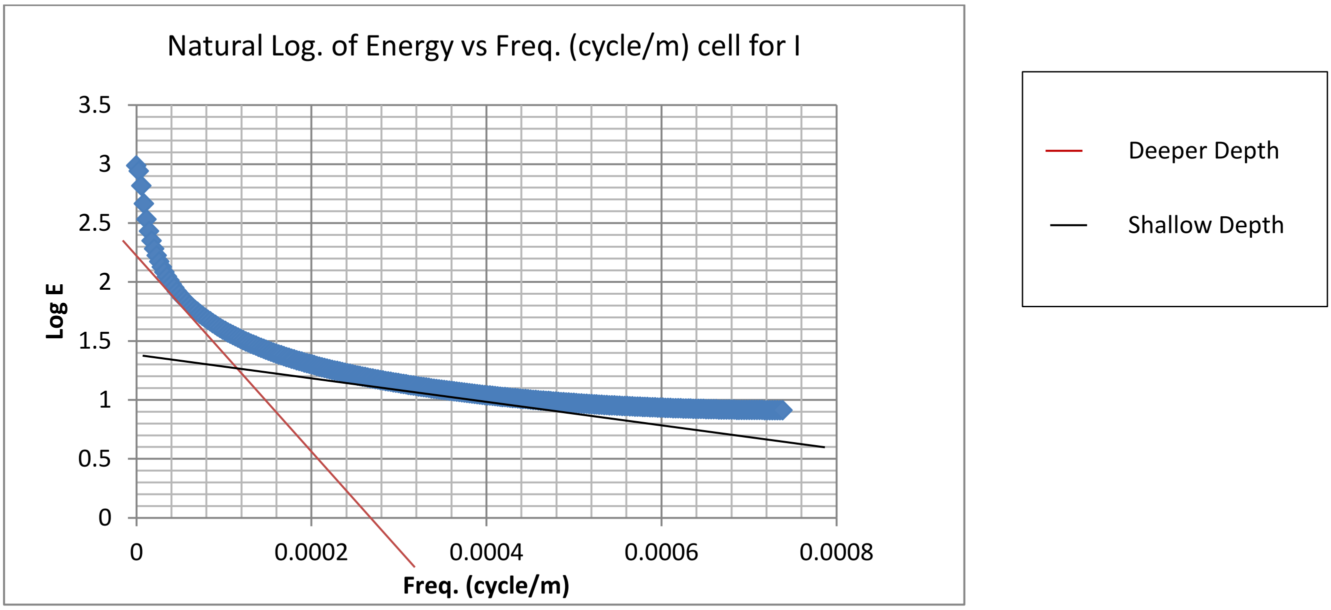

Figure 4.14*i*: A graph showing the deeper and the shallow depths for cell I

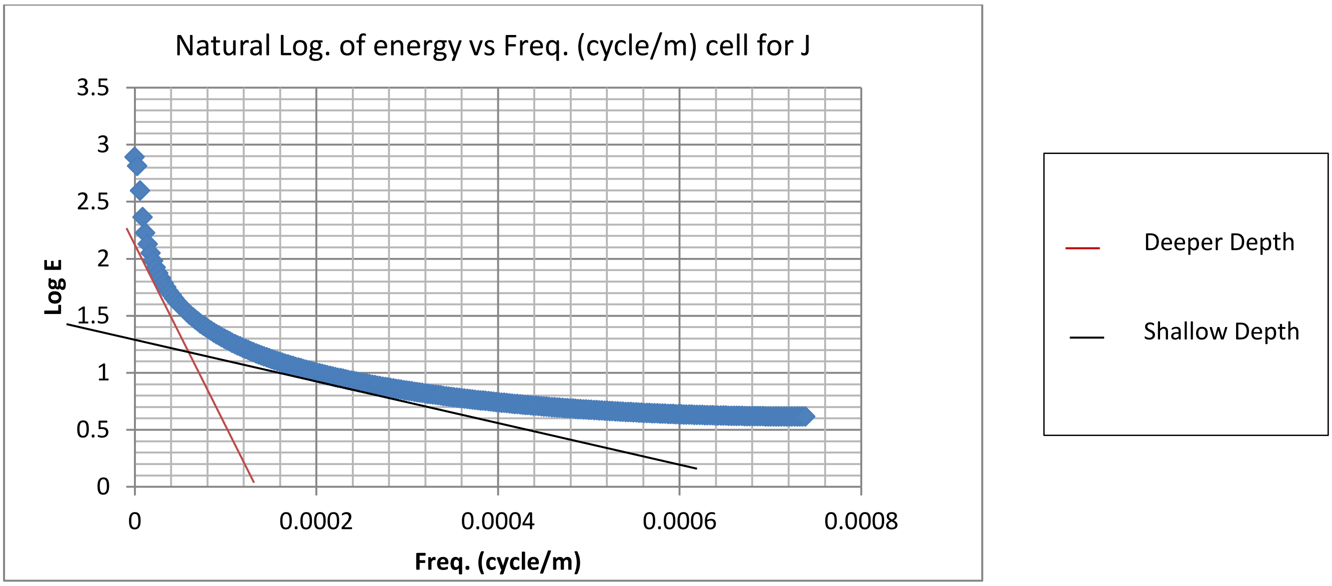

Figure 4.14*j*: A graph showing the deeper and the shallow depths for cell J

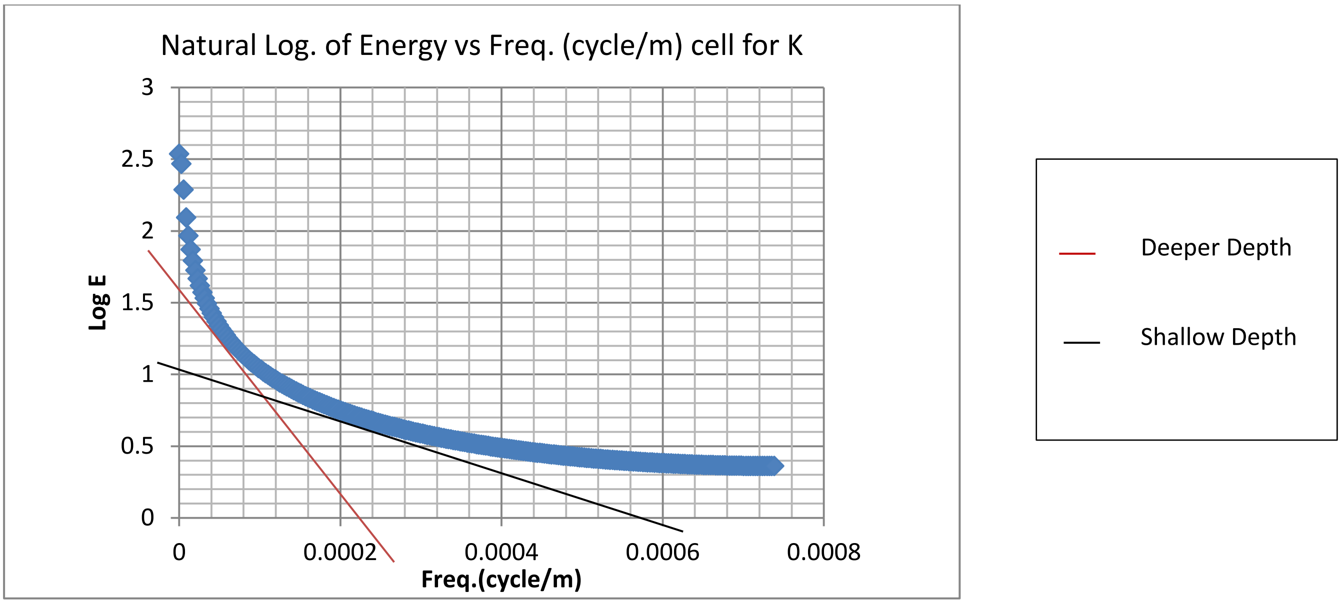

Figure 4.14*k*: A graph showing the deeper and the shallow depths for cell K

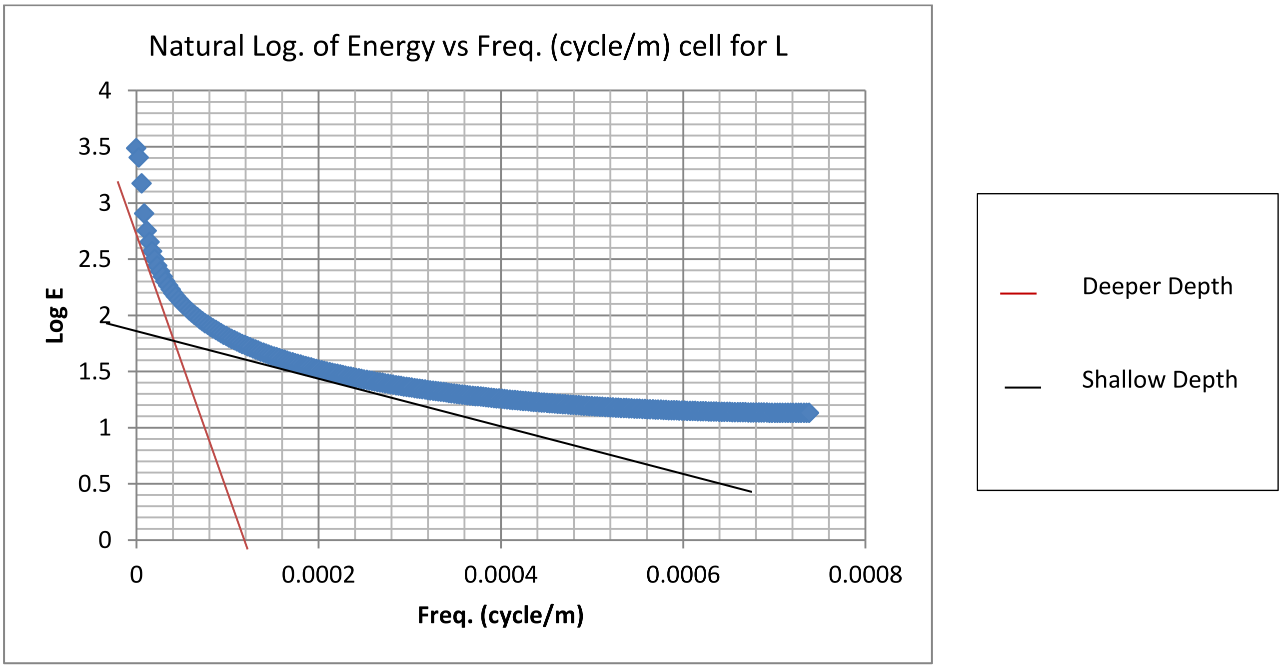

Figure 4.14*l*: A graph showing the deeper and the shallow depths for cell L

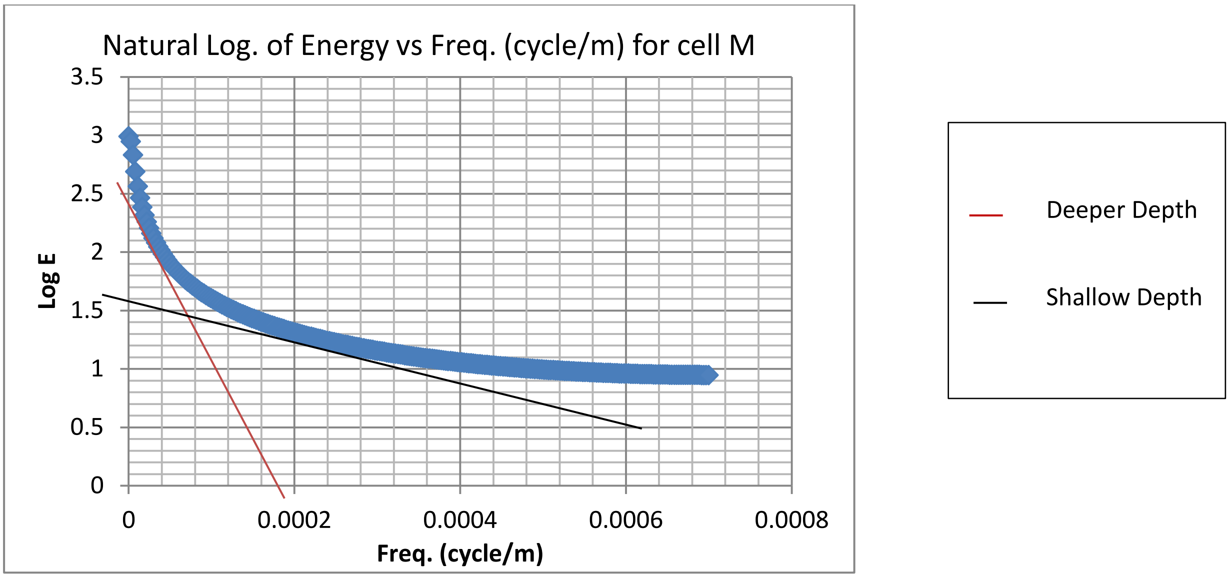

Figure 4.14*m*: A graph showing the deeper and the shallow depths for cell M

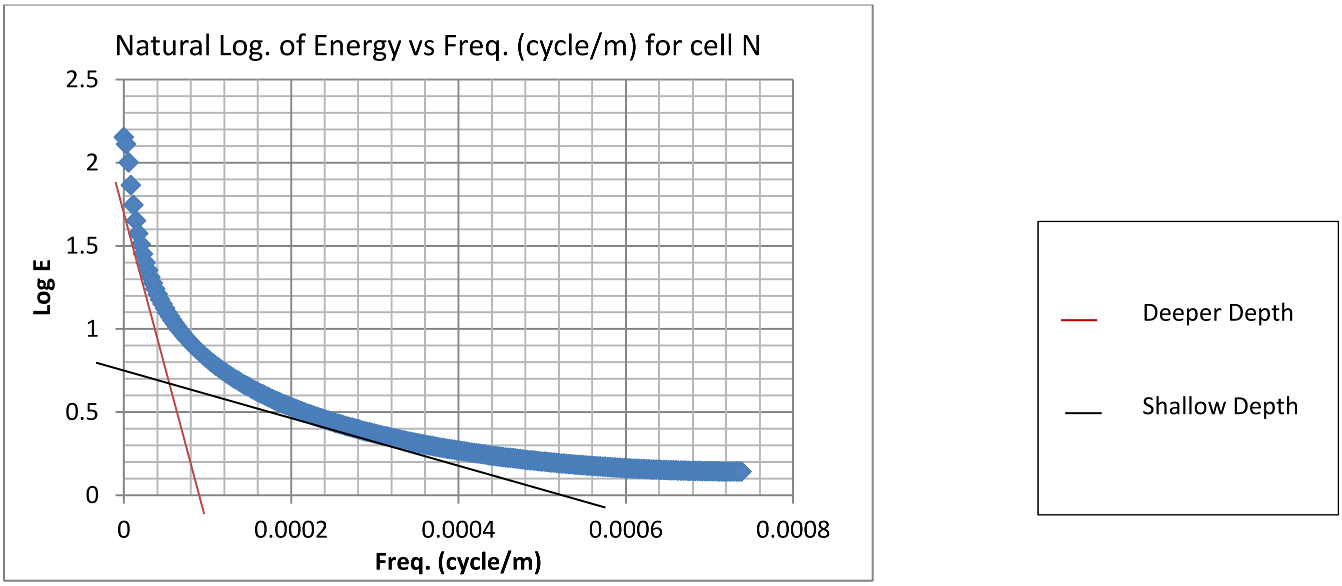

Figure 4.14*n*: A graph showing the deeper and the shallow depths for cell N

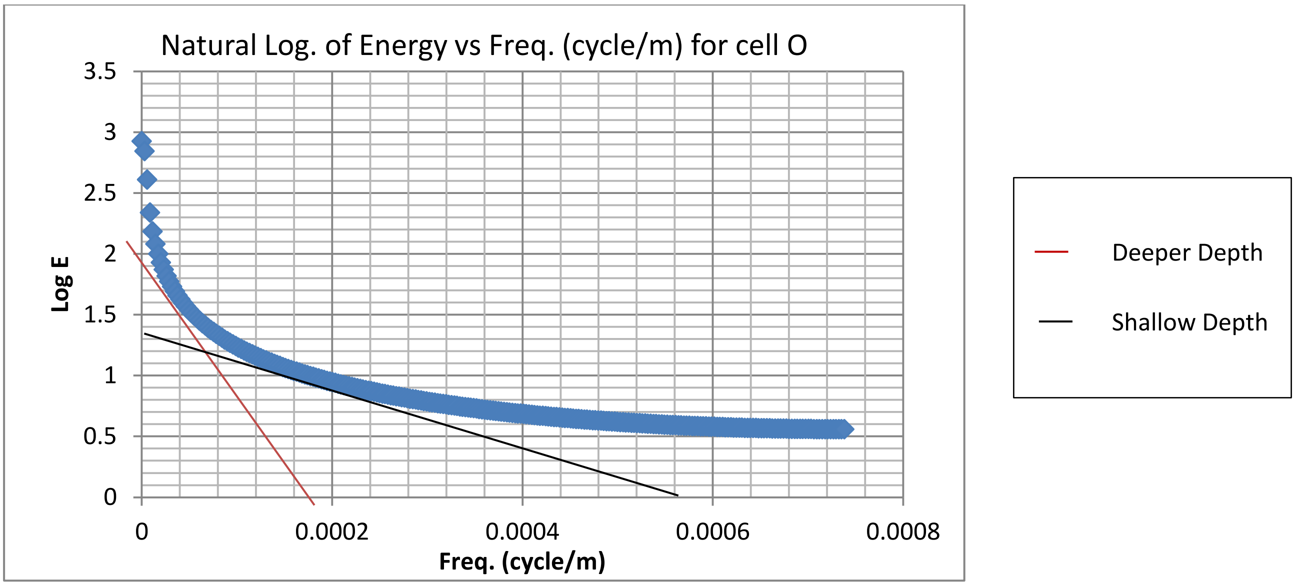

Figure 4.14*o*: A graph showing the deeper and the shallow depths for cell O

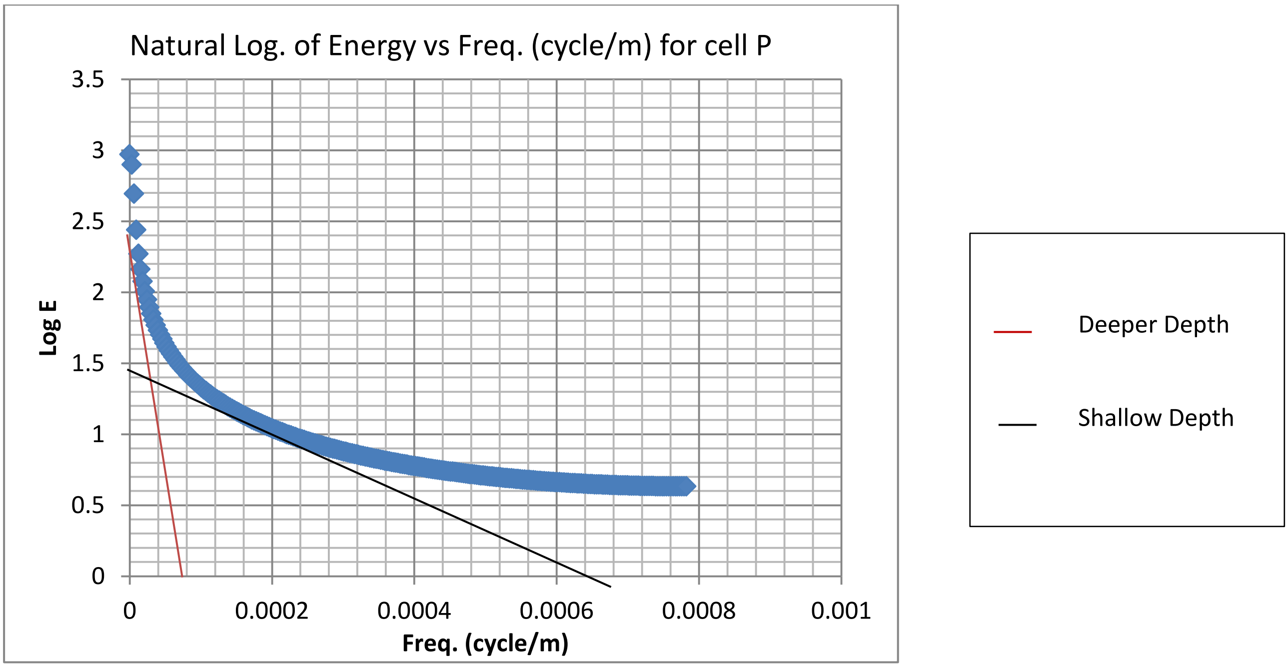

Figure 4.14*p*: A graph showing the deeper and the shallow depths for cell P

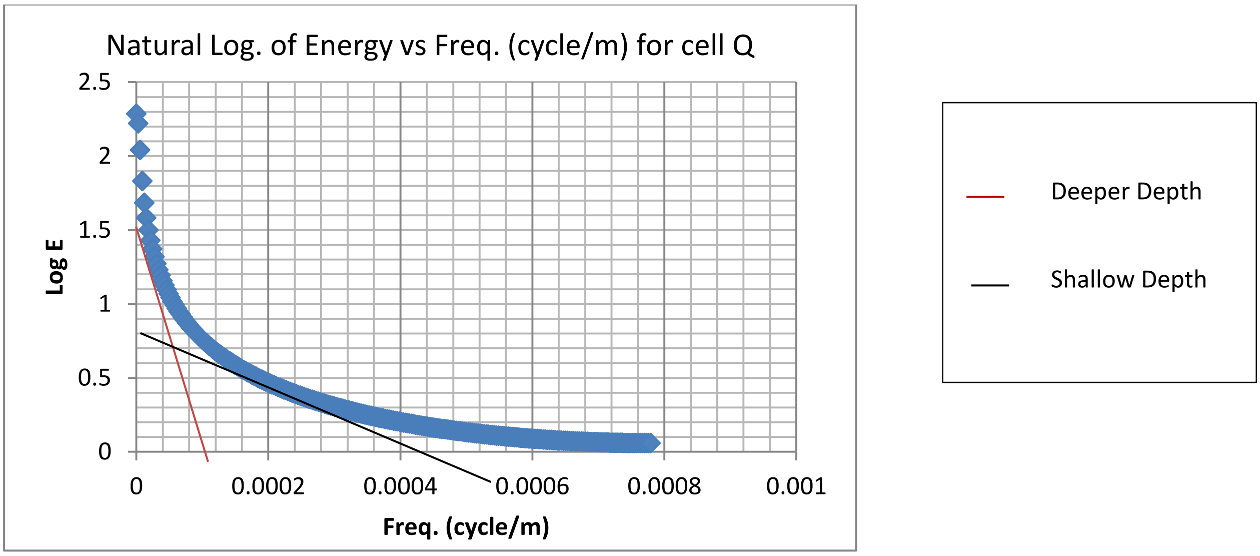

Figure 4.14*q*: A graph showing the deeper and the shallow depths for cell Q

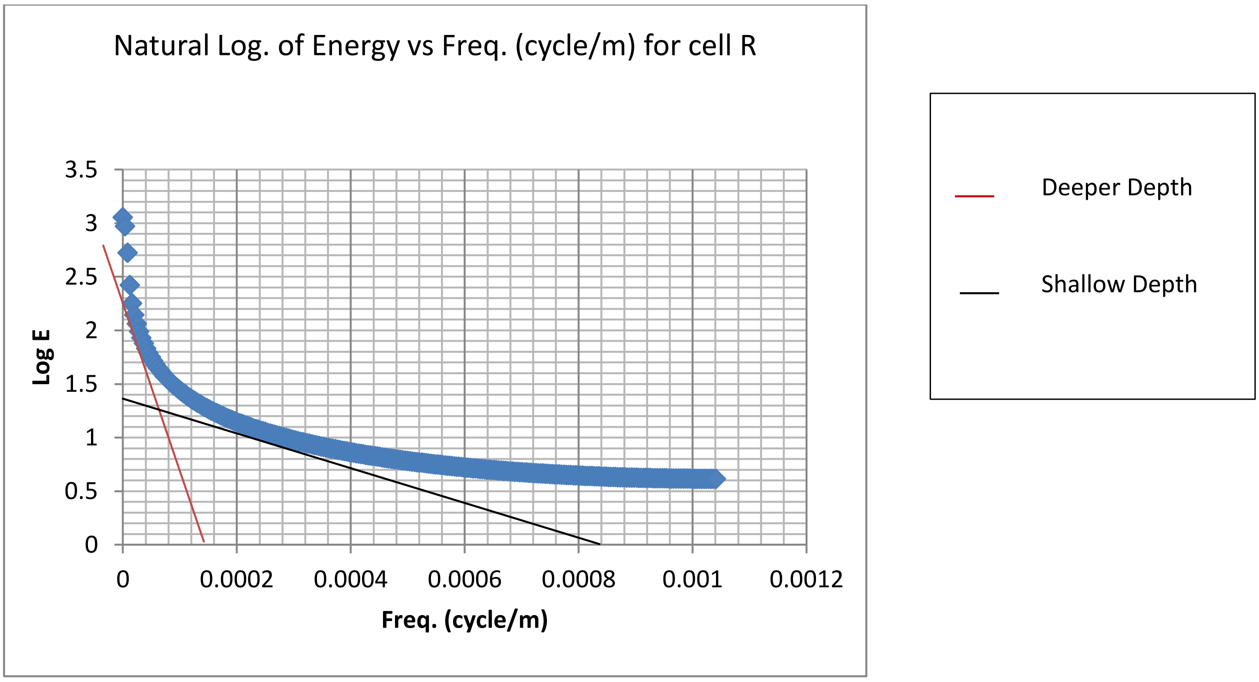

Figure 4.14*r*: The graphs showing the deep and the shallow depths for cell R

Table 4.1: spectral depths for the eighteen (18) blocks

SPECTRAL CELL	CENTRE VALUES (DEGRESS)		DEEPER SOURCE DEPTH (METRES)	SHALLOW SOURCE DEPTH (METRES)
	LONGITUDE (X)	LATITUDE (Y)		
A	6.083	6.583	1894.702	378.940
B	6.250	6.583	2081.257	416.834
C	6.417	6.583	1503.129	298.416
D	6.583	6.583	2586.268	290.764
E	6.750	6.583	2025.608	234.051
F	6.917	6.583	2685.740	703.955
G	6.083	6.750	1407.909	460.057
H	6.250	6.750	1114.085	163.836
I	6.417	6.750	1989.437	198.944
J	6.583	6.750	2387.324	306.067
K	6.750	6.750	2586.268	312.626
L	6.917	6.750	2652.582	209.414
M	6.083	6.917	1663.893	187.241
N	6.250	6.917	2546.479	229.550
O	6.417	6.917	1338.348	298.416
P	**6.583**	**6.917**	**3978.874**	**265.258**
Q	6.750	6.917	1856.808	183.640
R	6.917	6.917	1591.549	184.733
TOTAL DEPTHS (METRES)			37890.26	5322.742
AVERAGE DEPTHS (METRES)			2105.014	295.708

4.3.3.2 2-dimensional (2D) and 3-dimensional (3D) plots of the deeper depths

Surfer 11 software was used in producing the contour 2D map and the 3D surface plots of the deeper depths. The grid map of the deeper depths (Figure 4.15) shows clearly that point P is the deepest point as indicated by the colour legend bar. The 3D depth to basement view (Figure 4.16) shows also that the point P is the deepest point as indicated by the colour legend bar. The deepest point P is found in latitude $6.917°N$ and longitude $6.583°E$ of the study area and the depth is 3978.874 m.

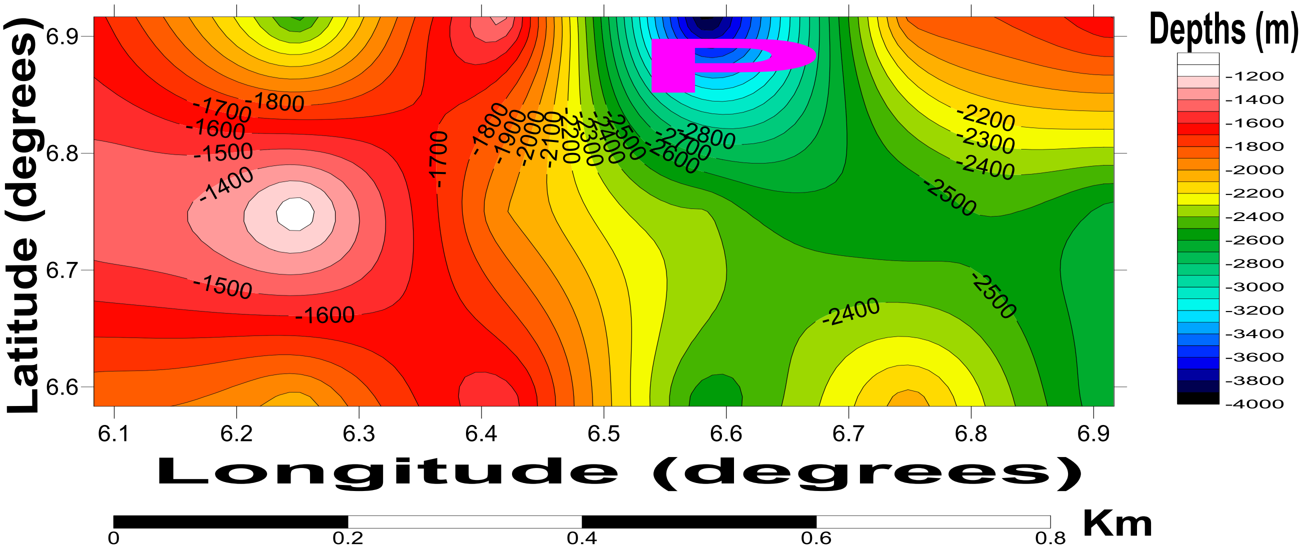

Figure 4.15: A grid map of deeper depths (2D representation)

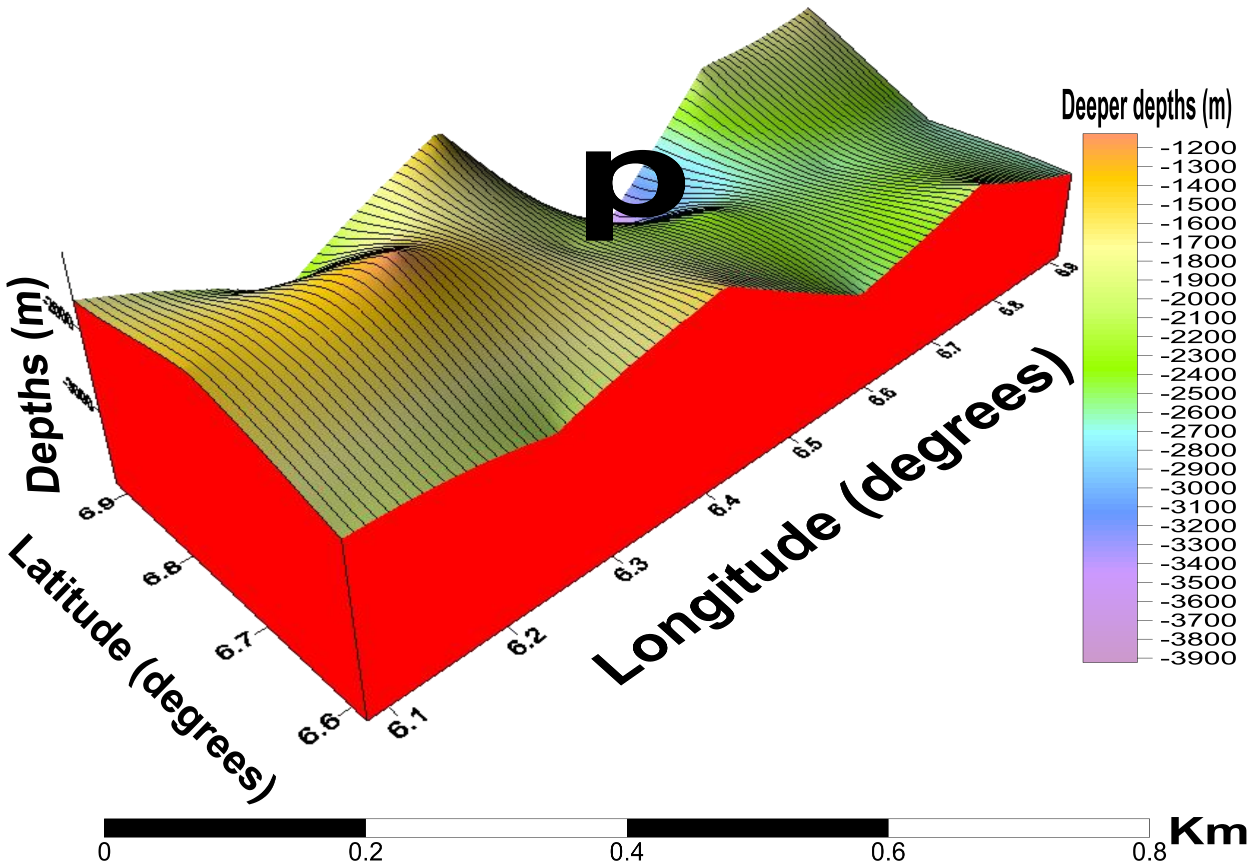

Figure 4.16: A diagram showing the 3D view of the deeper depth (depth to basement or sedimentary thickness) of the area

4.3.3.3 2-dimensional (2D) and 3-dimensional (3D) plots of the shallow depths

The contour 2D map and the 3D surface plots of the shallow depths were produced using Surfer 11 software. The contour map of the shallow depth (Figure 4.17) shows clearly that the area is very shallow except for the area in purple as indicated by the colour legend bar at depths $-560\ m$ to $-720\ m$. The 3D surface plot (Figure 4.18) clearly shows that the area is generally flat except the point indicated by the black colour from the colour legend bar (Figure 4.18).

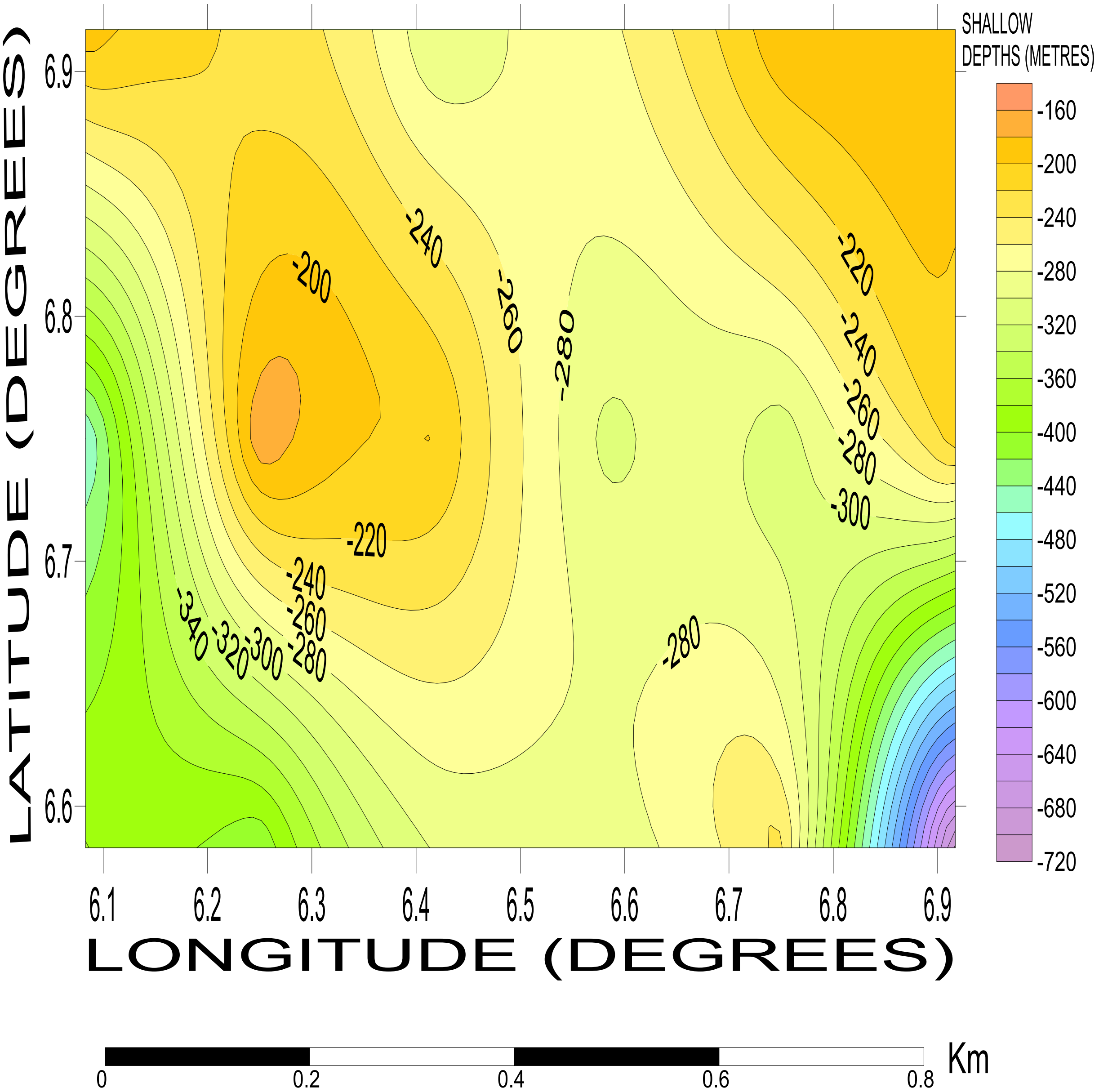

Figure 4.17: A diagram showing the 3D view of the shallow depth

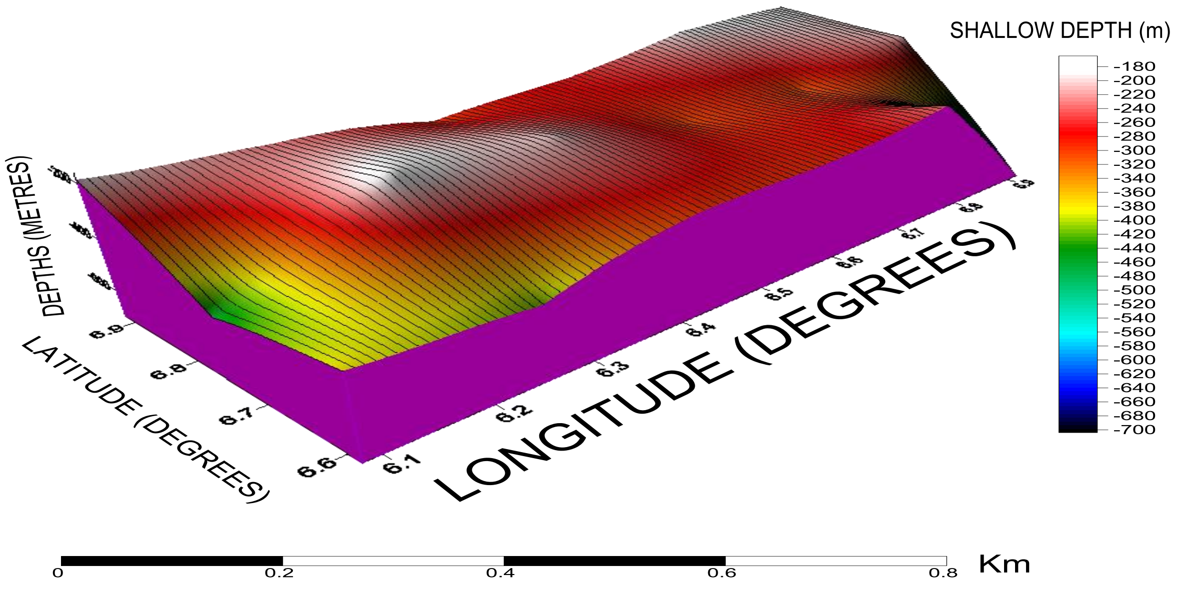

Figure 4.18: A diagram showing the 3D view of the shallow depth of the area

4.3.4 Forward and Inverse Modeling (using Potent software)

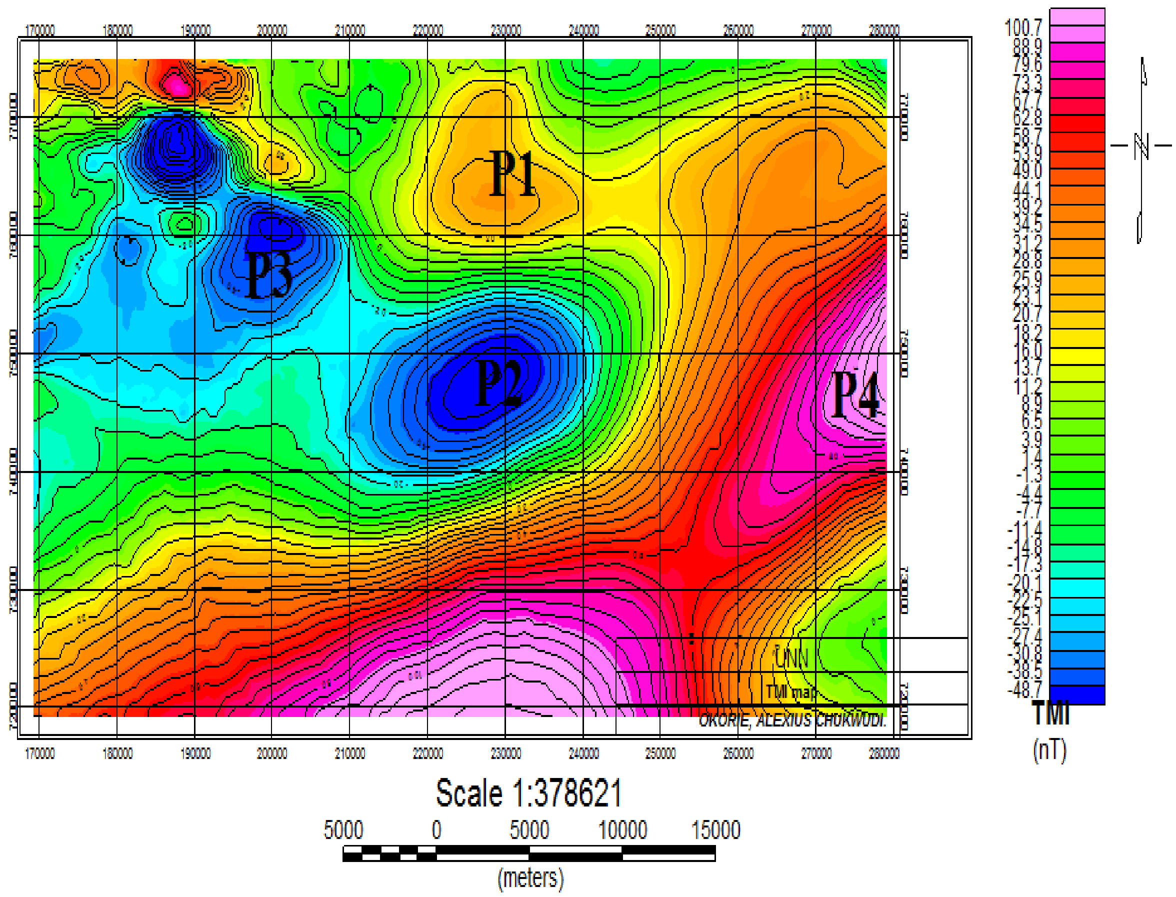

Figure 4.19: TMI contoured grid showing four profiles

To model the area and find the possible minerals and rocks in the area, four profiles (P1, P2, P3 and P4) were taken at different parts of Figure 4.19. From the results (Figures 4.20a, 4.20b, 4.20c and 4.20d, the blue curves represent the observed field while the red curves represent the calculated fields due to the model. Profiles modeled are chosen if they have good fit and also based on the geology of the area been considered. Profiles P1 and P2 were modeled using ellipsoid and sphere respectively and their susceptibility values are both 0.0100 which suggest that the possible bodies causing the anomalies are hematite, gneiss, granite or gabbro (Table 3.1). Profile P3 was modeled using ellipsoid and the susceptibility value is 0.0613 which suggest that the possible body causing the anomaly is porphyry, a hard igneous rock made up of feldspar, (Table 3.1). The profile P4 was modeled using ellipsoid and the susceptibility is 0.0288 which suggest that the possible bodies causing the anomaly are slate and hematite (Table 3.1). The summary of the modeling results is shown in Table 4.2.

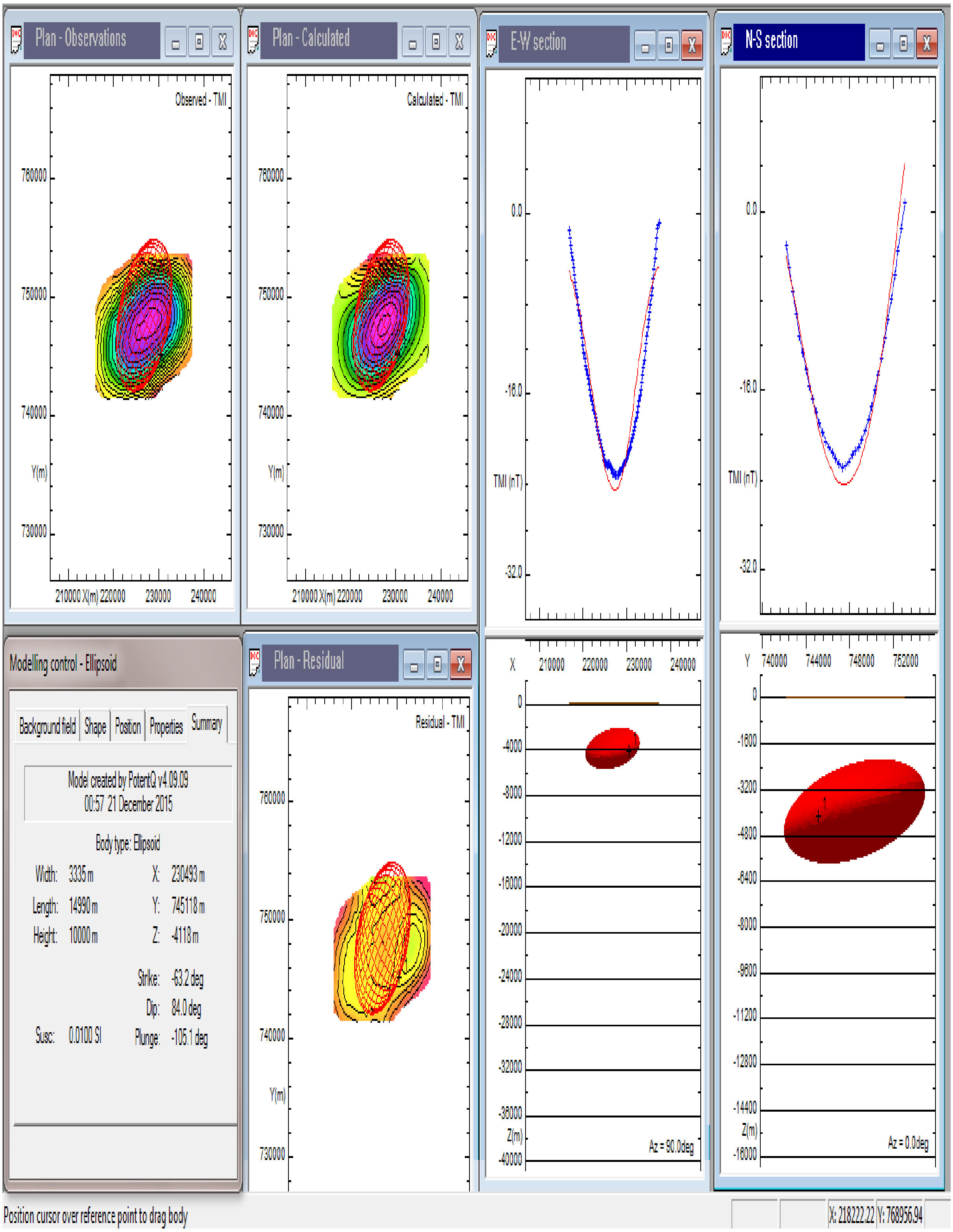

Figure 4.20a: forward and inverse modeling of profile $P1$

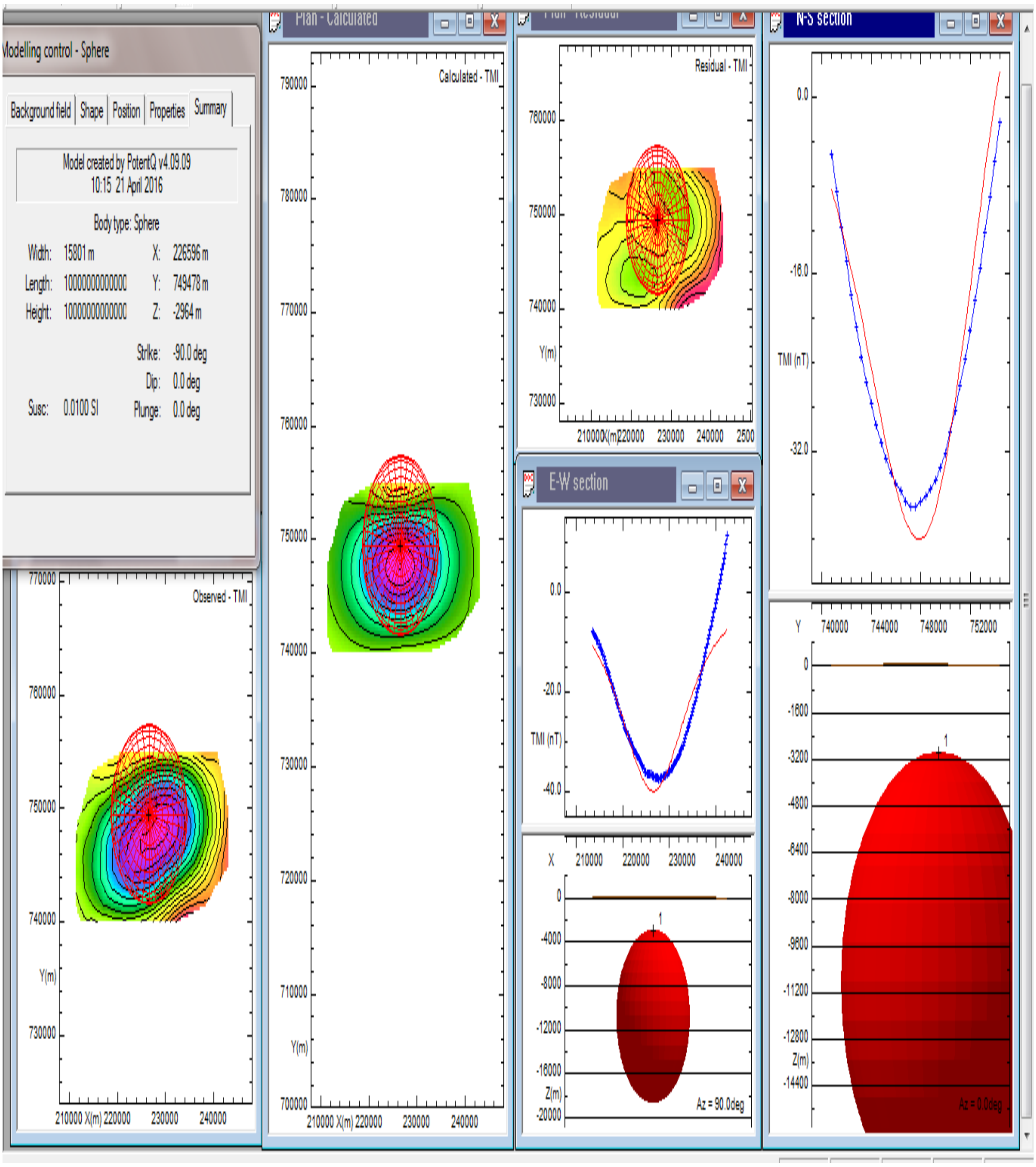

Figure 4.20*b*: forward and inverse modeling of profile $P2$

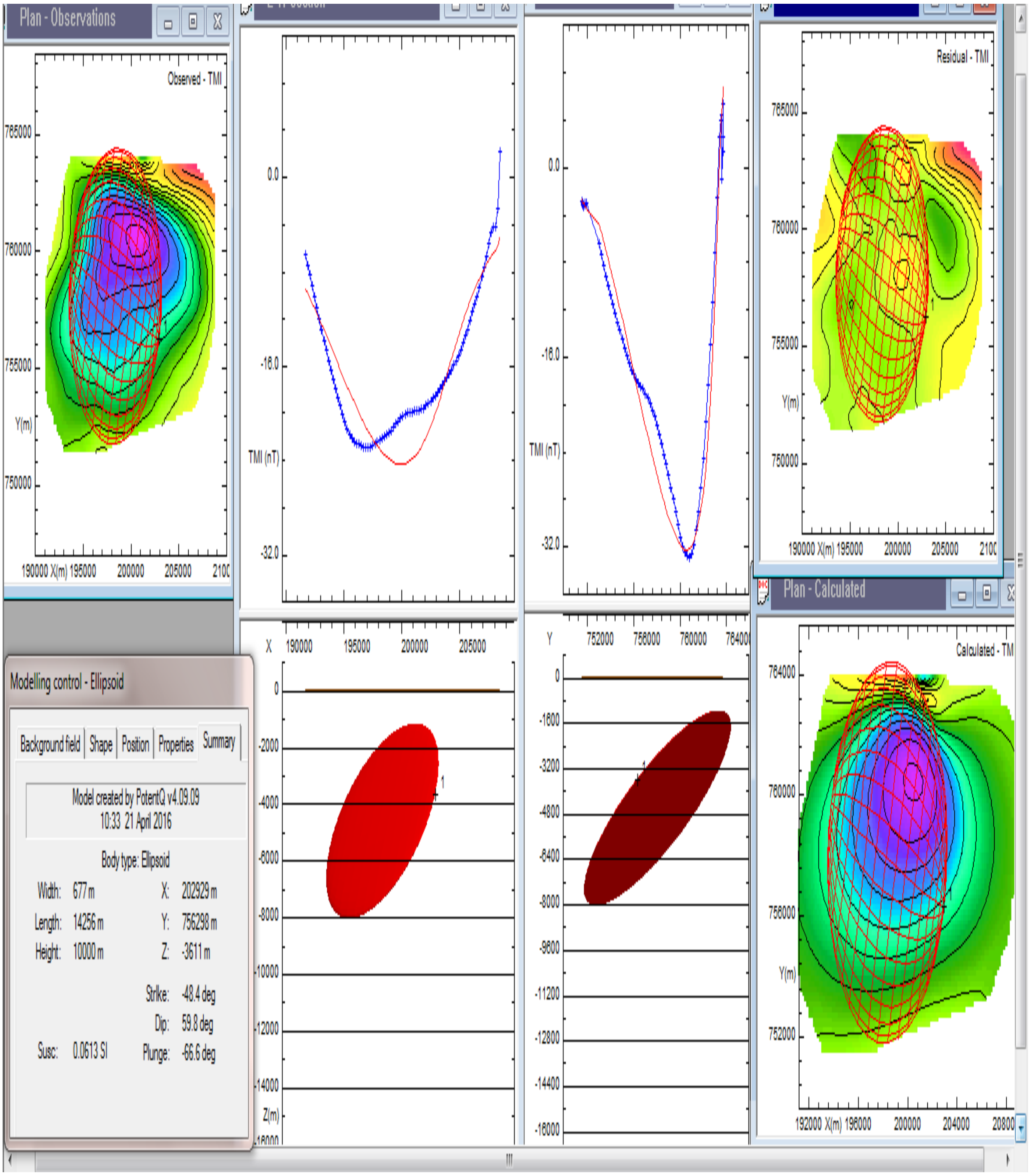

Figure 4.20*c*: forward and inverse modeling of profile $P3$

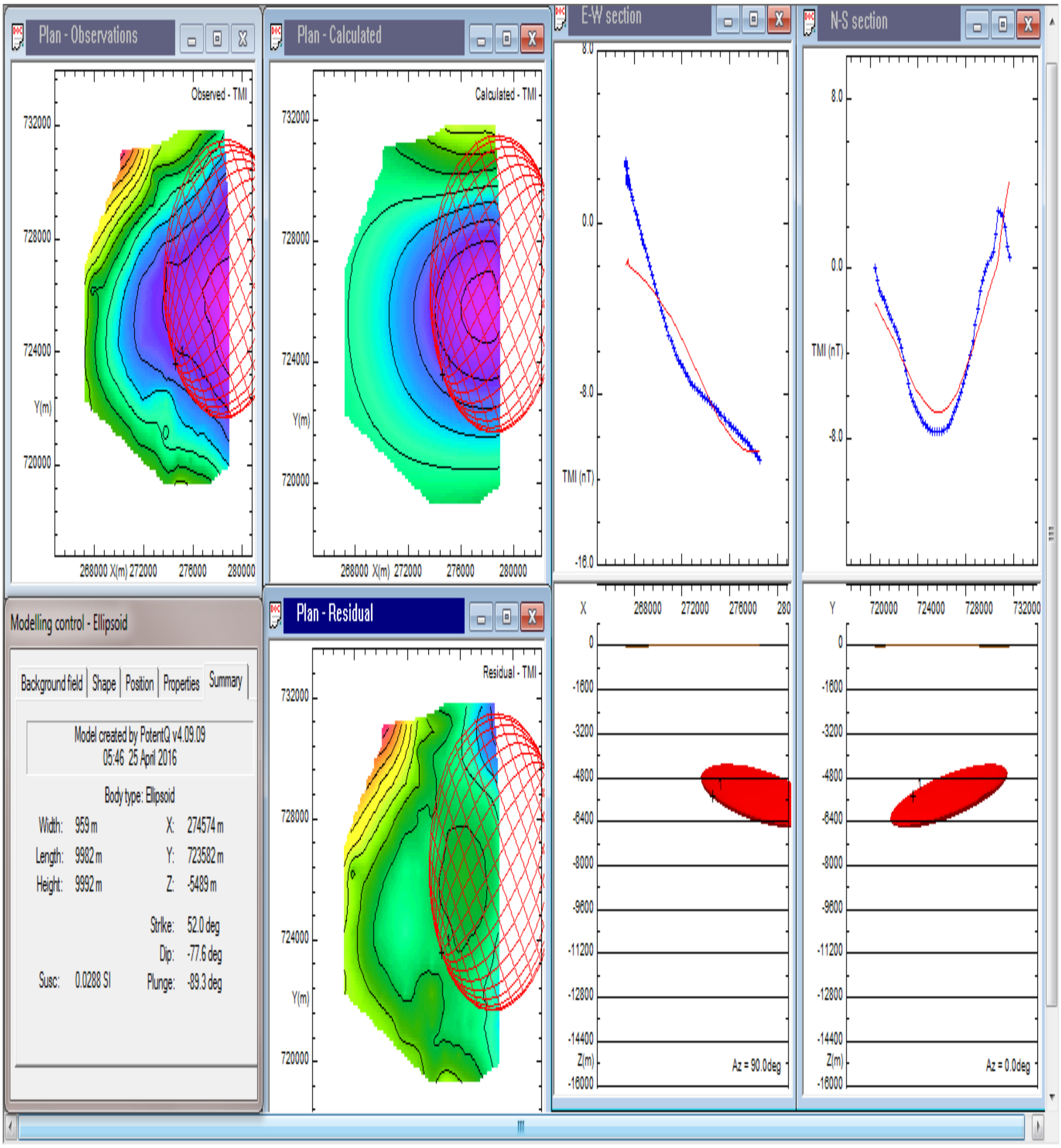

Figure 4.20*d*: forward and inverse modeling of profile *P*4

Table 4.2: Summary of forward and inverse modelling result

Profiles	X (m)	Y (m)	Depth (m)	Dip (deg.)	Plunge (deg.)	Strike (deg.)	Body shape	K value (SI)	Possible Mineral
1	230493	745118	-4118	84.00	-105.1	-63.2	Ellipsoid	0.0100	Hematite, Gneiss, Granite or Gabbro
2	226596	749478	-2964	0.0	0.0	-90.0	Sphere	0.0100	Hematite, Gneiss, Granite or Gabbro
3	202929	756298	-3611	58.8	-66.6	-48.4	Ellipsoid	0.0613	Porphyry (igneous rock)
4	274574	723582	-5489	-77.6	-89.3	52.0	Ellipsoid	0.0288	Slate or Hematite

4.4 Discussion of Results

The qualitative interpretation was carried out by visual inspection of the total magnetic intensity, reduction to pole, residual magnetic anomaly, regional magnetic anomaly, first vertical derivative, first horizontal derivative and Rose diagram maps.

The total magnetic intensity ranges from -48.7 nT to 100.7 nT (Figure 4.1). Higher values of magnetic intensity were found in the eastern and southern parts of the study area as indicated by the pink colour (Figure 4.1) and the lower values of magnetic intensity were found in the central and northern parts of the study area as indicated by the blue colour. The variation in magnetic intensity could be as a result of degree of strike, variation in depth, difference in magnetic susceptibility, difference in lithology, dip and plunge. Contour closures seen in the study area suggest the presence of magnetic bodies. The reduction to pole map (Figure 4.2) showed the Magnetic intensity of the map ranging from -400 nT to 450 nT. Higher magnetic values as indicated by letters A, B and C are found in the northern, central and southern areas respectively. The upward continuation showed magnetic intensity ranging from -40 nT to 95 nT (Figure 4.3). The map (Figure 4.3) showed low, intermediate and higher magnetic signatures. Higher magnetic signatures were found in the southern and eastern parts represented by K1 and K2 respectively.

The residual anomaly map from polynomial fitting of degree one (Figure 4.4) showed magnetic intensity ranging from -90 nT to 120 nT. The central and the northwestern portions of the map are characterized by low magnetic intensity values or weak anomalies. At the northwest part of the map are smaller magnetic contours which according to Gunn *et al.* (1997) is an indication of a distinct lithology from the surrounding or possibly a lava flow as evidenced by inhomogeneity of the magnetic units. Residual anomaly map from polynomial fitting of degree two (Figure 4.5) was done to see whether there may be some features which may be dominant after performing polynomial fitting of degree one. Figure 4.5 showed the magnetic intensity of the map ranging from -100 nT to 90 nT. The higher magnetic intensity values were found in the southern, eastern and northwestern parts of the map while the lower magnetic intensity values were found at the southeastern, central and northwestern parts of the map.

The regional anomaly map from polynomial fitting of degree one (Figure 4.6) showed the intensity of the map ranging from -45 nT to 80 nT. Figure 4.6 further showed the magnetic intensity of the area increasing from northwest to southeast direction. The regional anomaly map from polynomial fitting of degree two (Figure 4.7) showed the magnetic intensity of the map ranging from -35 nT to 105 nT. It further showed the magnetic intensity increasing conically from northwest to southeast. The first horizontal derivative map (Figure 4.8) showed that the map is characterized by low magnetic source bodies in general. Points G1 and G2 found in the northwest part showed higher magnetic intensity. The magnetic intensity of the map is very low in general, ranging from 0 nT to 0.054 nT. The first derivative map (Figure 4.9) showed magnetic intensity ranging from 18.925 nT to 19.02 nT. Higher magnetic intensity values were found in the southern, eastern and northwestern parts of the map. The lower magnetic values were found in the western, northern and central parts of the map. The Rose diagram (Figure 4.10) showed the structural lineament (fractures, faults, shear zones, veins and foliations) trends. From Figure 4.10, one can see the major anomaly trending in the northwest and southwest directions.

The quantitative interpretation was done by numerically determining the depth of shallow and deep magnetic bodies and modelling using; Source parameter imaging (SPI), Euler deconvolution, spectral analysis and modelling (forward and inverse) methods. The result of SPI depth ranges from 258.2 m to 3497.7 m (Figure 4.11). The Euler depth grids for various indices 0.5, 1, 2 and 3 shown in Figures 4.12 (a, b, c and d) showed the depth ranging from 1377.3 m (outcropping and shallow magnetic bodies) to 3089.9 m (deep magnetic source bodies). The study area (Ubiaja and Illushi) is characterized by rocky or mountainous formations. This can clearly be observed from the high positive values from the depth. The spectral depth obtained from spectral analysis revealed two major anomaly source depths, shallow and deep. The deep lying magnetic source bodies have sedimentary thickness ranging from 1114.085 m to 3978.874 m with an average depth of 2105.014 m whereas the shallow anomalous bodies have sedimentary thickness ranging from 163.836 m to 460.057 m with an average depth of 295.708 m as shown in Table 4.1. The thickest sedimentary cover occurred at spectral block P (Figure 4.13) located in the northern part of the map (Figure 4.15) which is indicated by the letter P. The point P according to Wright *et al.* (1985) is thick enough for the commencement of oil formation.

The depths deduced from the forward and inverse modelling are 4118 m, 2964 m, 3611 m and 5489 m for profiles 1, 2, 3 and 4 respectively (Figures 4.24a, 4.24b, 4.24c and 4.24d). The susceptibility values obtained from the model profiles 1, 2, 3 and 4 are 0.0100, 0.0100, 0.0613 and 0.0288 respectively. These susceptibility values according to Telford *et al.* (1990) (Table 3.1) indicates minerals like hematite, gneiss, granite, gabbro, porphyry or slate and they are all magnetic in nature.

From the four methods employed; SPI, Euler deconvolution, spectral analysis and modelling methods, the SPI and spectral analysis depths are of close range. Depths (thickness) obtained from modelling results (2964 m to 5489 m), SPI (258.2 m to 3497.7 m), Euler deconvolution (1377.3 m to 3089.9 m) and spectral analysis (1114.085 m to 3978.874 m) show thick sediment that is sufficient for hydrocarbon accumulation which agrees with the work of Wright *et al.* (1985) that the minimum thickness required for the commencement of oil formation for main organic remains would be 2300 m (2.3 km).

Onwe *et al.* (2015) carried out the estimation of sedimentary thickness in the eastern Anambra basin using the slope method and they found out that the sedimentary thickness ranges from 3.50 km to 7.00 km which is higher than the sedimentary thickness obtained from this work. Onuba *et al.* (2011) interpreted the aeromagnetic anomalies over Okigwe area and estimated the depth to basement using slope methods. They obtained two depth models, the deeper and shallow magnetic sources. Their deeper magnetic sources range from 2000 m (2.0 km) to 4990 m (4.99 km) while the shallow magnetic sources range from 400 m (0.4 km) to 1990 m (1.99 km). Their result is in close agreement with our depth result especially considering forward and inverse modelling method. Onwuemesi (1997) evaluated the depth to basement using spectral analysis in the Anambra basin and found the sedimentary thickness to vary from 900 m (0.9 km) to 5600 m (5.6 km). His result is in agreement with the result obtained from modelling method of this work. Obiora *et al.* (2015) interpreted aeromagnetic data of Nsukka area, Enugu state, Nigeria, for hydrocarbon exploration using SPI, inverse modelling and Euler deconvolution techniques. They obtained a depth range of 151.58 to 3082.7 m which is in close agreement with the SPI depth obtained in this work.

The results of some researchers (Onuba *et al*., 2011; Onwuemesi, 1997; Obiora *et al.,* 2015) who worked on the Anambra basin agree with the result of the present study especially with the shallow depth source. It must be noted that none of this work was carried out in Ubiaja and Illushi areas in the northern Anambra basin in particular, but in other parts of the Anambra basin.

CHAPTER FIVE

CONCLUSION AND RECOMMENDATION

5.1 Conclusion

Interpretations of aeromagnetic data of Ubiaja and Illushi areas have been carried out qualitatively and quantitatively. In the qualitative interpretation, the Rose diagram showed the structural (anomaly) trend in the study area. The major anomaly trends are in the northeast and southwest directions. Source parameter imaging (SPI), standard Euler deconvolution, spectral analysis and modelling (forward and inverse) methods were employed in the quantitative interpretation. The estimated depth from SPI ranges from 258.2 m to 3497.7 m. This agrees with the work of Wright *et al.* (1985) which asserts that the minimum thickness of sediment required for the commencement of oil formation from main organic remains would be 2300 m (2.3 km). The Euler 3D depth grid for structural indices (SI) 0.5, 1, 2 and 3 are shown in Figures $4.12a$, $4.12b$, $4.12c$ and $4.12d$ respectively. Depth range for SI = 0.5 is from $+1377.3$ m to -2510.9 m; for SI = 1, depths range from $+1482.0$ m to -3003.3 m; for SI = 2, depths range from $+1627.8$ m to -2984.3 m; and for SI = 3, depths range from $+1853.9$ m to -3089.9 m. From spectral analysis, two depth sources were determined, the deeper and the shallow magnetic sources. The deeper depth ranges from 1114.085 m to 3978.874 m with an average value of 2105.014 m while the shallow depth ranges from 163.836 m to 460.057 m with an average value of 295.708 m. The susceptibility values obtained from the model profiles 1, 2, 3 and 4 are 0.0100, 0.0100, 0.0613 and 0.0288 respectively, which indicate dominance of paramagnetic minerals (as indicated by positive susceptibility values) like hematite, gneiss, granite, gabbro, porphyry and slate.

The sedimentary thickness (depth to basement) from this work fairly agrees with the works of previous researchers (Onuba *et al.*, 2011; Igwesi and Umego, 2013; Obiora *et al.*, 2015) that have worked on the Anambra basin. Results from SPI, spectral analysis, forward and inverse modelling and standard Euler deconvolution methods show that the study area has sedimentary thickness that is fairly suitable for hydrocarbon accumulation. This study has greatly helped to delineate geophysical structures and has revealed the solid mineral potential of the study area.

5.2 Recommendation

These results and findings should further be confirmed by carrying out a land magnetic survey and also gravity survey of the study area.

REFERENCES

Adetona, A.A. and Abu, M. (2013). Investigating the Structures within the Lower Benue and Upper Anambra Basin, Nigeria, using First Vertical Derivative, Analytical Signal and Centre for Exploration Targeting (CET) plug-in. *Earth Science, 2*(5): 104 – 112.

Agagu, O.K., Fayose E.A. and Petter, S.W. (1985). Stratigraphy and sedimentation in the Senonian Anambra Basin of the Eastern Nigeria. *Journal of Mineral Geology, 22*: 25 – 36.

Agagu, O.K. and Adhijie, C.I. (1983). Tectonic and sedimentation framework of the Lower Benue Trough Southeastern Nigeria. *Journal of African Earth Sciences, 1:* 267 – 274.

Akanbi, E.S. and Fakoya, A.D. (2015). Regional Magnetic Field Trend and Depth to Magnetic Sourec Determination from Aeromagneti Data of Maijuju Area, North Central, Nigeria. *Physical Science International Journal, 8*(3): 1 – 13.

Ali, I., Olatunji, S., Nwankwo, L.I., Akoshile, C.O., Johnson, L.M. and Ellino, F. (2012). Geophysical Modeling of potential hydrocarbon traps in the lower Niger Delta, offshore West Africa. *Archives of applied science Research 4*(2): 863-874.

Amajor, L.C. (1989). Grain size characteristics and geologic controls on bed load sediments: A case study from the Imo River in South-eastern Nigeria. *Journal of African Earth Science. 9*: 507 – 515.

Ariffin, K.S. (2012). Geophysical Prospecting, earth science department University of Melbourne, Australia.

Baranov, V. and Naudy, H. (1964). Numerical calculation of the formula of reduction to the magnetic pole. *Geophysics, 29*: 67 – 79.

Benkhelil, J. (1989). The Evolution of the Cretaceous Benue Trough. *Journal of African Earth Sciences, 8:* 251 – 282.

Blakely, R.J. and Simpson, R.W. (1986). Approximating edges of source bodies from magnetic or gravity anomalies. *Geophysics, 51*: 1494 – 1498.

Burger, H.R., Sheehan, A.F. and Jones, C.H. (2006). *Introduction to applied Geophysics.* Published by Norton, W.W.

Dobrin, M.B. and Savit, C.H. (1988). *Introduction to Geophysical Prospecting (4th Edition).* McGraw Hill, New York.

Doell, R. and Cox, A. (1967). Magnetization of rocks. In: *Society of Exploration Geophysicists (SEG) theory of Exploration Geophysics, 2*: 446 – 453.

Emujakporue, G. and Ofoha, C.C. (2015). Spectral Depth Estimation of Subsurface Structures over Parts of Offshore Niger Delta, Nigeria. *The International Journal of Engineering and Sciences, 4*(10): 42 – 53.

Ezema, P.O., Eze, I.D., Ugwu, G.Z. and Abdulahi, U.A. (2014). Hydrocarbon and mineral Exploration in Abakaliki, Southern Nigeria. *International Journal of Engineering and Science, 3*(1): 24–30.

Fairhead, J.D., Williams, S.E. and Flanagan, G. (2004). Testing Magnetic Local Wavenumber Depth Estimation Methods using a complex 3D Test Model. *Society of Exploration Geophysicists Annual meeting, Denver, Extended Abstract.*

Gunn, P.J., Maidment, D. and Milligan, P.R. (1997). Interpreting Aeromagneic Data in Areas of limited outcrops. *Journal of Australian Geology and Geophysics, 17*(2): 175 – 185.

Horsfall, K.R. (1997). Airborne Magnetic and Gamma-ray Data Acquisition. *AGSO Journal of Geology and Geophysics*, *17*: 23 – 30.

Igwesi, I.D. and Umego, N.M. (2013). Interpretation of Aeromagnetic Anomalies over some Parts of Lower Benue Trough using Spectral Analysis Technique. *International Journal of Scientific and Technology Research*, *2*(8): 153 – 165.

Ikumbur, E.B., Onwuemesi, A.G., Anakwuba, E.K., Chinwuko, A.I., Usman A.O. and Okonkwo, C.C. (2013). Spectral Analysis of Aeromagnetic Data over Parts of the Southern Bida basin, West Central Nigeria. *International Journal of Fundamental Physical Sciences, 3*(2): 27 – 31.

Jacques, J.M., Parsons, M.E., Price, A.D. and Schwartz, D.M. (2003). Improving Geologic understanding with Gravity and Magnetic Data: *Examples from Gabon, Nigeria and Gulf of Mexico, First Break*, *21:* 57 – 62.

Kearey P., Brooks M. and Hill I. (2002). *An Introduction to Geophysical Exploration (3rd edition).* T.J international, Padstow, Cornwall. Hong Kong.

Kogbe, C.A. (1989). *The Cretaceous and Paleocene Sediments of the Southern Nigeria. In: Geology of Nigeria,* Kogbe C.A (Ed.). Elizabethan publication, Lagos, Nigeria, 273 – 286.

Langel, R.A. (1987). The main Field, *In: Jacobs J.A (Edition). Geophysics.* Academic Press, New York.

Mares, S. and Turdy, M. (1984). *Introduction to Applied Geophysic*s. Kluwer, Dordrecht.

Merill, R.T., McEthinny, M.W. and McFadden, P.L. (1996). *The Magnetic Field of the Earth: Paleomagnetism, the Core and the deep Mantle*. Academic Press, San Diego.

Musset, A.E. and Khan, M.A. (2000). *Looking into the Earth*. Cambridge University Press, New York, USA.

Nwajide, C.S. (2005). Anambra Basin of Nigeria: Synoptic Basin Analysis as a Basin for evaluating its Hydrocarbon Prospecting. In*: Hydrocarbon potentials of the Anambra Basin, Okogbue CO (Ed.).* Great AP press publishers Ltd; Nigeria, 1 – 46.

Nwajide, C.S. and Reijers, T.J.A. (1996). Geology of the Southern Anambra Basin In: *selected chapters of Geology, Reijers T.J.A. (Ed.).* SPDC, Warri, Nigeria, 133 – 147.

Nwankwo, L.I. (2006). A least square plane surface polynomial fit of two dimensional potential field geophysical data using Matlab. *Nigeria Journal of Pure and Applied Science, 21*: 2006 – 2013.

Nwosu, O.B. (2014). Determination of Magnetic Basement Depth over Parts of Middle Benue Trough by Source Parameter Imaging (SPI) Technique using HRAM. *International Journal of Scientific and Technology Research, 3*(1): 262 – 271.

Obaje, N.G. (2009). *Geology and Mineral Resources of Nigeria*. Springer Publishers, 1 – 203.

Obi, G.C. and Okogbue, C.O. (2004). Sedimentary response to the tectonism in the Campanian – Maastrichtian Succession, Anambra Basin, Southeastern Nigeria: *Journal of African Earth Sciences. 38:* 99 – 108.

Obiora, D.N., Ossai, M.N. and Okwoli, E. (2015). A Case study of Aeromagnetic Data Interpretation of Nsukka area, Enugu state, Nigeria, for Hydrocarbon Exploration. *International Journal of Physical Sciences, 10*(17): 503 – 519.

Ogala, J.E. (2011). Hydrocarbon Potentials of the Upper Cretaceous coal and shale units in the Anambra Basin, Southeastern Nigeria: *Petroleum and Coal, 53* (1): 35 – 44.

Okiwelu, A.A., Ofrey-Kulu, O. and Ude, I.A. (2013. Interpretation of Regional Magnetic Field Data Offshore Niger Delta. *Earth Science Research*, *2*(1): 13 – 18.

Onuba, L.N., Anudu, G.K., Chiaghanam, O.I. and Anakwuba, E.K. (2011). Evaluation of Aeromagnetic Anomalies over Okigwe Area, Southern Nigeria. *Research Journal of Environmental and Earth Sciences, 3*(5): 498 – 507.

Onwe, I.M., Odoh, B.I. and Onwe, R.M. (2015). Estimation of Sedimentary Thickness in Eastern Anambra Basin by Qualitative and Quantitative interpretation of Aeromagnetic Data. *Advances in Applied Science Research*, *6*(10): 1 – 6.

Onwuemesi, A.G. (1997). One Dimensional Spectral Analysis of Aeromagnetic Anomalies and Curie Depth Isotherm in Anambra Basin of Nigeria. *Journal of Geodynamics, 23*(2): 95 – 107.

Peterson, J.R. and Reeves, C.V. (1985). Application of Gravity and Magnetic Surveys: *The State-of-the Art in 1985, Geophysics, 50*: 2558 – 2594.

Reeves, C. (2005). *Aeromagnetic Surveys; Principles, Practice and Interpretation*. GEOSOFT.

Reid, A.B., Allsop, J.M., Granser, H., Millet, A.J. and Somerton, I.W. (1990). Magnetic interpretation in three dimensions using Euler deconvolution. *Journal of Geophysics, 55*: 80 – 91.

Reijers, T.J., Peters, S.W. and Nwajide, C.S. (1997). *The Niger Delta Basin*. In: Selley R.C (Ed.), African Basins. *Elsevier*, Amsterdan, 151 – 172.

Reyment, R.A. (1965). *Aspect of the Geology of Nigeria*. Ibadan University Press, Ibadan, Nigeria.

Simpson, A. (1954). The Nigerian coal field: The geology of parts of Onitsha, Owerri and Benue Provinces. *Geological Survey Nigerian Bulletin, 24*: 85.

Spector, A. and Grant, F.E. (1970). Statistical Models for Interpreting Aeromagnetic Data. *Journal of Geophysics, 35*(2): 293 – 302.

Telford, W,M., Geldart, L.P. and Sheriff, R.E. (1990). *Applied Geophysics* (2nd edition). Cambridge University Press, Cambridge.

Thurston, J.B. and Smith, R.S. (1997). Automatic conversion of magnetic data to depth, dip and susceptibility contrast using the SPI method. *Journal of Geophysics, 62*(3): 307 – 813.

Tijani, M.N., Nton, M.E. and Kitagawa, R. (2010). Textural and geochemical characteristic of the Ajali sandstone, Anambra basin South-east Nigeria: implication for its provenance. *Comptes Rendus Greoscene, 342*: 136 – 150.

Ugwu, G.Z. and Ezema, P.O. (2012). Forward and inverse Modelling of Aeromagnetic Anomalies over Abakaliki and Nkalagu areas of the Lower Benue Trough, Nigeria. *International Journal of Geology and Mining, 2*(8): 222 – 229.

Ugwu, G.Z., Ezema, P.O. and Ezeh, C.C. (2013). Interpretation of Aeromagnetic Data over Okigwe and Afikpo Areas of Lower Benue Trough, Nigeria. *International Research Journal of Geology and Mining, 3(*1): 1 – 8.

Valenta, J. (2015). *Introduction to Geophysics Lecture Notes*. Czech Republic Development Cooperation.

Wright, J.B., Hastings, D., Jones, W.B. and Williams, H.R. (1985). *Geology and Mineral Resources of West Africa*. George Allen and Urwin, London.